



Università degli Studi di Cagliari

**DOTTORATO DI RICERCA**

Scienze e Tecnologie Chimiche e Farmaceutiche

Ciclo XXIII

Structural and morphological characterization of  
hydrozincite and its interaction with organic molecules

Settore scientifico disciplinare di afferenza

CHIM/2-Chimica Fisica

Presentata da:  
Coordinatore Dottorato  
Relatore

Dott.ssa Roberta Sanna  
Prof. Mariano Casu  
Prof. Mariano Casu

Esame finale anno accademico 2009 - 2010



## Abstract

The morphological diversity and complexity of naturally occurring forms and patterns have been a motivation for humans to copy and adopt ideas from Nature to achieve functional, aesthetic and social value. Common biogenic materials, such as biominerals, constructed with mineral phases and an organic matrix exhibit delicate structure with unusual optimal chemical-physical, morphological and mechanical properties, and have inspired ideas for the design and synthesis of biomimetic functional materials. The organic templates play an important role in directing assembly of the mineral/organic composites, and in controlling the nucleation and subsequent crystallization. Consequently, knowledge about the molecular interactions at mineral/organic interfaces is essential for understanding the principles of the organic-matrix-mediated biomineralization process.

The microscopic properties of biomineral hydrozincite  $[\text{Zn}_5(\text{CO}_3)_2(\text{OH})_6]$  from Naracauli Creek (SW Sardinia) were investigated by using X-ray Diffraction (XRD), Fourier Transform Infrared (FT-IR), Nuclear Magnetic Resonance (NMR), Scanning Electron Microscopy (SEM), and High-Resolution Transmission Electron Microscopy (HR-TEM) and the organic matrix present has been extracted and characterized by using Fourier Transform Infrared (FT-IR).

In the context of molecular interactions at mineral/organic interfaces we describe an experimental study of the interaction of Bis(2-ethylhexyl)phthalate (DEHP) with hydrozincite. This interaction, under controlled laboratory experiments, was investigated by using Fourier Transform Infrared (FT-IR) and Nuclear Magnetic Resonance Spectroscopy (NMR).



## Acknowledgement

First, I would like to thank my supervisor Prof. Mariano Casu. He has given me the opportunity to explore the world of science and research in a really working environment. His enthusiasm for all the aspects of research was contagious, always helping me to do my best. His guidance, I could learn and explore several aspects of biomineralization and the interaction between minerals and organic molecules, applying different techniques for structural characterization.

I would really like to thank Prof. Anna Musinu for her help during my academic career. She has nicely and patiently answered to all of my questions, even the silliest ones. In particular, I would like to thank her for the valuable contribution to my first scientific publication.

I want also to thank Dr. Giovanni De Giudici, Dr. Francesca Podda, Dr. Elodia Musu, Dr. Riccardo Tombolini and Dr. Carla Cannas who contributed to my first paper making it possible.

In particular, I would like to thank Dr. Carla Cannas and Dr. Andrea Ardu for the XRD, TEM and HRTEM, Dr. Elodia Musu for the SEM and Dr. Marzia Fantauzzi for the XPS experiments, as well as Prof. Constantino Floris who helped me often with the organic chemistry involved in my job. Many thanks to Brian Phillips of the Stony Brook University for having hosted me in his group, where I could enlarge my knowledge and expertise on the Nuclear Magnetic Resonance, but also, giving me a valuable opportunity of personal growth.

During these three years I enjoyed discussing about science, as well as many other aspects of my life as Ph.D student, with Federica Orrù, Mauro Mureddu, Andrea Ardu, Alessandro Valente, Carla Cannas, Andrea Scorciapino, Cristina Piras, Marzia Fantauzzi and Davide Peddis, who largely contributed to my scientific and personal growth.

Also, I would like to thank the Bachelor and Master students I worked with: Michela Mulas, Alessio Cuccu, Valentina Mameli, Denise Carta, Roberto Piras, Giulia Casula and Silvia Meloni.

Last, but not least, I thank my parents Gina and Nicola, my brother Francesco, my sisters Rossana and Alessandra, my nephews Giuseppe, Elisa, Chiara, Giacomo, Giovanni and Simone, my brothers in law Giorgio and Giulio, my sister in law Simona whose constant support and encouragement has brought me so far.

I have no words to thank Barbara and Roberta, who have been my best friends all my life long. They have always helped whenever I was in trouble but, also, I hope they remember all the fun and laughs we have had.

Finally I would like to thank Salvatore for being my first supporter both when we were together and when I was abroad. I thank his parents for being so proud of me. I hope to live up to the expectations of all of you.

## Preface

This PhD was born from the collaboration with the Department of Earth Sciences Cagliari University. The research team superintended by Dr. Giovanni De Giudici from several years deal with the heavy metal abatement in the water of Naracauli creek (Sardinia, Italy) that follows the precipitation of biomineral hydrozincite. In this context the aim of my doctoral work was above all devoted to characterize the structural of biogenic hydrozincite deposition using spectroscopic, diffractometric and microscopic technique, such as X-ray Diffraction, Fourier Transform Infrared, Nuclear Magnetic Resonance, Scanning Electron Microscopy, and High-Resolution Transmission Electron Microscopy, and in a second time my interest was adressed to the chemical physical study of the interaction between synthetic hydrozincite and phthalates using Fourier Transform Infrared and Nuclear Magnetic Resonance.

This thesis reports the experimental work carried out at the Chemical Science Department, Cagliari University (Italy) under the supervision of Prof. Mariano Casu and a semester at the Geosciences Department of the Stony Brook University (New York, USA) under the supervision of Prof. Brian Phillips.

This description is divided into five sections:

- a) The first section presents a literature review about the interactions between minerals and organic molecules.
- b) The second section contains the experimental methods and the descriptions of the samples object of the study.
- c) The third section illustrates the general theory concerning the Solid State NMR.
- d) The fourth section is devoted to the results concerning the structural characterization of the biomineral hydrozincite.
- e) The fifth section examines the results concerning the interaction between synthetic hydrozincite mineral and Bis(2-ethylexyl)phthalate.





## Table of Contents

Abstract .....	ii
Acknowledgement .....	iv
Preface .....	vi
<b>Chapter I Introduction .....</b>	<b>1</b>
Generalities .....	1
1.1 Biomineralization and biominerals .....	2
1.1.1 Biologically induced mineralization .....	5
1.1.2 Biologically controlled mineralization .....	6
1.2 The nature of mineral surfaces .....	7
1.3 The organic mineral interface .....	10
1.4 The role of mineral in the pollution immobilization .....	12
1.5 Objectives .....	15
1.6 Overview on hydrozincite mineral .....	16
1.7 Phthalates and Bis(2-ethylexyl)phthalate.....	18
1.8 References.....	21
<b>Chapter II Materials and experimental procedures .....</b>	<b>35</b>
2.1 The samples object of the study .....	35
2.2 Extractions .....	40
2.3 Techniques - structural characterization .....	41

2.4 Analytical analysis .....	45
2.5 References.....	45
<b>Chapter III High Resolution Solid-State <sup>13</sup>C Nuclear Magnetic Resonance Spectroscopy .....</b>	<b>47</b>
3.1 Introduction .....	47
3.2 Magic Angle Spinning.....	48
3.3 High Power Proton Decoupling.....	49
3.4 Cross-Polarization .....	50
3.5 Relaxation phenomena .....	54
3.5.1 Transverse relaxation (T2) .....	54
3.5.2 Transverse relaxation (T1) .....	55
3.6 References.....	57
<b>Chapter IV Structural and morphological properties of hydrozincite minerals.....</b>	<b>59</b>
4.1 X-Ray diffraction measurement .....	59
4.2 Infrared Spectroscopy investigation.....	61
4.3 The morphologies analyzed by Scanning Electron Microscopy .....	65
4.4 HR-Transmission Electron Microscopy structural information .....	67
4.5 Solid State Nuclear Magnetic Resonance .....	70
4.5.1 <sup>13</sup> C MAS experiments .....	71
4.5.2 <sup>13</sup> C CPMAS experiments .....	73
4.5.3 Individual Gaussian decomposition of <sup>13</sup> C CPMA overlapped signals.....	75
4.5.4 Consideration on overlapped signals.....	78

4.5.5 Evidence of organic matrix in hydrozincite biomineral .....	82
4.6 FT-IR characterization of organic matrix.....	83
4.6.1 Characterization of insoluble extract.....	85
4.6.2 Characterization of lipidic extract.....	87
4.7 Conclusions.....	89
4.8 References.....	991
<b>Chapter V Characterization of the interaction hydrozincite/DEHP .....</b>	<b>99</b>
5.1 Hydrozincite in vitro synthesis .....	99
5.2 Identification of extract molecule .....	101
5.3 Origin of DEHP pollution.....	106
5.4 FT-IR study of hydrozincite synthesized in presence of PVC.....	107
5.5 FT-IR study of hydrozincite/DEHP mixture .....	109
5.6 <sup>13</sup> C MAS NMR investigation of hydrozincite/DEHP .....	112
5.7 <sup>13</sup> C CPMAS NMR investigation on hydrozincite /DEHP .....	116
5.8 <sup>13</sup> C CPMAS NMR experiments with different contact times .....	119
5.9 <sup>1</sup> H MAS informations .....	121
5.10 X-Ray complementary informations.....	1263
5.11 Conclusions.....	1265
5.12 References.....	126
<b>General Considerations .....</b>	<b>1269</b>
<b>Appendix .....</b>	<b>131</b>
<b>Scientific publications.....</b>	<b>135</b>



## Chapter I Introduction

---

### Generalities

Chemical interactions at crystal-water interfaces are crucial to a wide range of scientific and technological topics, including corrosion, heterogeneous catalysts, chemical sensors, teeth and bones, titanium implants and other prosthetic medical devices, and myriad commercial products including paints, glues, dyes, lubricants, solvents, and cleaners. Geochemists pay special attention to reactions between mineral surfaces and aqueous species interactions central to weathering, soil formation, hydrothermal ore-forming fluids, biomineralization, biofilm formation, uptake and release of chemicals that affect water quality, and many other natural processes (Davis and Kent, 1990; Stumm, 1992; Vaughan, 1995; Hochella, 1995; Drever, 1997; Langmuir, 1997; Brown et al., 1998; Brown and Parks, 2001; Davis et al., 2004; De Yoreo and Dove, 2004; Lee et al., 2006, 2007; Glamoclija et al., 2009). Studies of mineral-molecule interactions related to origins of life build on this vast geochemical literature. The study of the interaction of organic molecules on mineral surface is a very fascinating field that attracts the attention of researchers in different area: they go to the chemistry, the biology, the earth sciences and the material sciences. Mineral surface commonly include structural defects which provide promising docking loci for organic molecules, and this surface order-disorder provide some of the most fundamental constrains on reactions such a sorption, coprecipitation, crystal growth and dissolution.

At the same time, however, in nature are present organic pollutants and the mineral surfaces play an important role controlling the fate and transport of

contaminants in the environment. It is very fundamental to understand the molecular level interaction between surface mineral and organic pollutants for translate the information in the large scale for the design of chemical and biological remediation strategies.

## 1.1 Biomineralization and biominerals

Biomineralization refers to the process by which organisms form minerals. Over 60 different types of minerals with biological origins are known (Lowenstam and Weiner, 1989). Of the many essential elements required by living organisms,

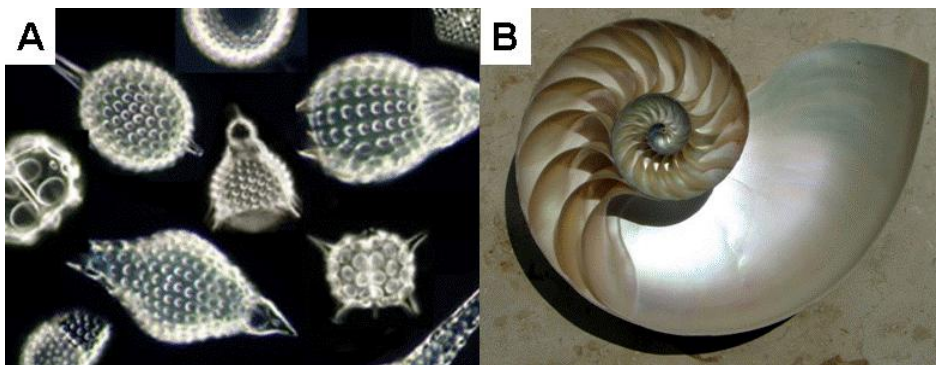


**Figure 1.1** Elegant examples of biomineralized products, in (A) *radiolarians* and (B) *nautilus* shell.

calcium is the most common of those found in biological minerals. Typical examples of these biominerals are certain layers of seashell, corals and eggshells. A variety of biomineral materials existing in nature present abundant morphologies and structure (Lowestam and Weiner, 1989). Examples include the widely varied scale produce by *radiolarians* (Fig. 1.1 A), and the impressive logarithmic symmetry of the *nautilus* shell (Fig. 1.1 B).

Organisms have evolved the ability to direct the formation of minerals into morphologies not naturally found in their inorganically derived counterparts. The resulting biominerals have unique morphologies, hierarchical structures and specific functions and often exhibit remarkable properties. The biomacromolecules exert a precise control on the deposition of the minerals and, thereby, create minerals with different shape and sizes. For example, human teeth show significant durability due to the well-aligned structure of hydroxiapatite crystals contains a small amount of protein (Furedimilhofer et al., 1994). With the study of biomineral systems, the biological concept, mechanism, function and design feature are abstracted as starting point on the road to new synthetic materials and devices with advanced structure and functions, this are called bio-inspired materials that have various application in different field as bioceramics, biosensing, biomedical engineering end bionanotechnology.

Numerous living organisms form minerals, biogenic minerals, or biominerals that are composite materials that contain an organic matrix and nano or macro scale amorphous or crystalline minerals. Biomineral composite materials include bone, dentine, enamel, statoliths, otoliths, mollusk and crustacean shells, coccolith scales, eggshells, sponge silica skeletons, algal, radiolarian and diatom silica micro-shells, and a variety of transition metal minerals produced by different bacteria (Lowenstam and Weiner, 1989; Weiner and Addadi, 1997; Banfield and Nealson, 1997; Fortin et al., 1997; Fitts et al., 1999; Lower et al., 2001; Mann, 2001; De Yoreo and Vekilov, 2003; Weiner and Dove, 2003; De Yoreo and Dove, 2004). Calcium is the most common essential element found in biological minerals. For example, familiar skeletal structures such as shell are built from calcium carbonate whereas the bones of higher organisms are composed of calcium phosphate. The biomineralization of calcium carbonate is found across many forms of life from the cell wall scales of coccolithophores to the inner ears of mammals

(Mann, 2001). These different structures are formed by a wide variety of organisms that initialize substantially different biological processes to result in various polymorphs of  $\text{CaCO}_3$  with distinctive mineralogies and composition (Morse and Mackenzie, 1990). Organisms have evolved the ability to direct the formation of minerals into morphologies not naturally present in their inorganic counterparts. As a result, the biominerals present specific functions and exhibit particular properties. From a materials science perspective, organic molecules are soft, compliant and fracture resistant while inorganic crystals are hard and brittle. Biomineral composites combine the best of these properties and minimize the weaknesses: they are both hard and fracture resistant (Currey, 1977; Schäffer et al., 1997; Kamat et al., 2000). This is due to several factors: structure, nano-size and chemical composition. Only recently materials scientists have begun to learn how to build a synthetic composite material that outperforms each component taken separately, and have done so inspired by shell nacre (Tang et al., 2003). These unique processes and particular properties of biomineralization are of interest for many scientific disciplines as chemistry, geology and materials science. The morphological control exerted in biomineralization may be separated into a three component system (Mann, 1983; Weiner, 1991):

- an insoluble organic matrix, which can play a role in compartmentalization of the growing mineral, and/or templating the nucleation for controlled crystallographic orientation and/or phase;
- soluble acid macromolecules (e.g. sulphate and/or phosphorylated glycoproteins contain large amounts of glutamic and aspartic acid) which are frequently occluded within the crystals (Weiner, 1991) and are thought to play a role in the control of crystal shape;
- vesicular compartments, which provide spatial and temporal control of ion and additive transport to the mineralization front.



There are two types of biomineralization depending on the level of biological control: “biologically induced” and “organic matrix-mediated” mineralization (Lowenstam, 1981), with the latter generalized in “biologically controlled” mineralization (Mann, 1983).

Biologically induced mineralization (BIM) occurs as result of chemical change in environment of an organism which can promote mineral precipitation as in the case of coral formation; in biologically controlled mineralization (BCM) morphologically complex structures nucleate and grow in concert with a genetically programmed macromolecules matrix of proteins.

### **1.1.1 Biologically induced mineralization**

Minerals that form by biologically induced mineralization (BIM) processes generally nucleate and grow extracellularly as a result of metabolic activity of the organism and subsequent chemical reactions involving metabolic byproducts. In many cases, the biological system has a little control on the mineralization (Weiner and Dove, 2003) and the organisms secrete one or more metabolic products that react with ions or compounds in the environment resulting in the subsequent deposition of mineral particles. The minerals that form are often characterized by poor crystallinity, broad particle-size distributions, and lack of specific crystal morphologies. In addition, the lack of control over mineral formation often results in poor mineral specificity and/or the inclusion of impurities in the mineral lattice. BIM is equivalent to inorganic mineralization under the same environmental conditions and the minerals are therefore likely to have crystallochemical features that are generally indistinguishable from minerals produced by inorganic chemical reactions. In some cases, the metabolic products diffuse away and minerals form from solution (Bazylinski and Frankel, 2003). However, bacterial surfaces such as

cell walls or polymeric materials (exopolymers) exuded by bacteria, including slimes, sheaths, or biofilms, and even dormant spores, can act as important sites for the adsorption of ions and mineral nucleation and growth (Beveridge, 1989; Konhauser, 1998; Banfield and Zhang, 2001; Bäuerlein, 2003).

### **1.1.2 Biologically controlled mineralization**

In biologically controlled mineralization, BCM, the organism exerts a great degree of crystallochemical control over the nucleation and growth of the mineral particles. For the most part, the minerals are directly synthesized at a specific location within or on the cell and only under certain conditions. The mineral particles produced by bacteria in BCM are characterized as well-ordered crystals with narrow size distributions, and specific, consistent particle morphologies. Because of these features, BCM processes are likely to be under specific chemical/biochemical and genetic control. In the microbial world, the most characterized example of BCM is magnetosome formation by the magnetotactic bacteria, a group of microorganisms in which BCM-produced magnetic crystals appear to have a relatively specific function. Biologically controlled mineralization can be described as occurring extra, inter or intracellular, and this distinctions refer to the location of the mineralization sites. However, not all the mineralization processes can be classified in this simple manner.

## 1.2 The nature of mineral surfaces

The theoretical crystalline surface terminates in an arrangement of atoms that approximates the planar truncation of a periodic three-dimensional crystal structure, but in real crystals this ideal situation is altered in several ways (e.g., Hochella and White, 1990; Somorjai, 1994; Hochella, 1995; Vaughan, 1995; Brown et al., 1998):

- surface atoms reside in an environment quite different from those below the surface, and thus undergo relaxation owing to boundary effects typically slight deviations from their formal crystallographic positions (Hochella, 1990; Stipp and Hochella, 1991; Wright et al., 2001);
- mineral surfaces in air or an aqueous medium are commonly subject to chemical alteration through oxidation, hydration, or hydroxylation (Guevremont et al., 1998; Biino et al., 1999; Stipp, 2002);
- crystals invariably have defects and impurities that alter local surface physical properties and chemical reactivity (Hochella, 1990; Cygan et al., 2002).

The topology of real crystal surfaces also represents an important deviation from ideality because crystal surfaces are seldom flat.

Mineral surfaces, with their low-level symmetries and multiple crystallographically distinct atomic sites, present additional complexities compared for example with the metals (Lasaga, 1990; Hazen, 2004). Although some common surfaces of rock-forming minerals can be ideally planar at the atomic scale (e.g., the [100] plane of quartz [SiO<sub>2</sub>], the [001] planes of graphite [C] and molybdenite [MoS<sub>2</sub>], and the [001] planes of varied layer silicates such as micas and chlorites), most surfaces are intrinsically irregular. Mineral surfaces also commonly include growth defects, step edges and kink sites, which provide promising docking loci for organic

molecules (Lasaga, 1990; Teng and Dove, 1997; Teng et al., 1998; Orme et al., 2001; Hazen and Sholl, 2003; De Yoreo and Dove, 2004). For example, Teng et al., 2006) showed the step-dependent adsorption of succinic acid (1,4-dicarbonylic acid) on irregular growth surfaces of calcite. The presence of succinic acid in solution blocks certain growth directions and thus dramatically modifies calcite surface growth morphology. Additional complexities arise from a variety of geological materials that do not have periodic two-dimensional surfaces, notably amorphous materials such as basaltic glass from seafloor volcanoes. Mesoporous zeolites and nano-particulate clays (including layer phyllosilicates and hydroxide minerals) interact with organic molecules in complex three-dimensional environments (Smith, 1998; Greenwell and Coveney, 2006; Benetoli et al., 2007). For example, Pitsch et al. (1995) showed that double-layer hydroxide minerals such as hydrotalcite efficiently adsorb glycoaldehyde phosphate and formaldehyde, presumably into their relatively spacious inter-layer regions, and promote condensation reactions to tetrose and hexose sugar phosphates. Given these complexities, any realistic modeling of interactions between biomolecules and mineral surfaces must take into account the geometries of both molecules and surfaces. Mineral surfaces undergo important modifications in an aqueous environment, especially in an electrolyte solution such as sea water (Parks, 1990; Davis and Kent, 1990; Van Cappellen et al., 1993; De Leeuw and Parker, 1997; De Leeuw et al., 1999; Wright et al., 2001; Stipp, 2002). In the classic electrical double layer (EDL) model, a crystal surface in pure water directly contacts a compact quasi-periodic layer of  $H^+$  or  $OH^-$  ions, whereas a second diffuse layer of mobile ions extends from the compact layer a few Ångstroms into the fluid. The nature of the EDL is strongly dependent on pH: At lower pH, the surface is typically protonated and thus positively charged, whereas at higher pH, the surface is negatively charged with hydroxyls. Adsorbed ionic and molecular species modify

the electrical double layer of mineral surfaces by displacing  $\text{OH}^-$ ,  $\text{H}^+$ , and  $\text{H}_2\text{O}$  at the solid-fluid interface. More than a century of experimental and theoretical research has explored the interaction of dissolved aqueous chemical species with mineral surfaces (Parsons, 1990; Hochella and White, 1990; Brown et al., 1998). Most of this important literature focuses on dissolved ions and inorganic complexes; however, many of the principles developed for mineral-ion interactions also apply to biomolecules. All surface-promoted reactions require at least one molecular species to interact with the surface. These interactions can be mediated by water molecules, protons, or hydroxyl groups through relatively weak interactions (outer-sphere adsorption, or “physisorption”). Alternatively, one or more chemical bonds can form (inner-sphere adsorption, or “chemisorption”). Chemisorbed ions typically bond to one or two surface atoms, whereas larger molecules can adopt a variety of surface topologies with multiple attachments (Davis and Kent, 1990; Zhang et al., 2004; Sverjensky et al., 2008; Jonsson et al., 2009). Details of molecular adsorption are dependent on several variables, most notably pH, the nature and concentrations of molecular solutes, and the identities and concentrations of electrolytes (Schindler, 1990; Sverjensky, 2005; Sverjensky and Fukushi, 2006; Jonsson et al., 2009). Additional complexities arise when organic molecules interact with crystal surface defects (Teng and Dove, 1997; Teng et al., 1998, 2000; Orme et al., 2001; De Yoreo and Dove, 2004; Elhadj et al., 2006). Such interactions can be strikingly revealed during crystal growth or dissolution in the presence of organic molecules, which can preferentially dock along crystallographically distinct edges and kinks. Such binding may inhibit crystal growth in certain directions and thus result in unusual crystal morphologies (e.g., Teng et al., 2006).

### 1.3 The organic mineral interface

Biom mineralization mechanisms are not completely clear (Mount et al., 2004), their understanding may provide models for new material, inspired design solutions and give new insight into the genetic control of biological structure (e.g. Schäffer et al., 1997). The mechanism of biom mineralization are poorly understood at the molecular level, in the bone, shell and some bacterial filaments, the organic matrix direct the formation of specific crystal phase, habit, size and orientation of the mineral. In the Figure 1.2 is shows a biom mineralization paradigm (Gilbert et al., 2005), but is not generalized and it is a simply intended to guide our reasoning and gives a visual model, however, it not included all biom mineralization systems. To this day, the organic molecular components have been identified in only few biom minerals. This paradigm, therefore, is to be interpreted as a conceptual mechanism, not a detailed model of interaction between known molecules. This paradigm can simplify the idea of the organic mineral interface and the chemical bonds at the interface. In BCM and BIM process (Lowenstam, 1981) the organic components are formed first, then these bind a few ions, which serve as nucleation sites for crystal growth (Lowenstam and Weiner, 1989; Falini et al., 1996). In Figure 1.2, the organic matrix (A) is composed from macromolecules which depending on the particular biom mineral may include a single organic molecule, e.g., a polysaccharide or a complex arrangement of proteins and glycoproteins. In all cases the organic components have charged functional groups that attract ions from solution (B). The steric arrangement of organic macromolecules, their sequence, and folding determines the precise position in three dimensions of the ions. Such positions are only compatible with a specific mineral, even more: they are only compatible with a well-determined polymorph of a specific mineral (C).

The crystal structure shown (C) is aragonite, the large white ions in (B) are  $\text{Ca}^{2+}$ , while the small-white and large-dark atoms are C and O, respectively in (C). In (D) is showed the zoom of the organic mineral interface, the inner-atomic bonds are indicated by dashed lines.

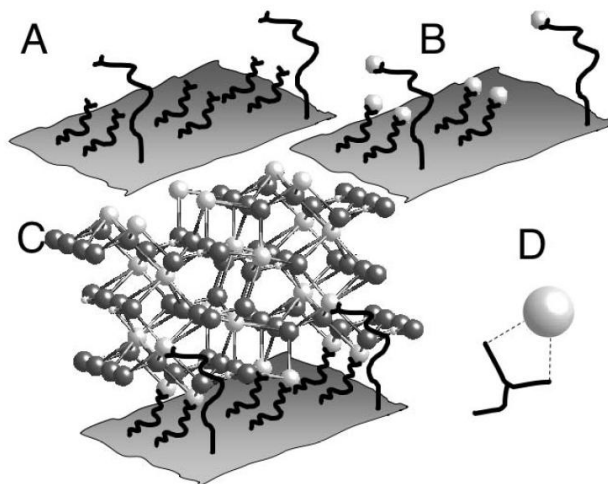


**Figure 1.2** The organic matrix (A) is composed of macromolecules, the organic components have charged functional groups that attract ions from solution (B). The steric arrangement of organic macromolecules, their sequence, and folding determines the precise position in three dimensions of the ions. Such positions are only compatible with a specific mineral, even more: they are only compatible with a well-determined polymorph of a specific mineral (C). The crystal structure shown (C) is aragonite, the large white ions in (B) are  $\text{Ca}^{2+}$ , while the small-white and large-dark atoms are C and O, respectively in (C). (D) Zooming in on the organic-mineral interface: the inter-atomic bonds are indicated by dashed lines.

Several authors suggest that the negatively charged amino acids, aspartate and glutamate, along their proteins sequences attract positive ions from solution and initiate crystal nucleation and growth (Mann, 2001; Weiner and Dove, 2003; Gotliv et al., 2005). The concentration of amino acid usually constitute between 30 and 40 mol% of the protein matrix. Gotliv et al. (Gotliv et al., 2005) show that the “Asprich”

family of proteins from the bivalve mollusk *Atrina rigida* contained more than 50 mol% of aspartate and 10 mol% of glutamate. For this reason, the paradigm by which negatively charged amino acid collect ions from solution provide the nucleation sites and direct growth biomineralization, is very interesting.

#### **1.4 The role of mineral in the pollution immobilization**

Minerals play an important role in the regulation of contaminants in ecosystems. In fact they can attenuate potentially toxic concentrations of contaminants and accordingly diminish the risk of surface water and groundwater contamination. For instance, silicates and oxides can adsorb organic pollutants, promoting their degradation to nontoxic forms, attenuating their movement through the environment, or preventing their uptake by plants and their introduction into the food chain. The characteristic of minerals as particle distribution, high specific area, structural order-disorder, and chemical groups in the surface make them highly reactive and permitted strong physical and chemical interaction with pollutant species, but at the other and also the physical chemical properties of the organic pollutant are dedicate by the structure of the molecule and the nature of the atom present in it, have an important role in the interactions.

For example, an important feature of clay minerals is the presence of structural negative charges, which enables clay minerals to adsorb different kind of molecules, especially organic and inorganic cations (Rytwo et al., 2002; Gürses et al., 2004; Lombardi et al., 2006), and at very low pH, the edges of 2:1 and 1:1 clay minerals carry a positive charge, which makes them capable to interact with anionic compounds. Fe, Al, Mn, Si and Ti oxides exhibit variable or pH-dependent surface charge, which is due to the amphoteric character of their surface hydroxyl groups. As a result, most oxides exhibit positive charge at low pH and negative



charge at high pH. Oxides with high point of zero charge, e.g. for goethite and hematite between pH 6-9, are therefore important adsorbents for anionic organic and inorganic substances (Cornell and Schwertmann, 2003). The quantification and understanding of immobilization mechanisms are of fundamental significance for predicting the fate of organic contaminants in a specific environment. In addition, knowledge about these mechanisms is essential for the development of efficient methods for contaminated soil and aquifer remediation. Sorption is generally the strongest interaction mechanism and can affect the fate of a contaminant in a number of ways. Apart from affecting mobility, and the potential for a contaminant to reach groundwater, sorption can affect the biodegradation and toxicity of a compound by influencing the bioavailability (Allard and Neilson, 1997; Guo, et al., 2000; Eggleton and Thomas, 2004; Arias-Estevez et al., 2008). There are generally many intermolecular interactions involved in sorption, but the dominant processes depend on chemical-specific properties, such molecular size and configuration, and polarity or lipophilicity, as well as mineral-specific properties, such as pH, surface groups and structural disorder.

For example, for polar contaminants, surface interactions include ionic and/or covalent and hydrogen bonding. Anionic contaminants are only weakly sorbed by minerals with permanent charge, such as clays, because they are electrostatically repulsed from negatively charged surfaces. Cationic contaminants are strongly sorbed on permanent negatively charged clay mineral surfaces by cation exchange. They interact much more strongly with the solid phase of soils and sediments than anionic ones, since ionisable organic-matter moieties and clay mineral surfaces are generally neutral or negatively charged over the pH range found in the environment.

However, for non-polar contaminants, the non-polar hydrophobic domains of organic matter provide important sorption sites and binding through hydrophobic

interactions (Van der Waals forces) will dominate the contaminant sorption (Wauchope et al., 2002; Semple et al. 2003). Sorption of hydrophobic organic contaminants to soil organic matter may be controlled by the amount of aromatic carbon (Abelmann et al., 2005), aliphatic carbon (Simpson et al., 2003, Chen et al., 2007), or the polarity of the soil organic matter (Tanaka et al., 2005). Müller et al. (2007) showed that also mineral surfaces could significantly contribute to the retention of hydrophobic organic contaminants, especially in subsurface soil horizons and aquifer sediments with small amounts of organic matter. The link between structure and physico-chemical properties of geosorbents and sorption activity of hydrophobic organic pollutants upon interaction with solid matrices has been established recently (Ehlers and Loibner, 2006). The conclusions are from high importance for studies on risk assessment and remediation. Currently research has focused on the development of low cost and highly reactive innovative materials. These modified natural or designed materials can be very useful in treating aqueous systems, including wastewater and aqueous waste streams, by removing undesired substances. In addition, it might be possible to incorporate or inject these materials into soil and subsoil, in order to enhance the sorption and retention of organic contaminants. From these studies it can be concluded that operative mechanisms for any particular interaction between contaminants, soil constituents and soil biota depends on the nature and properties of the soil surfaces, the chemistry of the system (e.g. pH, kind of exchangeable cations, water saturation degree) and the chemical nature of the organic contaminant.

## 1.5 Objectives

The main purpose of this study was to investigate and gain understanding of the fascinating world of biominerals and their interaction with organic molecules.

The first part of the thesis presents the structural and morphological characterization of biomineral hydrozincite and inorganic hydrozincite. This biomineral is a zinc carbonate  $[Zn_5(CO_3)_2(OH)_6]$  that has been found in a mine environment at Naracauli creek (Sardinia, Italy) in association with cyanobacteria (*Scytonema sp.*) and algae (*Chlorella*) (Podda et al., 2000). At Naracauli creek, as already shown in the literature, the precipitation of this biomineral results in the abatement of zinc concentration from hundreds ppm to few ppm in few hundred meters downstream. The presence of organic matter and the structural differences compared to inorganic mineral surface is presented and highlighted.

In the second part of the thesis the study has been devoted to the physico-chemical study of the interaction between synthetic hydrozincite and several phthalate. The problem of phthalate was born later when during investigation of the molecular-level basis of biomineralization, we found the presence of Bis(2-ethylhexyl)phthalate (DEHP) in some of the in-vitro synthesized samples. The DEHP was released by the tubing in PVC used for the synthetic preparation and captured by the mineral synthetic surface. The DEHP has an important role in the environmental context, due to the human health risk.

## 1.6 Overview on hydrozincite mineral

Hydrozincite [ $\text{Zn}_5(\text{CO}_3)_2(\text{OH})_6$ ] is a mineral formed in the oxidized zones of zinc deposits and is found as masses or crusts and is often not readily observed and may be confused with other minerals such as calcite. The mineral is often associated with other minerals such as smithsonite, calcite, hemimorphite, aurichalcite (Anthony et al., 2003).

The crystal structure of hydrozincite was first studied in a museum sample by Subrata Ghose in 1964 (Ghose, 1964) using single crystal X-ray diffraction. The structure is monoclinic with  $a_0=13.62$ ,  $b_0=6.30$ ,  $c_0=5.42$  Å,  $\beta = 95^\circ 50'$ , the space group is  $C2/m$ . There are two Zn sites, one in octahedral and one in tetrahedral coordination as shown in Figure 1.3. The octahedral sites outnumber the tetrahedral in the 3:2 ratio. Zinc atoms in tetrahedral coordination occur above holes that are present in sheets of octahedral zinc atoms.  $\text{CO}_3$  groups are binding the sheets parallel to (100). Out of the three oxygen atoms in the  $\text{CO}_3$  group the first is bonded to an octahedral, the second to the tetrahedral oxygen site while the remaining one is hydrogen bonded to three OH groups. The tetrahedral Zn-O distance is limited to 1.95 Å and is significantly smaller than the octahedral Zn-O distance at 2.10 Å. This author found also that synthetic crystals of hydrozincite have low crystallinity, and speculated that plane defects are the likely cause for the observed decrease in crystal order. After Ghose other authors studied the mineral hydrozincite, Infrared spectra from several hydrozincite specimens can differ significantly and show peak broadening (Jambor, 1966; Zabinsky, 1966). This difference was explained to the contributions of different plane defects. Conversely, Jambor (1964) and, more recently, Hales and Frost (2007) proposed that hydrous zinc carbonate could have two, or more, polymorphs.

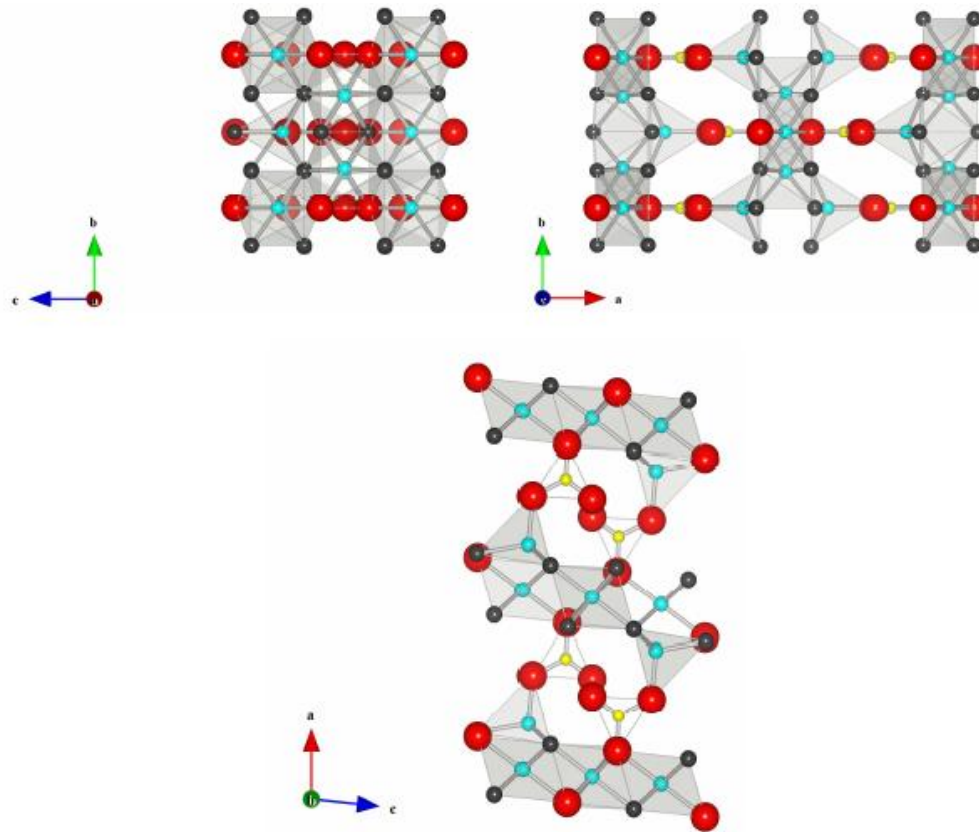


**Figure 1.3** The crystal structure of  $[\text{Zn}_5(\text{CO}_3)_2(\text{OH})_6]$ . The atoms of Zn are represented with cyan balls and they can be in octahedral and tetrahedral environment, as can be seen from the outline of the polyhedra shaded in gray. The atoms of O (red balls) are at the vertices of the polyhedra either stand-alone or bound with a hydrogen atom into an OH bond depicted as a black ball. The atom of C is shown as a yellow ball and finds itself in  $\text{CO}_3$  group bridging the  $\text{Zn}(\text{OH})_2$  that grow parallel to (100).

Beside structural issues, hydrozincite attracted the interest of many authors because of its role in the corrosion of Zn-rich materials (Stoffyn-Egli et al., 1998; Morales et al., 2006; Ghosh and Singh, 2007), for its involvement in controlling the

mobility of zinc in soils (Uygur and Rimmel, 2000) and waters (Mercy et al., 1998; Podda et al., 2000; Zuddas and Podda, 2005). Occurrence of hydrozincite forming in Zn-polluted calcareous soils was recently found by Jacquat et al. (2008). In addition, bioprecipitation of hydrozincite could represent an alternative biological approach for bioremediation of zinc-contaminated waters. A zinc carbonate, hydrozincite  $[Zn_5(CO_3)_2(OH)_6]$ , has been found in a mine environment at Naracauli creek (Sardinia, Italy) in association with cyanobacteria (*Scytonema sp.*) and algae (*Chlorella*) (Podda et al., 2000). At Naracauli creek, as already shown in the literature, the precipitation of this biomineral results in the abatement of zinc concentration from hundreds ppm to few ppm in few hundreds meters downstream. In addition, the bioprecipitation is also effective in the uptake of other heavy metals (Cd, Pb, etc) that are concentrated in the precipitate sediments.

## **1.7 Phthalates and Bis(2-ethylexyl)phthalate**

Phthalate esters are a large group of chemical compounds that are frequently used as plasticizers, solvents, and adhesives cosmetics, pesticides, building maintenance products, lubricants, and personal care goods that surround consumers at home, work, and in hospitals (Kato et al., 2004).

Phthalates are principal components of flexible polyvinyl chloride (PVC) products. PVC, after polyethylene is the second most widely used thermoplastic polymer, this material without additive is inherently a rigid and brittle material, requiring large amounts of plasticizer to make flexible products. In fact, approximately 90% of global plasticizer production is destined for use in PVC plastic (Bizzari et al., 2000; Houhhan and Wiles, 2000). The remaining 10% is used in other applications as adhesives, caulks, skin creams, detergents, electrical capacitors, hairspray, ink, solvents, lubrication oils, lotions, nail polish, paint, fragrances, and

pharmaceuticals (Shah and Shertukde, 2003). In personal care products, phthalate provide flexibility, create a film, and help dissolve and fix other cosmetics ingredients. The film forming and flexibility properties imparted by phthalates are also useful in paint, inks, fillers, adhesive and caulks and insulating properties in electrical cabling and capacitors (Gil et al., 2006).

The oily plasticizing properties of phthalates come from their chemical structure. Phthalate represent a broad chemical family containing a benzene ring, two carbonyl groups, and two alcohol groups to generate a diester structure. Common branched phthalates such as Bis(2-ethylhexyl)phthalate, Di-n-butyl phthalate, N-butyl-benzyl phthalate and Di-isononyl phthalate features branched chain alcohol moieties of 6 to 13 carbons. The linear phthalates containing linear alcohol groups and include short chain phthalates such as DEP and DMP, and other phthalate which chain lengths of 7 to 11 carbons are use to impart increased flexibility at low temperature.

The benzene ring based structure of phthalates helps reduce their viscosity but also makes them harder to degrade (Hatco Corp., 2002). Plasticizers act by breaking up the secondary bonds holding the polymer chains together and forming relatively weaker polymer-plasticizer bonds and thus impart mobility to the polymer chain and/or polymer chain segments. Plasticizing efficiency is generally considered to be a function of organic/inorganic moiety, functional groups present in the plasticizer molecule, the structure, a chain length, a molecular weight, etc. Thus, different plasticizers confer different plasticization effects because of the differences in the strength of plasticizer- polymer and plasticizer-plasticizer interactions. Phthalates move freely through the PVC polymer to impart flexibility and other characteristics (Tickner et al., 1999). Since they are not covalently bound to the polymer humans are exposed to contaminants in numerous ways, they are fairly easily released to air, water, saliva, blood, nutritional formula and other

extracting materials (National Chemicals Inspectorate, 1977; Petersen and Breindahl, 2000; Koch et al., 2003). This is especially true for Bis(2-ethylhexyl)phthalate (DEHP). DEHP is the most important phthalate and more than two million tons alone are produced worldwide each year (Lorz et al., 2002). DEHP, in fact, is extensively used to plasticize polyvinylchloride (PVC), which in turn is used to coat wires and flexible cables (Scholz et al., 2003). There is a large literature on the release of DEHP from plastic devices into the environment (Thuren, 1986; Calafant et al., 2004; Morrentsen et al., 2005).

DEHP migrates from the surface of the polymeric matrix during the use and distribution of products, or after their disposal (Petersen et al., 1997). DEHP has been a subject of public debate during recent years because it is suspected of being a human cancer-causing agent and could cause liver and kidney damage. Moreover it might damage the development of the reproductive organs and interfere with their development by acting as a mimic of the sex hormone, estrogen (Nielsen and Larsen, 1996). Environmental degradation of phthalates can occur by hydrolysis, photodegradation and biodegradation (Staples et al., 1997). These processes, however, are slow and therefore do not play an important role in degradation under typical environmental conditions (Asaoka et al., 2000). The most common methods for DEHP removal from water are aerobic (Khan and Jung, 2008) and anaerobic biological stabilisation, chemical stabilisation by lime, before or after dewatering and aerobic composting of the dewatered sludge (Marttinen et al., 2004).



## 1.8 References

- Abelmann, K., Kleineidam, S., Knicker, H., Gratwohl, P., Kogel-Knaber, I. Sorption of HOCs in soils with carbonaceous contamination: influence of organic matter composition. *J. Plant Nutr. Soil Sci.*, 168, 293 - 306 (2005).
- Allard, A.S. and Neilson, A.H. Bioremediation of Organic Waste Sites: A Critical Review of Microbiological Aspects. *Int. Biodeter. Biodeg.*, 39, 253-285 (1997).
- Anthony, J.W., Bideaux, R.A., Bladh, K.W., Nichols, M.C. *Handbook of Mineralogy*, Mineral Data Publishing, Tucson, Arizona, USA, (2003).
- Arias-Estevez, M., Lopez-Periago, E., Martinez-Carballo, E., Simal-Gandara, J., Mejuto, J.C., Garcia-Rio, L. Review: The mobility and degradation of pesticides in soils and the pollution of groundwater resources. *Agr. Ecosyst. Environ.*, 123, 247–260 (2008).
- Asaoka, K., Hagihara, K., Kabaya, H., Sakamoto, Y., Katayama, H., Yano, K. Uptake of phthalate esters, di(n-butyl)phthalate and di(2-ethylhexyl)phthalate, as environmental chemicals in monkeys in Japan. *Bull. Environ. Cont. Toxicol.*, 64, 679-685 (2000).
- Banfield, J.F. and Neilson, K.H. Geomicrobiology: interactions between microbes and minerals. *Rev. Mineral.*, 35 (1997).
- Banfield, J. F. and Zhang, H. Nanoparticles in the environment. *Rev. Mineral. Geochem.*, 44, 1 (2001).
- Bauerlein, E. Biomineralization of unicellular organisms: an unusual membrane biochemistry for the production of inorganic nano-and microstructures. *Angew. Chem. Int. Ed. Engl.*, 42, 614-641 (2003).
- Bazylinski, D.A., and Frankel, B.R. Biologically controlled mineralization in prokaryotes. *Rev. Mineral. Geochem.*, 54, 1, 217-247 (2003).

- Benetoli, L., de Souza, C., da Silva, K., de Souza, I. Jr, de Santana, H., Paesano, A. Jr, da Costa, A., Zaia, C., Zaia, D. Amino acid interaction with and adsorption on clays: FT-IR and Mossbauer spectroscopy and X-ray diffractometry investigations. *Orig. Life Evol. Biosph.*, 37, 479–493 (2007).
- Beveridge, T.J. The role of cellular design in bacterial metal accumulation and mineralization. *Annu. Rev. Microbiol.*, 43, 147-171 (1989).
- Biino, G., Mannella, N., Kay, A., Mun, B., Fadley, C. Surface chemical characterization and surface diffraction effects of real margarite (001): An angle-resolved XPS investigation. *Am. Mineral.*, 84, 629–638 (1999).
- Bizzari, S.N., Oppenberg, B., Ishtkawa, Y. Plasticizers. *Chemical Economics Handbook*. Palo Alto, CA, SRI International (2000).
- Brown, G.E. Jr., Heinrich, V.E., Casey, W.H., Clark, D.L., Eggleston, C., Felmy, A., Goodman, D.W., Grätzel, M., Maciel, G., McCarthy, M.I. Metal oxide surfaces and their interactions with aqueous solutions and microbial organisms. *Chem. Rev.*, 99, 77–174 (1998).
- Brown, G.E. Jr., Parks, G.A. Sorption of trace elements on mineral surfaces: Modern perspectives from spectroscopic studies, and comments on sorption in the marine environment. *Int. Geol. Rev.*, 43, 963–1073 (2001).
- Calafant, A.M., Slakman, A.R., Silva, M.J., Herbert A.R., Needham L.L. Automate solid phase and quantitative analysis of human milk for 13 phthalat metabolites. *J. Chromatogr. B., Anal. Technol. Biomed. Life Sci.*, 805, 49-56 (2004).
- Chen, G., Abichou, T., Tawfiq, K., Subramaniam, P.K. Impact of surface charge density on colloid deposition in unsaturated porous media. *Colloids Surf. A: Physicochem. Eng. Aspects*, 302, 342–348 (2007).
- Cornell, R.M. and Schwertmann, U. *The Iron Oxides*. 2nd ed. Wiley-VCH, Weinheim (2003).

- Cygan, R.T., Wright, K., Fidler, D.K., Gale, J.D., Slater, B. Atomistic models of carbonate minerals: Bulk and surface structures, defects, and diffusion. *Molec. Sim.*, 28, 475–495 (2002).
- Currey, J.D. Mechanical properties of mother of pearl in tension. *Proc. R. Soc. Lond. B*, 196, 443-463 (1977).
- Davis, J.A., and Kent, D.B. Surface complexation modeling in aqueous geochemistry. In Mineral-water interface geochemistry (ed. MF Hochella Jr, AF White), *Rev. Mineral.*, 23, 177–260 (1990).
- Davis, J.A., Meece, D.E., Kohler, M., Curtis, G.P. Approaches to surface complexation modeling of uranium (VI) adsorption on aquifer sediments. *Geochim. Cosmochim. Acta*, 68, 3621–3642 (2004).
- De Leeuw, N.H., Parker, S.C. Atomistic simulation of the effect of molecular adsorption of water on the surface structure and energies of calcite surfaces. *J. Chem. Soc., Faraday Trans 93*, 467–475 (1997).
- De Leeuw, N.H., Parker, S.C., Harding, J.H. Molecular dynamics simulation of crystal dissolution from calcite steps. *Phys. Rev. B*, 60, 13792–13799 (1999).
- De Yoreo, J.J. and Dove, P.M. Shaping crystals with biomolecules. *Science*, 306, 1301–1302 (2004).
- Drever, J.I. The geochemistry of natural waters. *Prentice Hall, New York*. (1997).
- Elhadj, S., Salter, E.A., Wierzbicki, A., De Yoreo, J.J., Han, N., Dove, P.M. Peptide controls growth on calcite mineralization: Polyaspartate chain length affects growth kinetics and acts as a stereochemical switch on morphology. *Cryst. Growth Des.*, 6, 197–201 (2006).
- Eggleton, J. and Thomas, K.V. A review of factors affecting the release and bioavailability of contaminants during sediment disturbance events. *Environ. International* 30, 973-980 (2004).

- Ehlers, G.A.C. and Loibner, A.P. Linking organic pollutant (bio)availability with geosorbent properties and biomimetic methodology: A review of geosorbent characterisation and (bio)availability prediction. *Environ. Poll.*, 141, 494-512 (2006).
- Falini, G., Albeck. S., Weiner, S., Addadi, L. Control of aragonite or calcite polymorphism by mollusk shell macromolecules. *Science*, 271, 67-69 (1996).
- Fitts, J.P., Persson, P., Brown, G.E. Jr, Parks, G.A. Structure and bonding of Cu(II)-glutamate complexes at the  $\gamma$ -Al<sub>2</sub>O<sub>3</sub>-water interface. *J. Colloid Surface Sci.*, 220, 133–147 (1999).
- Fortin, D., Ferris, F.G., Beveridge, T.J. Surface-mediated mineral development by bacteria. In *Geomicrobiology: Interactions Between Microbes and Minerals* (eds BanfieldJ, NealsonKH). 35, 161–180. *Mineralogical Society of America*, Washington, DC. (1997).
- Furedimilhofer H., Moradianoldak J., Weiner S., Veis A., Mintz K.P., Addadi L. *Connect. Tissue Res.*, 30-251 (1994).
- Ghose, S. The crystal structure of hydrozincite, Zn<sub>5</sub>(OH)<sub>6</sub>(CO<sub>3</sub>)<sub>2</sub>. *Acta Cryst.*, 17, 1051-1057 (1964).
- Ghosh, R. and Singh, D.D.N. Kinetics, mechanism and characterisation of passive film formed on hot dip galvanized coating exposed in simulated concrete pore solution. *Surf. and Coat. Techn.*, 201 (16-17), 7346-7359 (2007).
- Gil, N., Saka, M., Negulescu, I. (2006) Evaluation of the effects of biobased plasticizers on the thermal and mechanical properties of poly(vinyl chloride). *J. Appl. Polymer Sci.*, 102(2): 1366
- Gilbert, B. and Banfield, J.F. Molecular scale processes involving nanoparticulate minerals in biogeochemicalsystems. *Rev. Mineral. Geochem.*, 59,109-156 (2005).

- Glamoclija, M., Steele, A., Fries, M., Schieber, J., Voytek, M.A., Cockell, C.S. Association of anatase (TiO<sub>2</sub>) and microbes: unusual fossilization effect or a potential biosignature? *In* The ICDP-USGS Deep Drilling Project in the Chesapeake Bay Impact Structure: Results from the Eyreville Core Holes (ed. Gohn GS, et al. ) *Geol. Soc. Am. Spec. Pap.*, 458, 965–975 (2009).
- Gotliv, B.A., Kessler, N., Sumerel, J.L., Morse, D.E., Tuross, N., Addadi, L., Weiner, S. Asprich: a novel aspartic acid-rich protein family from the prismatic shell matrix of the bivalve *Atrina rigida*. *Chembiochem*, 6,304-314 (2005).
- Greenwell, H.C., and Coveney, P.V. Layered double hydroxide minerals as possible prebiotic information storage and transfer compounds. *Orig. Life Evol. Biosph.*, 36, 13–37 (2006).
- Guevremont, J.M., Strongin, D.R., Schoonin, M.A.A. Thermal chemistry of H<sub>2</sub>S and H<sub>2</sub>O on the (100) plane of pyrite: unique reactivity of defect sites. *Am. Mineral.*, 83, 1246–1255 (1998).
- Guo, L., Jury, W.A. Wagenet, R.J., Flury, M. Dependence of pesticide degradation on sorption:nonequilibrium model and application to soil reactors. *J. Cont. Hydrol.*, 43, 45–62 (2000).
- Gürses, A., Karaca, S., Dogar, Ç., Bayrak, R., Açikyildiz, M., Yalçın, M. Determination of adsorptive properties of clay/ water system: methylene blue sorption. *J. Colloid Interface Sci.*, 269, 310–314 (2004).
- Hales, M.C., and Frost, R.L. Synthesis and vibrational spectroscopic characterization of synthetic smithsonite and hydrozincite. *Polyhedron*, 26, 4955-4962 (2007).
- Hatco Corp. About esters, (2002).
- Hazen, R.M. Chiral crystal faces of common rock-forming minerals. *In Progress in Biological Chirality* (Eds. Palyi G et al.), Elsevier, New York 137–151 (2004).

- Hazen, R.M. and Sholl, D.S. Chiral selection on inorganic crystalline surfaces. *Nature Mater*, 2, 367–374 (2003).
- Hochella, M.F. Jr. Atomic structure, microtopography, composition, and reactivity of mineral surfaces. In *Mineral-water interface geochemistry*, (ed. MF Hochella Jr, AF White), *Rev. Miner.*, 23, 87–132 (1990).
- Hochella, M.F. Jr. Mineral surfaces: their characterization and their physical and reactive nature. *Mineral surfaces* (ed. DJ Vaughan, RAD Patrick), Chapman and Hall, New York 17–60 (1995).
- Hochella, M.F.Jr., and White, A.F. Editors. *Mineral-Water Interface Geochemistry*. *Rev. Mineral.*, 23, Mineralogical Society of America, Chantilly, VA. (1990).
- Houhhan, J., and Wiles, R. Beauty Secrets: Does a common chemical nail polish pose risks to human health? *Environ. Working Group*, (2000).
- Jacquat O., Voegelin A., Villard A., Marcus M.A., Kretzschmar R. Formation of Zn-rich phyllosilicate, Zn-layered double hydroxide and hydrozincite in contaminated calcareous soils. *Geochim. Cosmochim. Acta.*, 72, 5037-5054 (2008).
- Jambor, J. L. Studies of basic copper and zinc carbonates: I—Synthetic zinc carbonates and their relationship to hydrozincite. *Can. Mineral.*, 8, 92-108 (1964).
- Jambor, L.J. Natural and synthetic hydrozincites. *Can. Mineral.*, 8, 652-653 (1966).
- Jonsson, C.M., Jonsson, C.L., Sverjensky, D.A., Cleaves, H.J., Hazen, R.M. Attachment of L-glutamate to rutile ( $\alpha$ -TiO<sub>2</sub>): a potentiometric, adsorption and surface complexation study. *Langmuir*, 25, 12127–12135 (2009).
- Kamat, S., Su, X., Ballarini, R., Heuer, A.H. Structural basis for the fracture toughness of the shell of the conch *Strombus gigas*. *Nature*, 405, 1036–1040 (2000).

- Kato, K., Silva, M.J., Reidy, J.A., Hurtz, D. 3rd, Malek, N.A., Needham, L.L., Nakazawa, H., Barr, D.B., Calafat, A.M.. Mono(2-ethyl-5-hydroxyhexyl) phthalate and mono-(2-ethyl-5-oxohexyl) phthalate as biomarkers for human exposure assessment to di-(2-ethylhexyl) phthalate. *Environ. Health Perspec.*, 112(3), 327-30 (2004).
- Khan, M.H. and Jung, J.Y. Ozonation catalyzed by homogeneous and heterogeneous catalysts for degradation of DEHP in aqueous phase. *Chemosphere*, 72, 690–696 (2008).
- Koch, H., Drexler, H., Angerer, J. An estimation of the daily intake of di(2-ethylhexyl)phthalate (DEHP) and other phthalates in the general population. *Int. J. Hyg. Occup. Health*, 77–83 (2003).
- Konhauser, K.O. Diversity of bacterial iron mineralization. *Earth Sci. Rev.*, 43, 91–121 (1998).
- Lasaga, A.C., Holland, H.D., Dwyer, M.J. Primordial oil slick. *Science*, 174, 53–55 (1971).
- Langmuir, D. Aqueous environmental geochemistry Prentice-Hall, New York. (1997).
- Lee, H., Lee, B.P., Messersmith, P.B. A reversible wet/dry adhesive inspired by mussels and geckos. *Nature*, 448, 338–342 (2007).
- Lee, H., Scherer, N.F., Messersmith, P.B. Single-molecule mechanics of mussel adhesion. *Proc. Natl. Acad. Sci.*, 103, 12999–13003 (2006).
- Lombardi, B.M., Torres Sanchez, R.M., Eloy, P., Genet, M. Interaction of thiabendazole and benzimidazole with montmorillonite. *Appl. Clay Sci.* 33, 59–65 (2006).
- Lorz, P.M., Towae, F.K., Enke, W., Jäckh, R., Bhargava, N.. Phthalic acid and derivatives. In: Wiley-VCH (Ed.), *Ullmann's Encyclopedia of Industrial Chemistry. Release*, 7th Edition Online. Wiley-VCH, Weinheim (2002).

- Lowenstam, H.A. Minerals formed by organisms. *Science*, 211(4487), 1126-1131 (1981).
- Lowestam, H.A. and Weiner S. On biomineralization, Oxford University Press, New York (1989).
- Lower, S.K., Hochella, M.F., Beveridge, T.J. Bacterial recognition of mineral surfaces: Nanoscale interactions between *Shewanella* and alpha-FeOOH. *Science*, 292, 1360-1363 (2001).
- Mann, S., Archibald, D.D., Didymus, J.M., Douglas, T., Heywood, B.R., Meldrum, F.C., Reeves, N.J. Crystallization at Inorganic-organic Interfaces: Biominerals and Biomimetic Synthesis. *Science*, 261, 1286-1292 (1993).
- Mann, S. Biomineralization: Principles and Concepts in Bioinorganic Materials Chemistry. Vol 17. Oxford University Press, Oxford (2001).
- Martinen, S.K., Hänninen, K., Rintala, J.A. Removal of DEHP in composting and aeration of sewage sludge. *Chemosphere*, 54, 265–272 (2004).
- Morse, J.W. and Mackenzie, F.T. "Geochemistry of sedimentary carbonates". *Dev. Sedimentology*, 48, 1–707 (1990).
- Mercy, M.A., Rock, P. A., Casey, W. H., Mokarram, M. M. Gibbs energies of formation for hydrocerussite  $[\text{Pb}(\text{OH})_2 \cdot (\text{PbCO}_3)_2(\text{s})]$  and hydrozincite  $\{[\text{Zn}(\text{OH})_2]_3 \cdot (\text{ZnCO}_3)_2(\text{s})\}$  at 298 K and 1 bar from electrochemical cell measurements. *Am. Min.*, 83, 739-745 (1998).
- Morales, J., F., -Borges, J., . Atmospheric corrosion in subtropical areas: XRD and electrochemical study of zinc atmospheric corrosion products in the province of Santa Cruz de Tenerife (Canary Islands, Spain). *Corrosion Sci.*, 48 (2), 361-371 (2006).
- Morrentsen, G.K., Main, K.; Andersson, A.M., Leffers, H., Skakeback, N.E. Determination of phthalate monoester's in human milk and formula by tandem



- mass spectrometry(LC/MC/MS). *Annal. Bional. Chem.*, 382, 1084-1092 (2005).
- Mount, A.S., Wheeler, A.P., Paradkar, R.P., Snider, D. Hemocyte-mediated shell mineralization in the eastern oyster. *Science*, 304(5668), 297-300 (2004).
- Muller, S., Totsche, K.U., Kogel-Knabner, I. Sorption of polycyclic aromatic hydrocarbons to mineral surfaces. *Eur. J. Soil Sci.* 58, 918-931 (2007).
- Nass, L. Encyclopedia of PVC. New York: M. Decker (1977).
- Nielsen, E. and Larsen, X. Toxicological Evaluation and Limit Values for DEHP and Phthalates other than DEHP. *Danish Environ. Protect. Agency* (1996).
- Orme, C.A., Noy, A., Wierzbicki, A., McBride, M.T., Grantham, M., Teng, H.H., Dove, P.M., DeYoreo, J.J. Formation of chiral morphologies through selective binding of amino acids to calcite surface steps. *Nature*, 411, 775–778 (2001).
- Parks, G.A. Surface energy and adsorption at mineral-water interfaces: An introduction. In *Mineral-water interface geochemistry* (ed. MF Hochella Jr, AF White), *Rev. Mineral.*, 23, 133–175 (1990).
- Parsons, R. Electrical double layer: Recent experimental and theoretical developments. *Chem. Rev.*, 90, 813–826 (1990).
- Petersen, J.H. and Breindahl, T. Plasticizers in total diet samples, baby food and infant formulae. *Food Addit. Contam.*, 17, 133–141 (2000).
- Pitsch, S., Eschenmoser, A., Gedulin, B., Hui, S., Arrhenius, G. Mineral induced formation of sugar phosphates. *Orig. Life Evol. Biosph.*, 25, 297–334 (1995).
- Podda, F., Zuddas, P., Minacci, A., Pepi, M., Baldi, F., Heavy Metal Coprecipitation with Hydrozincite  $[Zn_5(CO_3)_2(OH)_6]$  from Mine Waters Caused by Photosynthetic Microorganisms. *Appl. Environ. Microbiol.*, 66, 5092–5098 (2000).

- Rytwo, G., Tropp, D., Serban, C. Adsorption of diquat, paraquat and methyl green on sepiolite: experimental results and model calculations, *Appl. Clay Sci.*, 20, 273–282 (2002).
- Schäffer, T.E., Ionescu-Zanetti, C., Proksch, R., Fritz, M., Walters, D.A., Almqvist, N., Zaremba, C.M., Belcher, A.M., Smith, B.L., Stucky, G.D., Morse, D.E., Hansma, P.K. Does abalone nacre form by heteroepitaxial nucleation or by growth through mineral bridges? *Chem. Mater.*, 9, 1731-1740 (1997).
- Schindler, P.W. Co-adsorption of metal ions and organic ligands: formation of ternary surface complexes. In *Mineral-Water Interface Geochemistry* (ed. MF Hochella Jr, AF White), *Rev. Mineral.*, 23, 281–307. (1990).
- Scholz, N. Ecotoxicity and biodegradation of phthalate monoesters. *Chemosphere*, 53, 921–926 (2003).
- Semple, K.T., Morriss, A.W.J., Paton, G.I. Bioavailability of hydrophobic organic contaminants in soils: fundamental concepts and techniques for analysis. *Eur. J. Soil Sci.*, 54, 809-818 (2003).
- Shah B. and Shertukde V.V., Effect of plasticizers on mechanical, electrical, permanence and thermal properties of poly(vinyl chloride). *J. Appl. Polym. Sci.*, 90, 3278 (2003).
- Simpson, M.J., Chefetz, B., Hatcher, P.G. Phenanthrene sorption to structurally modified humic acids. *J. Environ. Qual.*, 32, 1750 – 1758 (2003).
- Smith, J.V. Biochemical evolution. I. Polymerization on internal, organophilic silica surfaces of dealuminated zeolites and feldspars. *Proc. Natl. Acad. Sci.*, 95, 3370–3375 (1998).
- Somorjai, G.A. Introduction to surface chemistry, Wiley, New York (1994).
- Stipp, S.L. and Hochella, M.F.Jr. Structure and bonding environments at the calcite surface as observed with X-ray photoelectron spectroscopy (XPS) and low

- energy electron diffraction (LEED). *Geochim. Cosmochim. Acta*, 55, 1723–1736 (1991).
- Stipp, S.L. Where the bulk terminates: Experimental evidence for restructuring, chemibonded OH<sup>-</sup> and H<sup>+</sup>, adsorbed water and hydrocarbons on calcite surfaces. *Molec. Sim.*, 28, 497–516 (2002).
- Stoffyn-Egli, P., Buckley, D. E., Clyburne, J. A. C. Corrosion of brass in a marine environment: mineral products and their relationship to variable oxidation and reduction conditions. *Appl. Geochem.*, 13, 643-650 (1998).
- Stumm, W. Chemistry of the solid-water interface Wiley, New York. (1992).
- Sverjensky, D.A. Prediction of surface charge on oxides in salt solutions: revisions for 1:1 (M<sup>+</sup>L<sup>-</sup>) electrolytes. *Geochim. Cosmochim. Acta*, 69, 225–257 (2005).
- Sverjensky, D.M., Jonsson, C.M., Jonsson, C.L., Cleaves, H.J., Hazen, R.M. Glutamate surface speciation on amorphous titanium dioxide and hydrous ferric oxide. *Environ. Sci. Tech.*, 42, 6034–6039 (2008).
- Sverjensky, D.A., and Fukushi, K. Anion adsorption on oxide surfaces: Inclusion of the water dipole in modeling the electrostatics of ligand exchange. *Environ. Sci. Tech.*, 40, 263–271 (2006).
- Staples, C.A., Peterson, D.R., Parkerton, T.F., Adams, W.J. The environmental fate of phthalate esters: a literature review. *Chemosphere*, 35, 667–749 (1997).
- Tanaka, F., Fukushima, M., Kikuchi, A., Yabuta, H., Ichikawa, H., Tatsumi, K. Influence of chemical characteristics of humic substances on the partition coefficient of a chlorinated dioxin. *Chemosphere*, 58, 1319 – 1326 (2005).
- Tang, Z.Y., Kotov, N.A., Magonov, S., Ozturk B. Nanostructured artificial nacre, *Nature Materials*, 2 413-U8 (2003).
- Teng, H.H. and Dove, P.M. Surface site-specific interactions of aspartate with calcite during dissolution: Implications for biomineralization. *Am. Mineral.*, 82, 878–887 (1997).

- Teng, H.H., Dove, P.M., Orme, C., DeYoreo, J.J. The thermodynamics of calcite growth: a baseline for understanding biomineral formation. *Science*, 282, 724–727 (1998).
- Teng, H.H., Dove, P.M., DeYoreo, J.J. Kinetics of calcite growth: analysis of surface processes and relationships to macroscopic rate laws. *Geochim. Cosmochim. Acta*, 64, 2255–2266 (2000).
- Teng, H.H., Chen, Y., Pauli, E. Direction specific interactions of 1,4-dicarboxylic acid with calcite surfaces. *J. Am. Chem. Soc.*, 128, 14482–14484 (2006).
- Thuren, A. Determination of phthalic aquatic environments. *Bull. Environ. Contamin. Toxicol.*, 36, 33-40 (1986).
- Tickner, J., Hunt, P., Rossi, M., Haiama, N., Lappe M. The Use of Di-2-Ethylhexyl Phthalate in PVC Medical Devices: Exposure, Toxicity, and Alternatives. Lowell: Lowell Center for Sustainable Production, University of Massachusetts Lowell (1999).
- Uygur, V. and Rimmer, D.L. Reactions of zinc with iron-oxide coated calcite surfaces at alkaline pH. *Europ. J. of Soil Sci.*, 51 (3), 511-516 (2000).
- Van Cappellen, P., Charlet, L., Stumm, W., Wersin, P. A surface complexation model of the carbonate mineral-aqueous solution interface. *Geochim. Cosmochim. Acta*, 57, 3505–3518 (1993).
- Vaughan, D.J. Mineral surfaces: an overview. In *Mineral Surfaces*, (ed. DJ Vaughan, RAD Patrick), Chapman and Hall, New York 1–16 (1995).
- Wauchope, R.D., Yeh, S., Linders, B.H.J., Kolskowski, R., Tanaka, K., Rubin, B., Katayama, A., Kördel, W., Gerstel, Z., Lane, M., Unsworth, J.B. Pesticide soil sorption parameters: theory, measurement, uses, limitations and reliability. *Pest Management Science*, 58, 419-445 (2002).
- Weiner, S., and Addadi, L. Design strategies in mineralized biological materials. *J. Mater. Chem.*, 7, 689–702 (1997).

- Weiner, S. and Dove, P. An overview of biomineralization processes and the problem of the vital effect. *Rev. Miner.*, eds Weiner and Dove, MSA, 54, 1-24. (2003)
- Wright, K., Cygan, R.T., Slater, B. Structure of the (10-14) surfaces of calcite, dolomite, and magnesite under wet and dry conditions. *Phys. Chem. Chem. Phys.*, 3, 839–844 (2001).
- Yoreo, J.J. and Vekilov, P.G. Principles of nucleation and growth. *Rev. Miner.*, eds Weiner and Dove, MSA. 54, 57-90 (2003)
- Zabinsky, W. The problem of stacking-order in natural hydrozincite. *Can. Mineral.*, 8, 649-652 (1966).
- Zhang, Z., Fenter, P., Cheng, L., Sturchio, N.C., Bedzyk, M.J., Machesky, M.L., Wesolowski, D.J. Model-independent X-ray imaging of adsorbed cations at the crystal-water interface. *Surf. Sci.*, 554, 95–100 (2004).
- Zuddas, P. and Podda, F. Variations in physico-chemical properties of water associated with bio-precipitation of hydrozincite  $[\text{Zn}_5(\text{CO}_3)_2(\text{OH})_6]$  in the waters of Rio Naracauli, Sardinia (Italy). *Appl. Geochem.*, 20, 507-517. (2005).



## Chapter II Materials and experimental procedures

---

### 2.1 The samples object of the study

- **Natural hydrozincite**

The sample labeled with the name Nar is a natural sample from Rio Naracauli. The Rio Naracauli flows in a 30.2 km<sup>2</sup> basin west of the Ingurtosu mine in the Arburese mine district in southwestern Sardinia (Fig. 2.1). The river is about 8.2 km long and flows into the western Mediterranean Sea. The Rio Naracauli has a very limited flow, particularly in the upper part. Upstream it receives drainage from mine tailings on the left, and downstream it receives drainage from three adits: the Rio Pitzinurri (outlet A), the Ledoux mine gallery (outlet B), and the Rio Bau (outlet C). The hydrogeological details of this area have been reported by Pala et al. (1996). A series of stations (stations 1 to 11 in the creek and stations A to C in the three tributaries) were chosen along 3.4 km of the Rio Naracauli (Fig. 2.1). Station 1 was located at the tailings pond. In stations 2 to 4, a photosynthetic microbial population visibly encrusted the sediments with a green mat in spring, which developed into white material, particularly at stations 3 and 4. This is an annual event that varies in intensity depending on the meteorological conditions. The white precipitate is then mechanically transported away by rainfalls. Stations 5 to 7 were located after the Rio Pitzinurri tributary. In the sediments of these stations white precipitate residues were still visible. Stations 8 to 10 were located after the Ledoux gallery. Station 11 was located downstream from the Rio Bau tributary, where white deposits were not observed. The Nar sample was collected between the station 2 and 4 dried at room temperature and cleaned by the visible impurities.

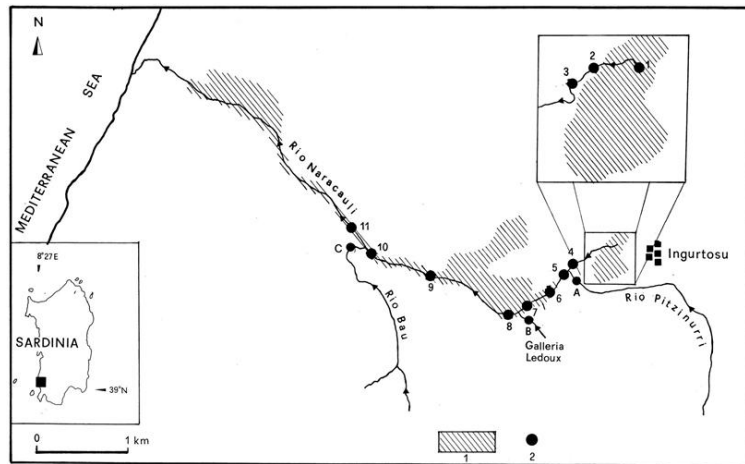


**Figure 2.1** Schematic map of the sampling area, with tailings distribution (hatched areas). Samples 1 to 11 (●) are from the Rio Naracauli stream; samples A to C were collected in the tributaries before the inflows.

- **Geological hydrozincites**

We have investigated two geological samples of hydrozincite kindly provided to us by the Mineral Museum of the Earth Science Department of the University of Cagliari. Both samples come from mining districts of Sardinia, Geol1 from Malfidano mine and Geol2 from Sa Duchessa mine.

The mining district of southwest Sardinia, Italy, is one of the classic areas where primary carbonate-hosted Zn-Pb sulfide ores are associated with a relatively thick secondary oxidation zone containing Zn (hydroxy-)carbonates and silicates, the so-called "calamine," exploited until the 1970s. The extent of the capping oxidized ore zones, reaching deep below the surface, is generally independent of the present-day water table. The base of the oxidation profile containing nonsulfide Zn minerals in various uplifted blocks in the Iglesiente area can be either elevated above or



submerged below the recent water table. The genesis of the ores is therefore considered to be related to fossil, locally reactivated, oxidation phenomena. The mineralogy of the nonsulfide mineralization is generally complex and consists of smithsonite, hydrozincite, and hemimorphite as the main economic minerals, accompanied by iron and manganese oxy-hydroxides and residual clays. These geological samples are more than million years old (Boni et al., 2003).

- **Hydrozincite synthesis**

**Hy1** – the sample was synthesized according to the protocol of Garcia-Clavel (1989) for the preparation of binary carbonate. The sample has been made by fast precipitation at 373 K mixing equal amounts of a 32 mM  $(\text{NH}_4)_2\text{CO}_3$  (Aldrich) solution and a 80 mM  $\text{Zn}(\text{NO}_3)_2 \cdot 6\text{H}_2\text{O}$  (Aldrich) solution. The precipitate obtained was filtered, washed with cold distilled water and dried at room temperature.

**Hy2** – the sample was synthesized according to the protocol of Paquette and Reeder (1995) at 298 K. One liter of a 50 mM  $\text{Zn}(\text{NO}_3)_2 \cdot 6\text{H}_2\text{O}$  (Carlo Erba Reagents) and 280 mM  $\text{NH}_4\text{Cl}$  (Carlo Erba Reagent) solution was placed into a closed reactor. The reactor was in communication with a vial containing  $(\text{NH}_4)_2\text{CO}_3$  (Aldrich) as a fine powder. The slow decomposition of this salt releases  $\text{NH}_3$  and  $\text{CO}_2$  to the solution. During the next 15 days hydrozincite began to precipitate at the water–vapour interface. The solution pH, initially was slightly acid (4.9-5.2) and the final pH was 7. The precipitate obtained was filtered, washed with deionized water and dried at room temperature.

**Hy3** – the sample has been made at 298 K by mixing of 0.2 mM of  $\text{NaHCO}_3$  (Carlo Erba Reagent 99,9%), 3 mM of  $\text{Na}_2\text{CO}_3$  (Aldrich) and 3 mM of  $\text{ZnSO}_4 \cdot 7\text{H}_2\text{O}$

(Aldrich) into deionized water, subsequently acidified by using HCl to adjust the initial pH at 6.7. The concentration of zinc was determined considering the concentration of  $Zn^{2+}$  in the natural water of Naracauli Creek during the hydrozincite bioprecipitation (Podda et al., 2000). The solution stirred throughout the synthesis in a glass baker was continually bubbled with air through glass tubing connect with an aquarium pump. After 15 days the solution was filtered and the precipitate rinsed several times with deionized water and then dried at room temperature.

**Hy4** – the sample has been make at 298 K by mixing of 0.2 mM of  $NaHCO_3$  (Carlo Erba Reagent 99,9%), 3 mM of  $Na_2CO_3$  (Aldrich) and 3 mM of  $ZnSO_4 \cdot 7H_2O$  (Aldrich) into deionized water, subsequently acidified by using HCl to adjust the initial pH at 6.7. The concentration of zinc was determined considering the concentration of  $Zn^{2+}$  in the natural water of Naracauli Creek during the hydrozincite bioprecipitation (Podda et al., 2000). The solution stirred throughout the synthesis in a glass baker was continually bubbled with air through plastic tubing connect with an aquarium pump. After 15 days the solution was filtered and the precipitate rinsed several times with deionized water and then dried at room temperature. A portion of sample has been subsequently washed with 1 ml of acetone (Aldrich) which was then separate from the solid; this washing procedure was repeated three times. The name of washed sample is Hy4/1.

**Hy5** – the sample has been making as described for the sample Hy3 but adding slices of flexible tube in PVC (Tygon) at the bottom of reaction glass baker. A portion of sample has been subsequently washed with 1 ml of acetone (Aldrich) which was then separate from the solid; this washing procedure was repeated three times. The name of washed sample is Hy5/1.

**Hy3-MIXDEHP** – 300mg of hydrozincite Hy3 has been mixed with various quantities of pure Bis(2-ethylexyl)phthalate (Aldrich, 99%) as reported in the Table 2.1. A portion of each mixing samples has been subsequently washed with 1 ml of acetone (Aldrich) which was then separate from the solid; this washing procedure was repeated three times for each mixing samples.

Sample	HY3 (mg)	DEHP ( $\mu$ l)	Sample washed
Hy3-25DEHP	300	25	Hy3-25DEHP/1
Hy3-50DEHP	300	50	Hy3-50DEHP/1
Hy3-100DEHP	300	100	Hy3-100DEHP/1
Hy3-200DEHP	300	200	Hy3-200DEHP/1
Hy3-400DEHP	300	400	Hy3-400DEHP/1

**Table 2.1** Summary of conditions for preparation of mixed samples.

- **Calcite synthesis**

**Cal1** – the sample was synthesized according to the protocol of Paquette and Reeder (1995) at 298 K. In this method the solid ammonium carbonate sublimates, and product  $\text{NH}_3$  and  $\text{CO}_2$  gases diffuse into an aqueous solution of calcium and ammonium chloride. 200 mM of  $\text{CaCl}_2 \cdot 6\text{H}_2\text{O}$  (Aldrich) was adding to 300 mM of  $\text{NH}_4\text{Cl}$  (Aldrich) in 1 l of deionized water. The glass baker contain the aqueous solution was placed inside a closed container in the presence of ammonium carbonate, so that creates a rich atmosphere of  $\text{NH}_3$  and  $\text{CO}_2$  that diffuses into the aqueous solution. The solution pH, initially slightly acid (4.9-5.2), during the next 15 days, the calcite crystals nucleated at the surface of the solution. The final pH was

7. The precipitate obtained was filtered, washed with deionized water and dried at room temperature.

**Cal2** – the sample has been making following the protocol for Cal1, but in this case the sliced out flexible pipes were added at the bottom of the reaction system.

**Cal1-100DEHP** – 300mg of calcite Cal1 has been mixed with 100µl pure Bis(2-ethylexyl)phthalate (Aldrich, 99%). A portion of each mixing sample has been subsequently washed with 1 ml of acetone (Aldrich) which was then separate from the solid; this washing procedure was repeated three times for each mixing samples. The name of washed sample is Cal1-100DEHP/1.

## **2.2 Extractions**

- **Extraction of Bis(2-ethylexyl)phthalate in synthetic hydrozincite**

Powder synthetic hydrozincite was soaked in chloroform at 40°C for 12 h, after this time, the mixture was filtered. The mixture contains extract and chloroform was evaporated in a rotary evaporator.

- **Extraction insoluble organic matrix in biomineral sample**

The powder sample was immersed in 5 ml of distilled water, then decalcified by progressive addition of 50% acetic acid to maintain the pH above 4. The entire extract was centrifuge ad 4500 xg for 15 min, which separated the supernatant (SOM: soluble organic matrix) and precipitated (IOM: insoluble organic matrix)

fractions. The insoluble fraction was desalted by successive centrifugation in distilled water, and lyophilized.

- **Extraction of lipidic fraction in biomineral sample**

Powder sample was soaked in warm chloroform/methanol (1:1v/v) for three days, under a mild and constant stirring, and sonicated every day. The mixture was then centrifugated at 4500 xg for 15 min to separate the powder and insoluble parts from the solvent –soluble part.

### **2.3 Techniques - structural characterization**

- **X-Ray diffraction**

XRD was performed with a  $\theta$ - $2\theta$  conventional diffractometer (Siemens D-500) with Mo  $K\alpha$  radiation (0.709 Å) and with  $\theta$ - $2\theta$  conventional diffractometer (Seifert X3000) with Cu  $K\alpha$  radiation (1.5418 Å). For XRD analysis, 200 mg of each sample were lightly ground in agate mortar and was packed into the sample holder for X-Ray diffraction analysis, for the Seifert diffractometer the sample was packed into zero-background sample holder.

The particle size of sample was estimate from the full-width at half maximum (FWHM) of most intense peak according to the Debye-Scherrer formula. The exactly FWHM and peak position was obtained by a non linear fitting of the XRD spectra with Log Normal function using Origin 5.0 program from Microcal Software.

- **Infrared Spectroscopy**

Fourier transform Infrared (FT-IR) spectra were collected in the Mid region from  $400\text{ cm}^{-1}$  to  $4000\text{ cm}^{-1}$  at  $4\text{ cm}^{-1}$  resolution over 64 averaged scans using a Bruker Equinox 55 spectrophotometer. For FT-IR analysis of solids, 10 mg of solid sample was ground in an agate mortar with 30 mg of KBr and pressed; liquid samples were analyzed adding a drop of liquid between two KBr windows.

- **Nuclear Magnetic Resonance**

High-resolution NMR spectra were collected using a Varian Unity Inova spectrometer with a 9.39 T wide-bore Oxford magnet operating at a proton frequency of 399.952 MHz. Solid state analysis was performed using solid state 4 mm probe solid state; liquid samples were analyzed in a 5 mm indirect, PFG (15N-31P) and VT probe.

$^{13}\text{C}$  Magic Angle Spinning (MAS) experiments for solids were performed packing using ~ 100 mg of sample lightly ground in agate mortar and packed into a 4 mm  $\text{Si}_3\text{N}_4$  rotors, 7 kHz spin rate, recycle time 1, 5, 100, 700 and 1200 s, 7.5  $\mu\text{s}$  pulse length ( $90^\circ$ ) and 50 kHz spectral window.

$^{13}\text{C}$  Cross Polarization Magic Angle Spinning (CPMAS) spectra were collected with contact times of 0.3, 1, 2, 4, 8 and 16 ms, and a recycle time of 2 s.  $^{13}\text{C}$  chemical shifts were referenced externally to hexamethylbenzene ( $\text{CH}_3 = 17.4\text{ ppm}$ ).

The species distributions in  $^{13}\text{C}$  CPMAS experiments were obtained by a non linear fitting of the NMR signals to individual Gaussian by means of the Origin 5.0

program from Microcal Software, in the fitting procedure, the position, line width, and intensity were varied to find the best fit curve to the experimental spectrum.

$^1\text{H}$  experiments were carried out with the sample contained in a 5 mm tube using 7  $\mu\text{s}$  pulse ( $90^\circ$ ), 2 s repetition time, and spectral width of 4 kHz. The NMR experiments used for proton resonance assignments also included magnitude Correlation Spectroscopy (COSY) (Aue et al., 1976).

$^{13}\text{C}$  spectra were recorded at the frequency of 100.564 MHz using a spectral width of 20 kHz and  $90^\circ$  pulse.  $^{13}\text{C}$  assignments were made from Heteronuclear Multiple Bond Coherence (HMBC) (Wilker et al., 1993) and Heteronuclear Single Quantum Coherence (HSQC) (Kay et al., 1992) spectra. Chemical shifts in all spectra were referenced to DSS (2,2-dimethyl-2-silapentane-5-sulfonate).

The concentration of phthalate in hydrozincite synthesis has been calculated using the Internal Standard Method. To obtain the absolute concentration of our compound in the NMR sample, the area of the signals have been compared to the area of a reference (pure methanol, Aldrich 99,99%) with known concentration.

## • HR-Transmission Electron Microscopy

HRTEM images were collected using JEM 2010UHR (Jeol) microscope with a LAB6 thermoionic source operating at 200kV and equipped with a Gatan imaging filter (GIF). Energy-filtered images were acquired using 3 mm GIF entrance aperture and a slit width of 15 eV. All high-resolution images were acquired digitally using 1 or 2 sec of exposure and 1x binning (1024 x 1024 pixels) of the charge-coupled-device (CCD) camera.

The samples were lightly ground in an agata mortar and were disperse in octane (or distilled water) and further submitted to an ultrasonic bath. The suspensions were then dropped on carbon coated copper grids for high-resolution transmission electron microscopy. A fast Fourier transform (FFT) was calculated on the images by using the Digital Micrograph (JEOL) software. Because of the ~19x magnification between the TEM viewing screen and the CCD camera, a preliminary calibration using a standard gold sample was performed to obtain corrected values of d-spacing in the samples.

- **Scanning Electron Microscopy**

Surface morphological analyses were investigated with an environmental scanning electron microscope (ESEM QUANTA 200, FEI, Hillsboro, Oregon) (SEM) working at 25 kV electron accelerating voltage. The samples were prepared by mounting onto aluminium stubs and carbon-coated with a layer about 10 nm thick by using metal-coating plant under a vacuum of 0.01 Pa ( $10^{-4}$  Torr).

## **2.4 Analytical analysis**

The major elemental concentrations were determined by inductively plasma atomic emission spectrometry (ICP-AES; FISION-ARL3520).

Carbon and nitrogen content were obtained by using FIsion Instruments 1108 CHNS (T = 1000°C) elemental analyzer.

Other trace elemental concentrations were determined by inductively-coupled plasma-mass spectrometry (ICP-MS; Perkin-Elmer; ELAN 5000).



## 2.5 References

- Aue, W., Bartholdi, E. and Ernst, R. R. Two-dimensional spectroscopy. Application to nuclear magnetic resonance *J. Chem. Phys.*, 64, 2229-2247 (1976).
- Boni, M., Gilg, H.A., Aversa, G., and Balassone, G. The "calamine" of southwest Sardinia: Geology, mineralogy and stable isotope geochemistry of supergene Zn mineralization products. *Economic Geology*, 98, 731-748 (2003).
- Garcia-Clavel, M., Martinez-Lope, M.J., and Casais-Alvarez, M.T. thermoanalytical study of the system  $Pb^{2+}$ - $Zn^{2+}$  coprecipitated as binary carbonates. *Thermochim. Acta*, 137, 177-187 (1989).
- Kay, L.E., Keifer, P. and Saarinen, T. Pure absorption gradient enhanced heteronuclear single quantum correlation spectroscopy with improved sensitivity. *J. Am. Chem. Soc.*, 114, 10663–10664 (1992).
- Pala, A., Costamagna, L. G., and Muscas, A. Valutazione delle riserve idriche nei bacini dei Rii Piscinas e Naracauli (Sardegna Meridionale). *Boll. Soc. Geol. Ital.* 115, 717-735 (1996).
- Paquette, J., and Reeder, R.J. Relation hip between surface structure, growth mechanism, and trace element incorporation in calcite. *Geoch. et Cosmoch. Acta*, 59, 735- 749 (1995).
- Podda, F., Zuddas, P., Minacci, A., Pepi, M., Baldi, F. Heavy Metal Coprecipitation with Hydrozincite  $[Zn_5 (CO_3)_2(OH)_6]$  from Mine Waters Caused by Photosynthetic Microorganisms. *Appl. Environ. Microbiol.* , 66, 5092–5098 (2000).
- Music, S., Popovic, S., Maljkovic, M., Dragcevic, D. Influence of synthesis on the formation and properties of zinc oxide. *J. Alloys and Comp.*, 347,324-332 (2002).

Willker, W., Leibfritz, D., Kerssebaum, R., Bermel, W. Gradient selection in selection in inverse heteronuclear correlation spectroscopy. *Magn. Reson. Chem.*, 31, 287–292 (1993).

# Chapter III High Resolution Solid-State <sup>13</sup>C Nuclear Magnetic Resonance Spectroscopy

---

## 3.1 Introduction

The utilization of Nuclear Magnetic Resonance (NMR) techniques for the structural characterization has a very long tradition (Kogel-Knabner, 1997; Wilson et al., 1981). The advent of modern solid-state NMR spectrometers, which are capable of producing liquid-like spectra, ushered in a new era of organic matter characterization. A major attraction of this technique is the fact that samples can be analyzed often times without any prior pretreatment, thus rendering solid state NMR a non-destructive approach to characterization without the production of artifacts.

Although solid-state NMR spectroscopy has these added advantages, several disadvantages do exist. Larger quantities of material are needed to perform NMR in the solid-state (~ 70-200 mg). Already an insensitive technique, solid-state NMR gives very low and broad signals such that much more accumulation time is needed to obtain spectra with reasonable S/N ratios. Despite these limitations, several techniques have been developed to overcome these shortcomings, principally cross-polarization with magic angle spinning (CPMAS) and high power proton decoupling (HPDEC). The theory of NMR has been widely reported and the following discussion will be adopted from several sources (Hays, 1982; Schaefer et al., 1975).

<sup>13</sup>C is the most common nucleus studied in geochemical materials and the focus of this dissertation, although a variety of other nuclei such as <sup>15</sup>N and <sup>31</sup>P are available for investigation. Since NMR is considered an insensitive technique, the

concentration of the particular element under study in the sample, as well as its natural abundance, is of importance. Also, characteristics of the nuclei of interest are critical such as the gyromagnetic ratio,  $\gamma$ , where nuclei with small values are much more difficult to detect because they have small nuclear dipole moments.

### 3.2 Magic Angle Spinning

One of the problems encountered in solid-state NMR spectroscopy is that of chemical shift anisotropy (CSA). It has been shown (Wilson, 1987) that the chemical shift observed in the solid state can be expressed as:

$$\sigma_{\text{obs}} = 3/2\sigma_{\text{iso}}\sin^2\theta + 1/2(3\cos^2\theta - 1) \sum_p \sigma_p \cos^2\chi_p$$

where  $\chi_p$  are the angles of the nuclei axes of rotation to the principal axes and  $\sigma_p$  are the various chemical shift tensors. Since chemical shift is a tensor, there are three chemical shift components (x,y,z planes), which in most cases are not identical. Upon performing NMR on static samples where all possible orientations of these tensors exist, powder patterns are produced which are associated with broad resonances due to this anisotropy.

In order to remove CSA, the sample is spun at the magic angle of  $54.7^\circ$  relative to the external magnetic field  $B_0$  (z axis) (Schaefer and Stejskal, 1976; Schaefer and Stejskal, 1977). The effect on the chemical shift can be understood mathematically that if  $\theta = 54.7^\circ$ , we recognize that  $3\cos^2(54.7)-1$  is equal to zero.

Then  $\sigma_{\text{obs}} = \sigma_{\text{iso}}$ .  $\sigma_{\text{iso}}$  is the isotropic chemical shift characterized by sharp resonances which are naturally obtained in solution-state NMR where molecular tumbling allows for these orientational effects on chemical shifts to be averaged.

Therefore, MAS mimics this molecular motion and allows liquid-like spectra to be obtained on solid samples.

Since the chemical shift of a particular  $^{13}\text{C}$  environment is dependent on the orientation of the parent molecule with respect to the external magnetic field, the MAS rate must have a greater frequency than the frequency range of the chemical shift in the static powder sample. If this is not the case, several spinning sidebands will be observed in addition to a sharp central peak for a particular chemical shift. These sidebands are located on both sides of the center signal at integral multiples of the MAS rate and extend over the entire frequency range of the chemical shift in the static solid state spectrum.

### 3.3 High Power Proton Decoupling

High power proton decoupling (HPDEC) (Bloch, 1958), in conjunction with magic angle spinning, removes  $^{13}\text{C}$ - $^1\text{H}$  dipolar interactions. These same interactions, which allow for efficient cross-polarization, also cause severe broadening in solid-state spectra due to the 99% abundance of the  $^1\text{H}$  nucleus. As the  $^{13}\text{C}$  nucleus is rare, almost all of this broadening arises from interaction with neighboring protons. Proton decoupling in solution-state NMR is a familiar technique, but the application to solids requires much greater power (100W vs. 10W or less) because the  $^{13}\text{C}$ - $^1\text{H}$  interaction is much stronger. HPDEC is achieved by applying continuous high power at frequencies comparable to the proton line widths, usually tens to hundreds of kHz (Schaefer et al. 1975), for the whole duration of  $^{13}\text{C}$  data acquisition.  $^{13}\text{C}$ - $^1\text{H}$  dipolar interactions result from the through space interaction between  $^{13}\text{C}$  and  $^1\text{H}$  magnetic dipoles. This interaction modifies the  $^{13}\text{C}$  spectrum because  $^1\text{H}$  dipoles change the effective  $B_0$  at the  $^{13}\text{C}$  nucleus by adding to it ( $^1\text{H}$  dipoles align with  $B_0$ ) or by subtracting from it ( $^1\text{H}$  dipoles align against  $B_0$ ). The

magnitude of the interaction is dependent on the distance between carbons and protons and on their orientation with respect to  $B_0$ . The dipolar interactions spread a particular

$^{13}\text{C}$  NMR frequency over a wide range in the solid-state  $^{13}\text{C}$  NMR spectrum. HPDEC effectively flips the  $^1\text{H}$  dipoles rapidly, aligning them with and against  $B_0$ , thus averaging the dipolar  $^{13}\text{C}$ - $^1\text{H}$  interaction. The frequency range of carbon functional groups, which experience dipolar interactions, now spans a smaller range, and thus narrower resonances can be observed.

### 3.4 Cross-Polarization

Cross-polarization allows the low natural abundance of the  $^{13}\text{C}$  nucleus to be overcome in a way far superior to DP-MAS (Direct Polarization). Unlike solution state NMR, proton NMR in the solid-state of these materials gives broad, featureless signals due to very strong  $^1\text{H}$ - $^1\text{H}$  dipolar interactions (Sullivan and Maciel, 1982). The cartesian coordinate representation for a typical CPMAS experiment is seen in Figure 3.1. When proton nuclei are placed in a magnetic field, the magnetic dipoles of these nuclei align themselves with (low energy) or against (high energy) the magnetic field,  $B_0$ , according to the Boltzmann distribution. However, as more nuclei align themselves in the low energy configuration, a net magnetization,  $M_{0\text{H}}$ , develops along the z axis. A  $90^\circ$  proton radiofrequency (rf) pulse is then applied along  $x'$ , after which each  $M_{1\text{H}}$  (proton magnetization) points along  $y'$ .

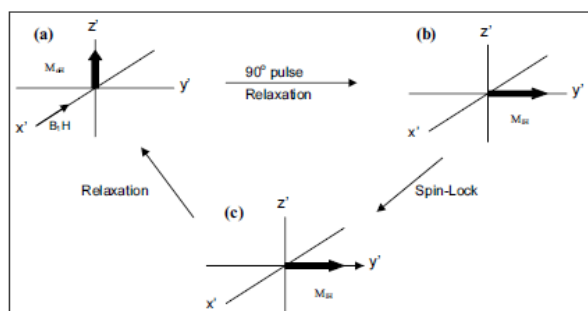


**Figure 3.1** Cross-Polarization scheme showing magnetization vectors during a CPMAS experiment: (a) proton magnetization along  $+z'$  axis at equilibrium (b) magnetization tipped along  $y'$  after  $90^\circ$  pulse along  $x'$  from (a) (c) spin-locking of proton magnetization along  $y'$ .

An rf proton spin lock with magnitude  $B_{1H}$  is immediately applied along  $y'$  such that the magnetization  $M_{1H}$  is now forced to rotate (locked) about  $y'$  with a frequency given by:

$$\nu_{1\rho}H = \gamma_H B_{1H} / 2\pi$$

where  $\gamma_H$  is the gyromagnetic ratio of the protons. Without the presence of  $B_{1H}$ , each  $M_{1H}$  would spread out in the  $x'y'$  plane ( $^1H$  NMR plane) because each  $M_{1H}$  corresponds to a different  $^1H$  NMR frequency and each  $M_{1H}$  starts to move out of the  $x'y'$  plane because of spin-lattice ( $T_1$ ) relaxation. If  $B_{1H}$  is left on indefinitely, the magnitude of each  $M_{1H}$  will gradually decrease because of spin-lattice relaxation in the rotating frame ( $T_{1\rho}$ ) as well.

In the cross-polarization experiment, a  $^{13}C$  spin lock with magnitude  $B_{1C}$  is applied simultaneously along the  $x''y''$  plane ( $^{13}C$  NMR plane). If the magnitude of  $B_{1C}$  is adjusted to a matching condition known as Hartmann-Hahn (Hartmann and Hahn, 1962) given by:

$$\gamma_H B_{1H} = \gamma_C B_{1C}$$

where  $\gamma_H$  and  $\gamma_C$  are the gyromagnetic ratio of proton and carbon, respectively, and  $B_{1H}$  and  $B_{1C}$  represent the spin locking rf of protons and carbons, respectively, then a rapid transfer of magnetization between  $^1\text{H}$  and  $^{13}\text{C}$  can occur. Since at the start of the  $^1\text{H}$  and  $^{13}\text{C}$  spin locks,  $M_{1H}$  equals  $M_{oH}$  (proton magnetization along z axis before  $90^\circ$  pulse) and  $M_{1C}$  equals zero, magnetization is transferred from  $^1\text{H}$  to  $^{13}\text{C}$  nuclei.  $^{13}\text{C}$  dipoles that initially contributed towards  $M_{oC}$  are forced to re-orient themselves in a non-zero  $M_{1C}$  component at the expense of the  $^1\text{H}$  dipoles that contributed towards  $M_{1H}$ . This magnetization transfer is known as cross-polarization (Pines et al., 1973) and is defined by a time constant  $T_{CH}$ .

The time duration of the matched spin locks is termed the contact time. At the end of the contact time, the spin locks are turned off and the  $^{13}\text{C}$   $M_1$  components are detected in the presence of high power proton decoupling. For CP from  $^1\text{H}$  to  $^{13}\text{C}$  with the matching condition met, the signal intensity of each  $^{13}\text{C}$  spectral component,  $M_{1C}$ , as a function of the contact time,  $t$ , is given by:

$$M_{1C}(t) = (M_{oC}\gamma_H/\gamma_C)/(1-T_{CH}/T_{1\rho H})[\exp(-t/T_{1\rho H})-\exp(-t/T_{CH})]$$

where  $M_{oC}$  is the magnitude of the equilibrium magnetization of each  $^{13}\text{C}$  species in  $B_o$  (external magnetic field) and is directly proportional to the concentration of each  $^{13}\text{C}$  species in the sample and  $T_{1\rho H}$  is the proton spin lattice relaxation in the rotating frame.

The CPMAS NMR experiment has many advantages over DPMAS. With CPMAS, a signal enhancement of up to four is possible given the gyromagnetic ratios of proton and carbon ( $\gamma_H/\gamma_C = 4$ ). Furthermore, the recycle delay necessary between



experiments ( $5 \sim T_{1H}$ ) is dictated by the longest  $^1\text{H}$   $T_1$  in the sample rather than the longest  $^{13}\text{C}$   $T_1$  as is the case for DP-MAS. Usually,  $T_{1H} \ll T_{1C}$ . Thus, more CPMAS experiments can be performed in a given time and the overall signal gain will be enhanced over DP-MAS. However, in order for the CP process to be successful,  $T_{CH} \ll t$  (contact time)  $\ll T_{1\rho\text{H}}$  for all  $^{13}\text{C}$  species present in the sample. Thus, cross-polarization is a competing process of  $M_{1C}$  growth based on  $T_{CH}$  and  $M_{1C}$  decay based on  $T_{1\rho\text{H}}$ .

Given the heterogeneous nature of geochemical materials, which give rise to broad NMR signals, a variety of  $T_{CH}$  values are expected to exist.  $T_{CH}$  depends on various factors including the nature of lattice motions in the sample, the spinning rate of the sample, which is especially true for non-protonated carbon nuclei, and the exactness of the Hartmann-Hahn match (Alemany et al., 1983). This cross-polarization rate is dependent not only on the number of bonded protons, but also has a  $r_{CH}$  (Wershaw, 1993) dependence (i.e. the distance between carbon and protons both inter- and intra-molecularly). Hence, non-protonated carbons polarize at a much slower rate than protonated carbons. Also, carbons which possess some mobility cross-polarize much slower due to attenuations in  $^{13}\text{C}$ - $^1\text{H}$  and  $^1\text{H}$ - $^1\text{H}$  dipolar interactions. For these circumstances, longer  $\tau_c$  are required to fully achieve cross-polarization at the expense of rigid, protonated carbon signals. Consequently,  $T_{CH}$  values go as:

**non-protonated C > mobile  $\text{CH}_3$  > protonated aromatic C, CH >  $\text{CH}_2$  > static  $\text{CH}_3$**

$T_{CH}$  values are constant for all spectrometers since dipolar interactions are independent of the external magnetic field provided that an exact Hartmann – Hahn match exists and the same MAS rates are used. If MAS rates were increased, an expected increase in  $T_{CH}$  would likely result. Carbon nuclei of low or remote protonation experience a much weaker  $^{13}\text{C}$ - $^1\text{H}$  dipolar interaction, and thus,  $T_{CH}$  may be long such that these carbon nuclei may not cross-polarize as efficiently

as protonated carbons. This results in intensity distortions and quantitation problems. Inefficient proton spin diffusion processes in proton-dilute samples also create difficulties in the effectiveness and linearity of the CP process by causing a decrease in  $^{13}\text{C}$ - $^1\text{H}$  Hartmann-Hahn matches if long enough recycle delays are not employed (Alemany et al., 1983). Also, intermolecular interactions may be comparable or even longer than intramolecular interactions for carbons separated from protons by three bonds or more causing poor cross-polarization which requires long contact times.

### **3.5 Relaxation Phenomena**

Like other spectroscopic techniques, solid-state NMR involves transitions between energy states. In NMR, a radiofrequency  $90^\circ$  pulse is applied to perturb magnetization away from an equilibrium position (along z axis with  $B_0$ ), and the decay back to this position can then be followed to give the NMR spin dynamics of the sample.

These spin dynamics give insights into structural properties of the sample such as its rigidity/mobility or crystalline/amorphous nature. These relaxation parameters can also give clues into environmental processes such as sorption of organic chemicals and metal binding to the macromolecules, minerals, soils or others. Spin dynamics are also useful in their own right as guidelines to optimize the CPMAS experiment.

#### **3.5.1 Transverse relaxation ( $T_2$ )**

Upon excitation of  $^{13}\text{C}$  or  $^1\text{H}$  nuclei, these nuclei may exchange energy with neighboring nuclei of the same kind in order to return to equilibrium along z. In

effect, a mutual flipping of the spins of the interacting nuclei results which is termed spin-spin or transverse relaxation ( $T_2$ ). This phenomenon occurs only between identical nuclei such that the  $M_x$  and  $M_y$  (magnetization in the xy plane) components of the total  $M$  magnetization are reduced with a time constant  $T_2$  according to:

$$Mt^{x,y} = M_0 e^{-t/T_2}$$

where  $Mt^{x,y}$  is the x and y components of the total magnetization,  $M_0$  is the equilibrium magnetization and  $t$  is a time unit. The rate of spin-spin relaxation is related to the line width at half height,  $\nu_{1/2}$ . However, due to imperfect magnetic field homogeneity, different regions of the sample experience slightly different frequencies, and thus shorter  $T_2$  values. Thus,

$$\nu_{1/2} = 1/\pi T_2 + \gamma \Delta B_0 / 2\pi$$

where  $\gamma \Delta B_0 / 2\pi$  describes this magnetic field inhomogeneity.

### 3.5.2 Transverse relaxation ( $T_1$ )

In addition to energy exchange with neighboring nuclei, energy exchange may also occur with the surroundings, or lattice. When a group of nuclei is placed in a magnetic field,  $B_0$ , a small equilibrium magnetization develops along the direction of  $B_0$  (z axis) given by the Boltzmann distribution. The rate at which  $M_z$  (magnetization in the z axis) approaches  $M_0$  (equilibrium magnetization) can be described as:

$$M_0 - M_z = Ce^{-t/T_1}$$

where C represents the degree of equilibrium attained by the magnetization at time, t, and  $T_1$  (spin-lattice relaxation), the rate at which the nuclei can transfer energy to the lattice.  $T_1$  measurements depend on the medium in which the measurement is made. Spin-lattice relaxation for solids is much longer (up to days) than for liquids ( $10^{-2}$  to  $10^2$  s).

Conversely,  $T_2$  values are generally much shorter than  $T_1$ , in any medium. A related relaxation rate is the spin-lattice relaxation rate in the rotating frame,  $T_{1\rho}$ . This time constant characterizes the decay of  $M_0$  in an applied field,  $B_1$ , which is much smaller than  $B_0$ . After a  $90^\circ$  pulse and spin locking, as discussed in the cross-polarization section of this text,  $B_1$  is turned off and the magnetization along y is allowed to decay. This decay is described by:

$$M_t = M_0 e^{-t/T_{1\rho}}$$

and given as being in the rotating frame because the effective field is now  $B_1$  and not  $B_0$ .

### 3.6 References

- Aleman, L. B., Grant, D. M., Pugmire, R. J., Alger, T. D., Zilm, K. W. J. Cross polarization and magic angle sample spinning NMR spectra of model organic compounds. 1. Highly protonated molecules. *J. Am. Chem. Soc.*, 105, 2133-2141 (1983).
- Aleman, L. B., Grant, D. M., Pugmire, R. J., Alger, T. D., Zilm, K. W. Cross polarization and magic angle sample spinning NMR spectra of model organic compounds. 2. Molecules of low or remote protonation. *J. Am. Chem. Soc.*, 105, 2142-2147 (1983).
- Bloch, F. Theory of Line Narrowing by Double-Frequency Irradiation. *Phys. Rev.*, 111, 841-853 (1958).
- Hays, G. R. High-resolution carbon-13 solid-state nuclear magnetic resonance spectroscopy. *Analyst*, 107, 241-252 (1982).
- Hartmann, S. R., and Hahn, E. L. Nuclear Double Resonance in the Rotating Frame *Phys. Rev.*, 128, 2042-2050 (1962).
- Kogel-Knabner, I. <sup>13</sup>C and <sup>15</sup>N NMR spectroscopy as a tool in soil organic matter studies. *Geoderma*, 80, 243-270 (1997).
- Pines, A., Gibby, M. G., Waugh, J. S. Proton-enhanced NMR of dilute spins in solids. *J. Chem Phys.*, 59, 569-590 (1973).
- Schaefer, J., Stejskal, E. O., Buchdahl, R. High-Resolution Carbon-13 Nuclear Magnetic Resonance Study of Some Solid, Glassy Polymers. *Macromolecules*, 8, 291-296 (1975).
- Schaefer, J., and Stejskal, E. O. Susceptibility studies of laccase and oxyhemocyanin using an ultrasensitive magnetometer. Antiferromagnetic behavior of the type 3 copper in Rhus laccase. *J. Am. Chem. So.* , 98, 1031-1032 (1976).

- Schaefer, J., Stejskal, E. O., Buchdahl, R. Magic-Angle  $^{13}\text{C}$  NMR Analysis of Motion in Solid Glassy Polymers. *Macromolecules*, 1977, 10, 384-405.
- Sullivan, M. J., and Maciel, G. E. Spin dynamics in the carbon-13 nuclear magnetic resonance spectrometric analysis of coal by cross polarization and magic-angle spinning. *Anal. Chem.*, 54, 1615-1623 (1982).
- Wershaw, R. Model for Humus in Soils and Sediments. *Environ. Sci. Technol.*, 27, 814-816 (1993).
- Wilson, M. A., Pugmire, R. J., Zilm, K. W., Goh, K. M., Heng, S., Grant, D. M. Cross-polarization  $^{13}\text{C}$ -NMR spectroscopy with 'magic angle' spinning characterizes organic matter in whole soils. *Nature*, 294, 648-650 (1981).
- Wilson, M. A. NMR Techniques and Applications in Geochemistry and Soil Chemistry; Pergamon Press: New York (1987).

## Chapter IV Structural and morphological properties of hydrozincite minerals

---

### 4.1 X-Ray Diffraction measurement

The crystal structure of hydrozincite was first studied in a geological sample by using single crystal X-ray diffraction (Ghose, 1964). The Figure 4.1 shows some of collected XRD patterns.

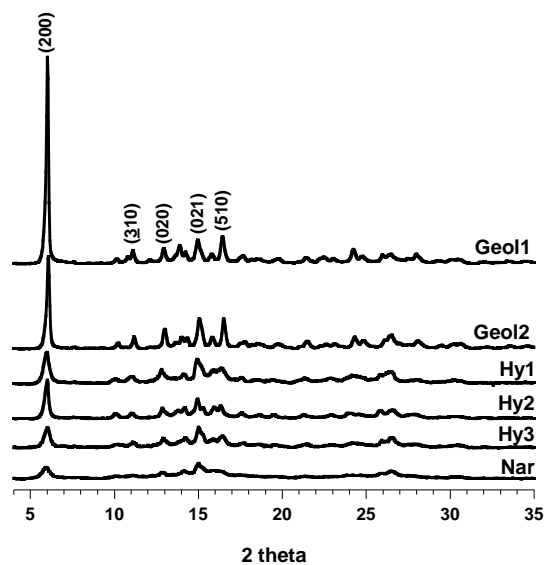


**Figure 4.1** XRD patterns of geological (Geol1 and Geol2), synthetic (Hy1, Hy2 and Hy3), and biomineral (Nar) samples. All the patterns are in agreement with expected hydrozincite diffraction pattern.

All observed Bragg reflections can be indexed as a hydrozincite single phase with a monocline structure, according to experimental (PDF Card 19-1458) and calculated (PDF 72-1100) reference patterns. The XRD patterns confirm the presence of only hydrozincite phase in the samples.

The  $I_{100}$  peak appears at  $2\theta \sim 6^\circ$  corresponds to the (200) hydrozincite main reflection. For the geological samples, the relative peak intensity for the (200) peak is much higher than reported for the monocline structure in the reference cards. This can be explained as a preferred orientation, in fact the preferred orientation can create a systematic variation in diffraction peak intensity, this information is in agreement with the {100} crystallographic form, as observed also by SEM (Fig. 4.3 a and b), at least for the Geol1 and Geol2 samples.

The diffraction spectra for the Geol1 and Geol2 samples present well-defined diffraction peaks, while peaks from the synthesized samples clearly show peak broadening, and the largest peak broadening for the biomineral sample (Nar). The broadening of the signals suggests a progressive decrease in the size of crystal-coherent domains.

If the crystallite is smaller than 120 nm the diffraction spectra present broad diffraction peaks, in this case it is possible to estimate the crystallite size by the full-width at the half maximum (FWHM) of the most intense peak, according to the Debye-Scherrer formula:

$$B_{\theta} \approx \frac{K\lambda}{\beta \cos \theta}$$

where  $K$  is the shape factor,  $\lambda$  is the x-ray wavelength, in Å,  $\beta$  is the line broadening at half the maximum intensity (FWHM) in radians, and  $\theta$  is the Bragg angle (Scherrer, 1918; Patterson, 1939). The fitting of XRD spectra has been made



by Origin 5.0 program from Microcal Software, for each collected diffraction spectra the dimension has been calculated by fitting of the main reflections.

The averages sized calculated on the main reflection were ~21 nm for Geol1, ~19 nm for Geol2, ~14 nm for Hy2, ~10 nm for Hy1, ~9 nm for Hy3 and ~7 nm for Nar.

Thus, the progressive decrease in the size of crystal coherent domains should be dependent on the structural evolution of the minerals and/or on the crystallization process. Specifically, the persistence of the nanocrystals should be explained according to the mechanism on an imperfect oriented aggregation of nanoparticles (Meldrum and Cölfen, 2007).

## **4.2 Infrared Spectroscopy investigation**

Infrared spectroscopy is usually applied in the investigation of both inorganic and organic materials (Hasse et al., 2000; Wang et al., 2003). It allows the identification of characteristic functional groups in molecules that correspond to specific molecular vibrations (Conley, 1966). In addition, sampling is easy and requires a small amount of materials (about 1 mg). FT-IR has also been applied for comparing the organic composition of different molluscan shells (Dauphin, 1999; Dauphin et al., 2008). The main features of all FT-IR spectra in the range 400 – 1800  $\text{cm}^{-1}$  are shown in the Figure 4.2.

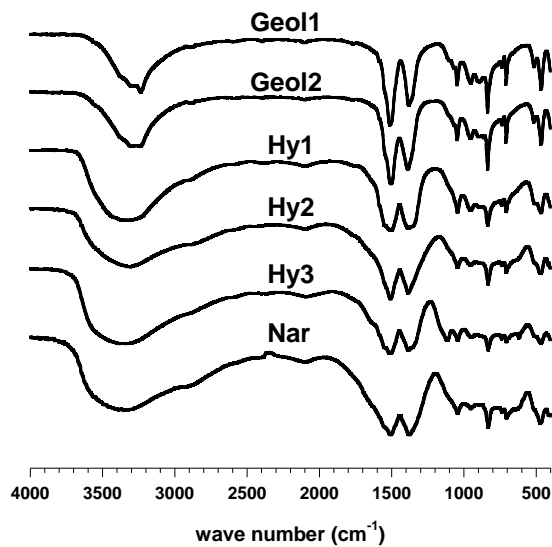


**Figure 4.2** FT IR spectrum for geological samples (Geol1 and Geol2), synthetic samples (Hy1, Hy2 and Hy3), and biomineral sample (Nar).

The carbonate vibrational stretching and bending of hydrozincite are attributed in comparison with the literature attributions (Music' et al., 2002), and the main peaks are shown in Table 4.1. For comparison the IR peaks of carbonate groups taken from (Music' et al., 2002) are show in the Table 4.1. The four peaks in the region 1520–1390  $\text{cm}^{-1}$  are ascribed to the asymmetric  $\text{CO}_3^{2-}$  stretching  $\nu_3$  mode (the correlation field splitting is well observed in the spectrum). The peak at 1047  $\text{cm}^{-1}$  is assigned to the  $\nu_1$  symmetric  $\text{CO}_3^{2-}$  stretching mode. The strong and sharp peaks at 836  $\text{cm}^{-1}$  is assigned to  $\nu_2$  out-of-plane OCO bending mode and that at 709  $\text{cm}^{-1}$  is assigned to  $\nu_4$  asymmetric OCO bending mode. All the samples show bands in the range 2900-3600  $\text{cm}^{-1}$  which can be ascribed to the water molecules and to the OH stretching modes. Both museum samples exhibit in the 2900-3600

cm<sup>-1</sup> region a broad signal with on the top three peaks observed at 3235, 3298, 3382 cm<sup>-1</sup> in Geol1 and at 3235, 3301, 3379 cm<sup>-1</sup> in Geol2.

Mode	Z4 <sup>a</sup>	Geol1	Geol2	Hy1	Hy2	Hy3	Nar
v1	1047	1047	1047	1046	1046	1046	1046
v2	837	836	836	835	835	834	835
v4	710	709	709	709	709	709	709
v3	1362	1363	1351	1354		1355	1345
v3	1387	1389	1389	1386	1382	1386	1380
v3	1511	1506	1501	1505	1508	1510	1509
v3	1549	1548	1546	1547	1550	1555	1556
vOH	3234	3235	3235	3300	3300	3368	3369
	3303	3298	3301	3562	3566	3569	3569
	3363	3282	3379				

**Table 4.1** FT IR frequencies (cm<sup>-1</sup>) of Hydrozincite samples compared with sample Z4 taken from Music' et al. (2002).

These peaks are in very good agreement with that reported in literature: 3234, 3303 and 3363 cm<sup>-1</sup> (Music et al., 2002) and attributed to the structured OH groups in hydrozincite. In this mineral, two oxygen atoms of the carbonate group are bonded to an octahedral and tetrahedral zinc atom each, whereas the third oxygen atom is hydrogen bonded to three OH groups. The hydrogen bonds present are of different strength, in spite of the similar hydrogen bond lengths, due to the different hydrogen bond acceptor strengths of the carbonate oxygen atoms (Schmidt and Lutz, 1993). This means that the stretching vibrations of the structural OH groups in hydrozincite should show three types of interactions in chemical bonding. In the IR spectrum of all the other samples in Figure 4.2, two broad bands centred at about 3500 cm<sup>-1</sup> and 3300 cm<sup>-1</sup> can be observed. These indicate the presence of

large amount of adsorbed water on the surface of the hydrozincite. The broad absorption bands at  $1640\text{ cm}^{-1}$ , assigned to the bending of water molecules, demonstrate the presence of molecularly adsorbed water in the crystal. The stretching vibrations corresponding to the structural OH group, which contributes to the IR band between  $3200 - 3400\text{ cm}^{-1}$ , are not resolved in these samples.

The geological samples present a gradual separation of the IR bands corresponding to the structural OH groups in  $[\text{Zn}_5(\text{CO}_3)_2(\text{OH})_6]$ . Zabinski (1964) investigated the IR spectra of several hydrozincite minerals from different localities. Hydrozincite mineral from Dorchester showed a broad IR band centred at  $3450\text{ cm}^{-1}$ , whereas the best crystallized hydrozincite mineral from Sedmocislenici showed well-resolved IR band at  $3230$  and  $3303\text{ cm}^{-1}$  and a weak shoulder at  $3350\text{ cm}^{-1}$ . This author concluded that the change in the microstructure of hydrozincite caused this effect in the corresponding spectra. According to this author, hydrozincite consist essentially of  $\text{Zn}_5(\text{OH})_6\text{O}_2^{4-}$  sheets with additional Zn atoms and  $\text{CO}_3$  groups above and below these sheets. The carbonate group hold these sheets together and, consequently, a deficiency of carbonate groups in hydrozincite facilities a disorder in the layer sequence. This means that the disorder crystal structure of hydrozincite influences the FT-IR spectrum as observed in the biomineral sample, in fact the spectrum showed a poor crystallinity respect the synthetic and in particular respect the geological samples. With an increase in the staking disorder the hydrogen bonds become elonged for different amounts in the various sheets and the corresponding IR bands are broadened and shifted toward higher wave number (Music' et al., 2002).

### **4.3 The morphologies analyzed by Scanning Electron Microscopy**

The morphological features of the samples studied are significantly dependent on the mineral growth process. Geol1 and Geol2 show globular aggregates (Fig. 4.3 a) and crystals are characterized by a platelet shape (Fig. 4.3 b), probably caused by the association of crystallographic forms {100} and {010}. Samples grown under a condition of inorganic synthesis show acicular crystals (Fig. 4.3 c) having a short side typically 100 and 200 nm in length, while the largest side is 2-10  $\mu\text{m}$  and platelet shaped (Fig. 4.3 d). Synthetic crystals show shapes and sized similar to the geologically occurring crystals. The distinctive feature of the Naracauli samples is that the hydrozincite form a packed network (Fig. 4.3 e) and encrust cyanobacteria sheaths (Fig. 4.3 f). The crystals of the Nar samples show a platelet shape (Fig. 4.3 g) having the shortest side typically 50-100 nm long. These crystals are misaligned and form mesoporous aggregate having a sponge-like surface. In addition, some filaments of organic material are clearly visible between sheaths (Fig. 4.3 g) and sometime protrude out from the inner sheaths.

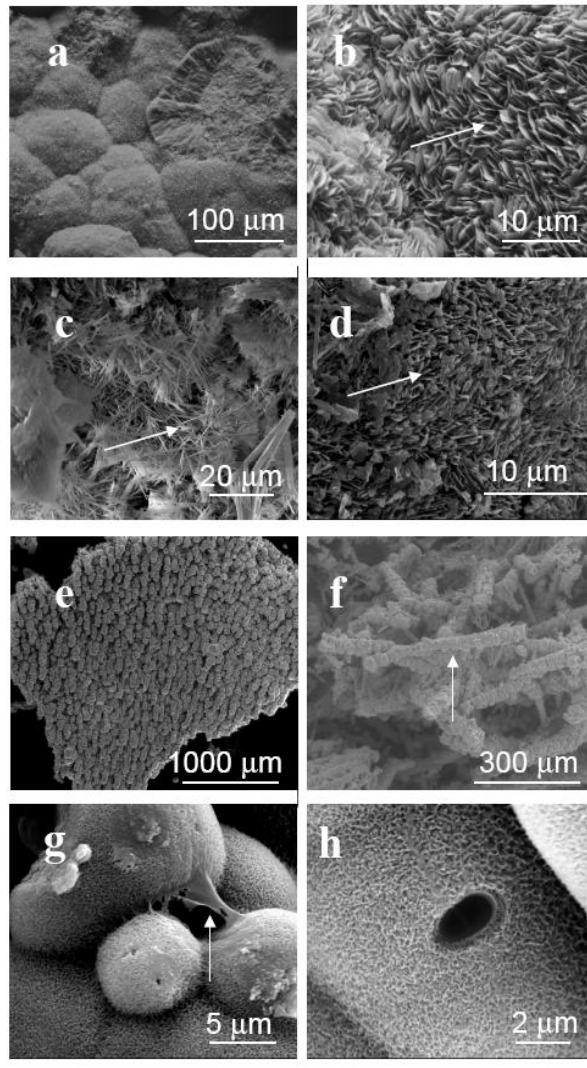


**Figure 4.3** SEM images of Geologic sample Geol1 (a and b), synthetic sample Synth2 (c and d), and Naracauli natural biomineral (Nar). Morphological units flattened on {100} can be recognized for all samples. The morphology of Nar sample is characterized by sheaths and sole organic matter filaments.

#### 4.4 HR - Transmission Electron Microscopy structural informations

A representative HRTEM micrograph of geologic samples is provided in Figure 4.4 image a and b, where a low magnification image (Fig. 4.4 a) of the Geol1 sample shows a euredral particle. Due to the thickness of these well crystallized particles, only the extreme edge is transparent to electrons in high-resolution mode at high magnification (Fig. 4.4 b). The image of figure 3.4 b shows nanocrystalline domains larger than 5 nm with a grain boundary network. The observed nanocrystals exhibit the lattice plane distance of 2.85 Å, which corresponds to the (220) hydrozincite planes, as calculated by fast Fourier transform (FFT) in the inset (Fig. 4.4 b). Representative images of the Nar sample are show in Figure 4.4 c, with the FFT in the figure 4.4d (inset). The particle size distribution of the Nar sample, calculated on about 2000 particles observe in dark-field images, is reported in Figure 4.4 d. The average particle size is about 3-4 nm and the particle size distribution is narrow. TEM results are in good agreement with FWHM from XRD; the value (3-4 nm), lower than the average crystallites size determined by XRD (7 nm), could be the result of the presence of some attached isoriented primary nanoparticles. In the literature were reported to spontaneously self-organized to a superstructure with a common crystallographic orientation in a process called "oriented attachment" (Banfield et al., 2000; Meldrum and Cölfen, 2007). Figure 4.4 c (inset 1 and 3) clearly indicates that nanocrystals can aggregate by fusion at the grain boundaries. Sometimes misalignment between crystallites falls below 10°. More often nanocrystals sharing some of the atomic position at their grain boundaries show misalignment higher than 10°. The fusion process should be able to decrease the excess of surface free energy and then stabilize the nanocrystals. According to Meldrum and Cölfen (2007) the platelet observed by SEM can be consider as a

mesocrystals produced by imperfect oriented aggregation of the nanocrystals observed by TEM. In the Nar sample, the aggregation and fusion process cannot be scaled up and mesocrystals are only platelets observed in Figures 1 g and h. In high resolution mode, some nanocrystals are observed with the lattice plane distance of 2.72 and 3.14 Å corresponding to the (021) and (020) hydrozincite planes. In comparison with geologic samples, the Nar sample show lattice defects, which can be related to the presence of staking modes (Fig. 4.4 c inset 2), in addition to nanocrystals in contact through grain boundaries. An HRTEM image of Hy2 sample is show in Figure 4.4 e with the FFT in the inset. The HRTEM image show grain boundaries and lattice defects, which can be ascribed to the presence of stacking modes on the basis of the typical streaking of the reciprocal rows observed in the FFT.



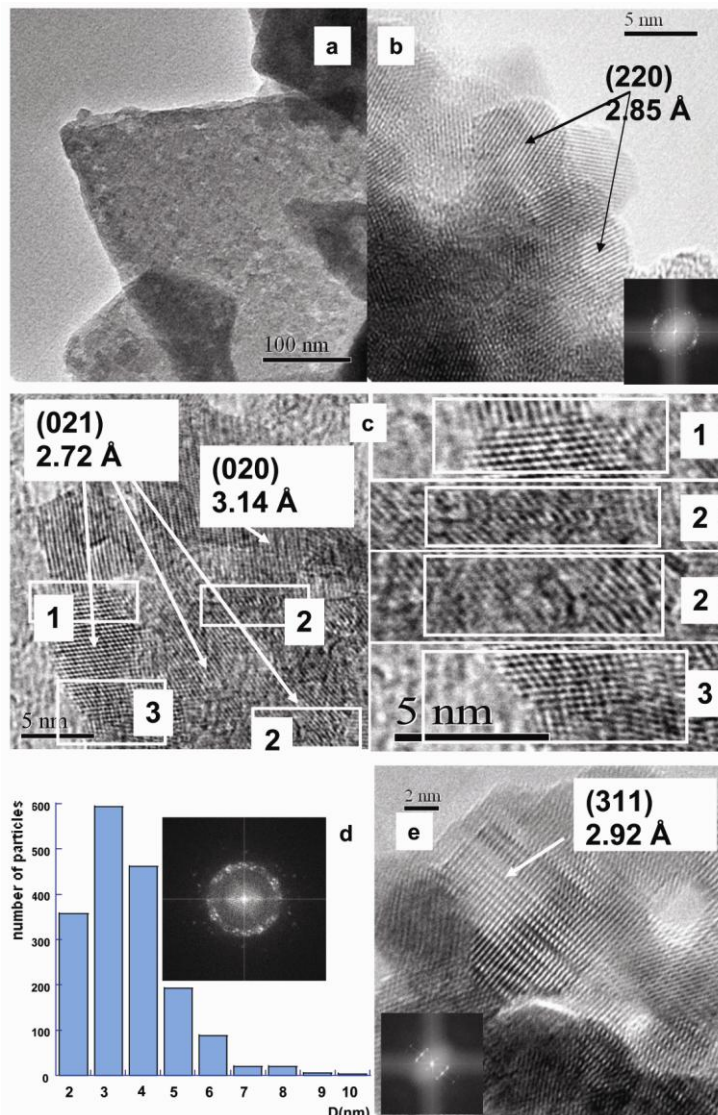


**Figure 4.4** HRTEM images: Geol2 sample at low (a) and high magnification with FFT in the inset (b); Nar sample at high magnification (c-left) where lattice defects as grain boundaries (1,3) and stacking modes (2) are evidenced (c-right); FFT of Nar sample and particle size distributions(d); Hy1 sample at high magnification with FFT in the inset (e).

## 4.5 Solid State Nuclear Magnetic Resonance

$^{13}\text{C}$  NMR spectroscopy has been a routine tool of organic chemistry for many years, but there has been little investigation of the  $^{13}\text{C}$  behavior of inorganic phase. The first paper regarding the mineral carbonate with biogenic origin has been published in the 1989 (Papenguth et al., 1989).

The information that we obtain from a solid-state NMR spectrum concern the presence of polytypes, different number of lattice defects in the sample, namely plane defects such as stacking faults (Tateyama et al., 1997; Harris, 2004). This because NMR spectra are influenced by the local environment, extending to only few spheres of coordination, so long-range order is not required to produce a signal. The local environment can lower the local symmetry, thus affecting the individual chemical shift and broadening of the observed peak, which are the result of a superposition of the signals arising from all the carbon atoms in given sites (Mehring, 1983; Engelhardt, 1987).

### 4.5.1 $^{13}\text{C}$ MAS experiments

The  $^{13}\text{C}$  NMR experiments were collected with different relaxation delay, between 0.2 s and 1200 s. The Figure 4.7 and Figure 4.8 show the  $^{13}\text{C}$  spectra of the samples Geol1, Geol2, Hy1, Hy2, Hy3 and Nar collected with 5 s and 1200 s. In the spectra of Geol1 and Geol2, shown in the Figure 4.7 and collected with 5 s of relaxation delay, a peak with FWHM of  $\sim 1$  ppm is present at 163.8 ppm. Figure 4.7 shows that no signals are observed in the spectra of Hy1 and Hy3, while a large featureless signals is observed in the spectrum of Hy2 in the range 160-168 ppm. The spectrum of Nar sample shows overlapping signals falling in the 162-169 ppm range, with a main signal at  $\sim 164$  ppm.

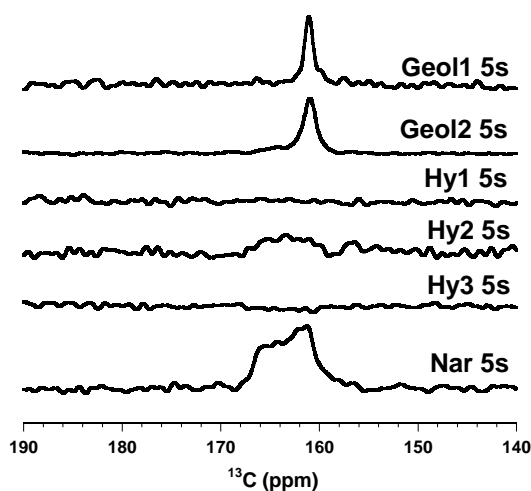


**Figure 4.7**  $^{13}\text{C}$  MAS NMR spectra of geologic samples (Geol1 and Geol2), synthetic samples (Hy1, Hy2 and Hy3), and biomineral sample (Nar). The spectra were collected at two relaxation delay of 5 s. All spectra have 50Hz line broadening.

The spectra Geol1 and Geol2 collected with 1200 s of relaxation delay are shown in the Figure 4.8.

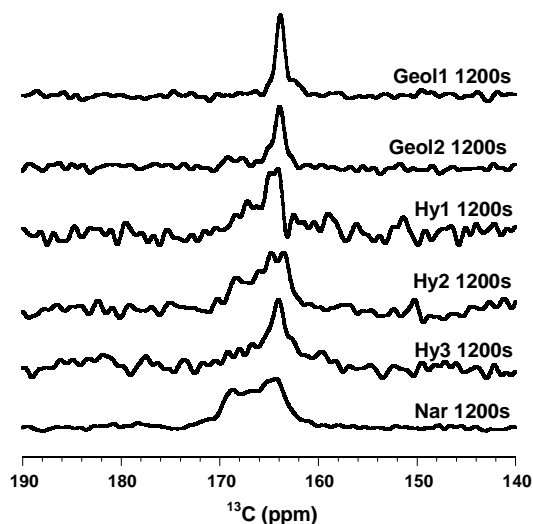


**Figure 4.8**  $^{13}\text{C}$  MAS NMR spectra of geologic samples (Geol1 and Geol2), synthetic samples (Hy1, Hy2 and Hy3), and biomineral sample (Nar). The spectra were collected at 1200 s. All spectra have 50Hz line broadening.

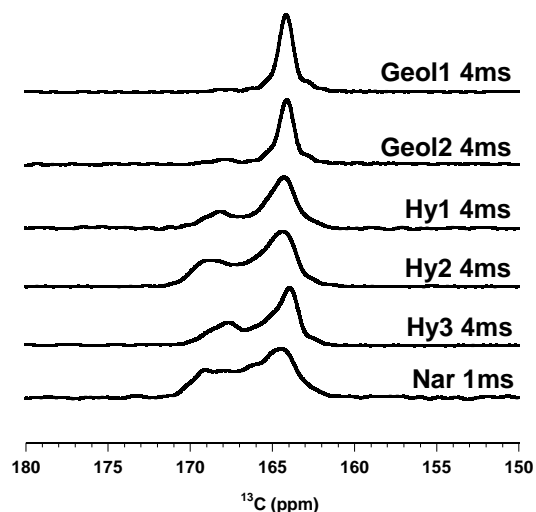
The samples collected at 1200 s of delay show a main peak at 164 ppm, such as that observed in the spectra collected with 5 s of relaxation delay (Fig. 4.7); however, small shoulders at both low and high frequencies can now be identified. In addition, a small high frequencies signal at 168 ppm can be observed in the spectrum of Geol1. The spectrum of Hy1 collected with 1200 s of relaxation delay (Fig. 4.8) present overlapping signals in the range between 163-169 ppm, the spectra of Hy2 and Hy3 show similar features to those of Hy1; however the peaks in the range 165.5-169 ppm are broader. The spectrum of the Nar sample shows

the same features under both delay conditions. As observed in Figure 4.8, even the use of a very long relaxation delay (1200 s) gives  $^{13}\text{C}$  MAS NMR spectra of low quality.

#### 4.5.2 $^{13}\text{C}$ CPMAS experiments

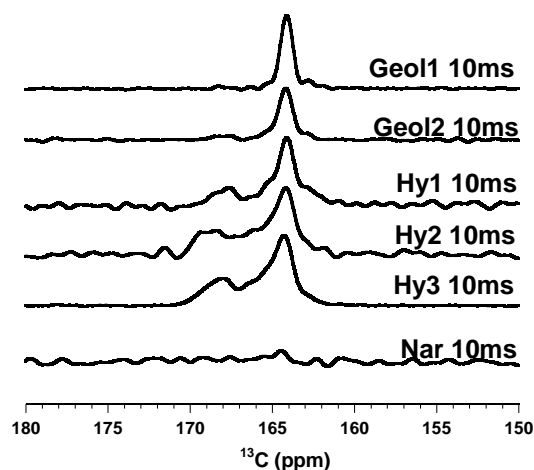
The use of  $^{13}\text{C}$  Cross-Polarization Magic Angle Spinning (CPMAS) technique gives spectra with a better signal to noise ratio (Fig. 4.9 and 4.10). The CPMAS technique is also useful for detecting biopolymers (Ueyama et al. 1998; Takahashi et al., 2004). The  $^{13}\text{C}$  CPMAS NMR spectra should be effective for the organic components which have many protons, in fact in the  $^1\text{H}$ - $^{13}\text{C}$  Cross-Polarization experiment the proton magnetization transfer to a carbon nucleus occurs during the contact time period and depend on the distance between the protons and carbon nuclei; moreover, it is governed by the characteristic proton spin-lattice relaxation time in the rotating frame ( $T_{1\rho}$ ) and  $^1\text{H}$ - $^{13}\text{C}$  cross polarization time.

Figure 4.9 shows the spectra collected with a contact time of 4 ms for Geol1, Geol2, Hy1, Hy2 and Hy3 and with 1 ms of contact time for Nar sample. The geological and synthetic samples show the maximum polarization time as 10 ms, while the natural sample present 1 ms of maximum polarization time.



**Figure 4.9**  $^{13}\text{C}$  CPMAS NMR spectra of geological samples (Geol1 and Geol2), synthetic samples (Hy1, Hy2 and Hy3) and biomineral sample (Nar). Geological and synthetic spectra collected with 4 ms and Nar sample collected with 1 ms of contact time. All spectra have 50-Hz line broadening.

In the experiments reported in the Figure 4.9 and in the experiments with 10 ms of contact time (Fig. 4.10) the sample Geol1, Geol2, Hy1, Hy2 and Hy3 present overlapping signals in the 162-169 ppm range, whose the main signals appears at ~164 ppm. The Nar sample was not cross polarizable with a contact time of 10 ms. this because, as described above, the presence of paramagnetic impurities in the sample Nar induces a shortening of the  $T_{1\rho}$  relaxation process.



**Figure 4.10**  $^{13}\text{C}$  CPMAS NMR spectra of geological samples (Geol1 and Geol2), synthetic samples (Hy1, Hy2, Hy3) and biomineral sample (Nar) collected with 10 ms contact time. All spectra have 50-Hz line broadening.

#### 4.5.3 Individual Gaussian decomposition of $^{13}\text{C}$ CPMAS overlapped signals

The CPMAS NMR technique gives spectra with a better signals to noise ratio respect the MAS NMR experiment, for this reason, we consider the analysis of CPMAS spectra suitable to discriminate the single components of the overlapped signals, at least for the chemical shift of the different observed peaks. The overlapped signals collected with 4ms of contact time for the geological and synthetic samples were decomposed into individual Gaussian by using the Software package Origin 7 from Microcal. The Figure 4.11 shows the experimental and simulates spectra of the Geol1 (a), Geol2 (b), Hy1 (c), Hy2 (d) and Hy3 (e).

This approach has been used in literature either for the simulation of infrared and Raman spectra of hydrozincite and smithsonite systems (Hales and Frost, 2007) or NMR spectra as silicon carbide (Mykhaylyk, 2002). The information obtained (i.e., positions, FWHM, and chemical shift values of geological samples) were reported in the Table 4.3 The relative areas of the signals in the Table 4.3 should be taken with caution and only as an indication of the relative amounts of the different structural conditions.

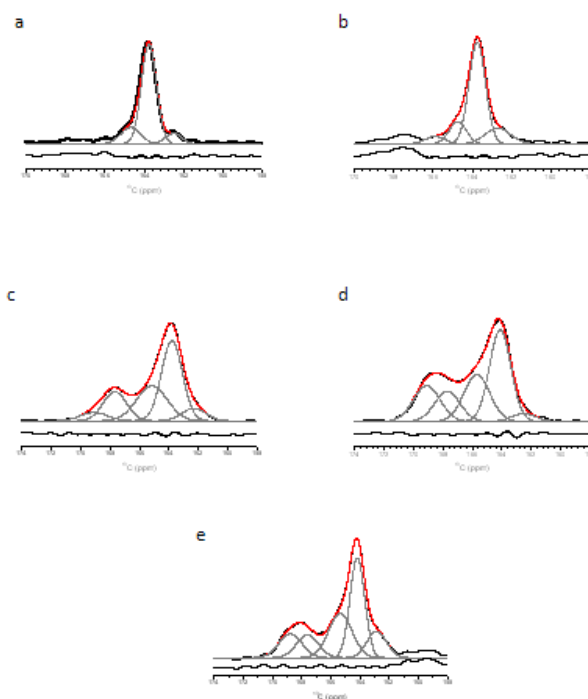


**Figure 4.11**  $^{13}\text{C}$  CPMAS NMR spectra of Geol1 (a), Geol2 (b), Hy1 (c), Hy2 (d) and Hy3 (e) samples. The species distributions in  $^{13}\text{C}$  CPMAS experiment of the samples were obtained by a nonlinear fitting of the NMR spectrum to individual Gaussians (grey curves). In the fitting procedure, the position, line width, and intensity were varied to find the best fit curve (red curve) to the experimental spectrum. The residuals were shown offset for clarity (black curve).



	Geol1	Geol2	Hy1	Hy2	Hy3
$\delta$	163.0±0.4	163.0±0.3	162.9±0.2	162.7±0.3	162.9±0.1
FWHM	1.21±0.06	0.92±0.08	0.93±0.07	1.62±0.08	1.33±0.01
%	13	10	9	4	11
$\delta$	164.1±0.3	164.1±0.2	164.2±0.2	164.3±0.1	164.2±0.2
FWHM	0.82±0.04	0.85±0.04	0.91±0.03	1.45±0.06	1.01±0.08
%	74	66	40	39	37
$\delta$	165.2±0.4	165.2±0.3	165.3±0.3	165.9±0.4	165.4±0.4
FWHM	1.23±0.06	0.91±0.07	1.34±0.07	1.72±0.09	1.61±0.04
%	13	15	24	23	26
$\delta$		167.9±0.4	168.0±0.3	168.0±0.4	167.6±0.4
FWHM		1.54±0.05	1.65±0.06	1.82±0.07	1.53±0.01
%		9	25	20	12
$\delta$			169.3±0.4	169.4±0.3	168.8±0.3
FWHM			1.55±0.08	1.57±0.05	1.57±0.05
%			2	14	14

**Table 4.3** Chemical shift (ppm), FWHM (ppm), and percentage of carbon CPMAS signals decomposed into individual Gaussians for geologic and synthetic samples collected with 4ms contact time.

The fitting results clearly show that the signals at 164 ppm are the main signals for all samples, as observed in the  $^{13}\text{C}$  MAS (Fig. 4.7 and 4.8) spectra. In the Geol1 samples two more signals were detected at ~163 and ~165 ppm, whereas in the Geol2 samples further signals is detected at ~168 ppm. In the spectra of both synthetic samples, more components are present, and a good simulation can be achieved using only five Gaussians at ~163, ~164, ~166, ~168, and ~169 ppm.

#### 4.5.4 Considerations on the overlapped signals

It is worth noting that, even though the hydrozincite structure (Ghose 1964) has only one crystallographically independent site for the carbon atom, but all MAS and CPMAS spectra in the Figure 4.4 and 4.5 show several peaks in the range 150-180 ppm, more dominant in the biomineral and synthetic samples. Several reasons can be taken into consideration to explain the presence of these additional signals:

1. The presence of paramagnetic metals can influence the chemical shift, the spin lattice relaxation time ( $T_1$ ) and the line with the carbon signals (La Mar et al. 1973). The amount of paramagnetic metal impurities in the Nar sample is lower than 0.3%, is below 0.1% in the Geol1 and Geol2 samples, and far below 0.1% in Hy1, Hy2 and Hy3 samples (Table 4.4). As consequence, since overlapping signals are present in Nar, synthetic samples, the presence of paramagnetic metal impurities cannot be responsible for the appearance of additional signals. It is worth noting that the spectra Hy1, Hy2 and Hy3 clearly show very broad signals at 5 s of delay (Fig. 4.7), whereas small peaks are observed with 1200s delay (Fig. 4.8). Thus large  $T_1$  characterizes the NMR signals of these samples. However, the spectrum of the Nar sample appears to be independent of the investigated delays, showing that the NMR signals are affected by short  $T_1$  (<5 s). Geological samples show a slight dependence on the experimental delay. This seems to indicate that samples having low paramagnetic metal impurity content show dependence on relaxation delay (synthetics), samples having high concentration impurities contents show very little dependence (Nar), and samples of intermediate content show a slight dependence. This shows that the paramagnetic impurities do have

strong effects on the NMR spin lattice relaxation times affecting the appearance of the peaks as a function of relaxation delay in the MAS spectra (Fig. 4.7 - 4.8). Similar information is obtained from the CPMAS spectra (Fig. 4.9 - 4.10). It may be suggest that in Nar, the presence of higher concentration of paramagnetic impurities, when compared to the other samples, induces a shortening of the T1 $\rho$  relaxation process, limiting the polarization transfer to C nuclei. This can explain to loss of cross-polarizable carbon signal in Nar sample collected at 10 ms contact time (Fig. 4.10).

	Geol1	Geol2	Hy1	Hy2	Hy3	Nar
Zn (g/Kg)	511	539	550	543	540	515
Pb (mg/Kg)	110	<0.4	0.05	81	25	1800
Cd (mg/Kg)	974	116	<0.4	<0.4	<0.4	560
Fe (mg/Kg)	300	21	<6.2	<0.4	<0.4	1970
Mn (mg/Kg)	300	2.00	0.01	0.04	0.02	220
Cu (mg/Kg)	17	12	8.08	7.02	7.56	150
Ni (mg/Kg)	23	10	0.08	0.08	0.08	330
Co (mg/Kg)	0.02	0.02	0.02	0.02	0.01	26
Ba (mg/Kg)	26	29	1.01	1.02	1.03	22
Sr (mg/Kg)	1.07	0.06	0.01	0.01	0.01	9

**Table 4.4** Concentration of paramagnetic impurities in the geologic samples (Geol1 and Geol2), synthetic samples (Hy1, Hy2 and Hy3) and biomineral samples (Nar).

2. The appearances of extra peaks in the range of 150-180 ppm could be explain by the presence of carbonyl/amide-carbons from organic biopolymers, as previously observed (Takahashi et al., 2004). However the presence of additional signals can be clearly excluded for the synthetic samples, since they were synthesized in our laboratory in the absence of any organic molecule, as evidenced by the absence of organic filaments in TEM images. As to the Geol1 and Geol2 samples, they show lower additional signals than the other samples analyzed, and, like the previous sample, the SEM images do not show traces of organic filaments. This evidence, and the fact that the amount of carbon estimates through CHNS-O analysis was in agreement with the stoichiometry of the hydrozincite formula (4.44%) for all geological and synthetic samples (Geol1 4.41%; Geol2 4.37%; Hy1 4.29%; Hy2 4.34%; Hy3 4.32%) rule out this possibility. Different consideration should be made regarding the Nar sample. In this sample, the C estimate through CHNS-O analysis revealed an excess of C (4.84%), which suggest the presence of biopolymer C. This evidence confirms the presence of some organic material in the Nar sample, as observed in SEM images (Fig. 4.3 g), and it is in good agreement with the signals observed in CPMAS spectrum, as shown in the next paragraph. In fact, the CPMAS spectrum Figure 4.12 of the Nar sample is characterized by a broad signals that can be attributed, as revealed by CHN-O analysis, to aliphatic chains (~22ppm) and to O-aliphatic –carbons (~73ppm and ~110 ppm), whereas these signals were not observed in the other samples. Carbonyl-C atoms would be expected in the range 160<d<190

ppm. All this evidence would suggest the presence of signals coming from carbonyl C from organic material in the range of 150-180 or at least, and more importantly, that the organic material has some influence in the formation of this additional signals.

3. The NMR technique is well known to be sensitive to the crystal order and to the presence of lattice defects such as stacking faults. The relation between stacking and/or polytype and NMR peak formation is well known in literature for several phase such as silicon carbide (Tateyama et al., 1997; Harris, 2004; Hartman et al., 1987), calcium silicate hydrate (Cong and Kirkpatrick, 1996) and saponite (Vogels, 2005). Depending on mineral synthesis, different stacking sequences or polytypes can possibly be achieved, (Vogels et al., 2005), and these result in different energy minima (Ryjáček et al., 2005) Despite the fact that the C has only one crystallographic position in the ideal structure of hydrozincite,  $^{13}\text{C}$  NMR spectra of our samples show up to five peaks depending on the mineral formation. These additional peaks can be ascribed to the presence of lattice defects, namely grain boundaries and stacking modes, that lower the crystal structure symmetry present in these hydrozincite crystals, in agreement with HRTEM analysis.

#### 4.5.5 Evidence of organic matrix in hydrozincite biomineral

This approach cannot be used for the Nar sample, in fact as observe in the whole spectrum collected with 1 ms to contact time (Fig. 3.12), this shows additional broad signal at ~22, ~73, ~103, ~173, ~181 ppm which were not present in all the spectra of the other samples.

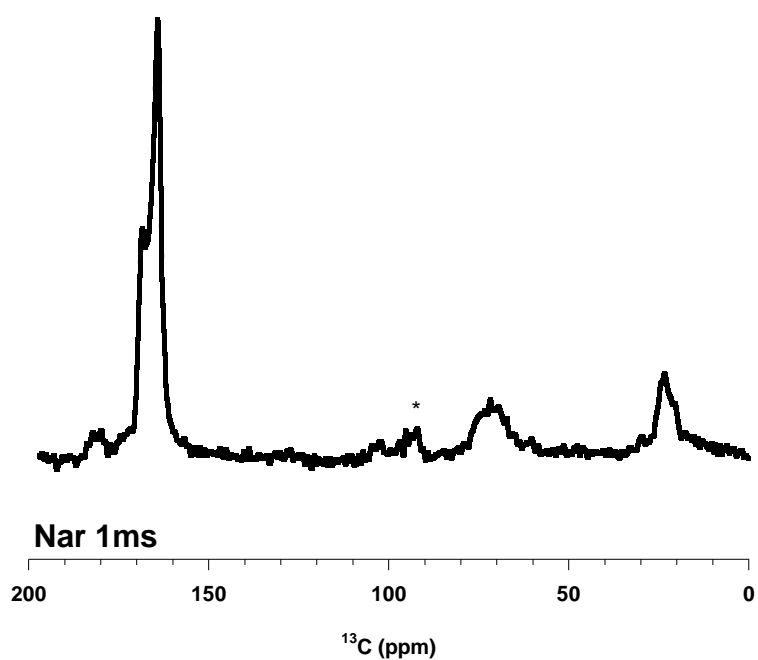


**Figure 4.12** The whole <sup>13</sup>C CPMAS spectrum of biomineral sample collected at 1 ms contact time. (\* indicates spinning side bands of the overlapping signals in the 163-169 ppm range).

These additional signals may be attributed to the presence of organic material. The hypothesis has been confirmed in addition to the SEM image (Fig. 4.3 g) also through the CHNS-O analysis, that revealed an excess of C (4.84%), for Nar sample respect the other samples (~ 4.2%), which suggest the presence of biopolymer C. The  $^{13}\text{C}$  CPMAS signals can be attributed, as revealed by CHN-O analysis, to aliphatic chains (~22ppm) and to O-aliphatic –carbons (~73ppm and ~110 ppm). In literature, Takahashi et al. (2004) show similar results for the biopolymer present in biomineral  $\text{CaCO}_3$  *Pinctada fucata*.

#### **4.6 FT-IR characterization of organic matrix**

The mineral phase of biomineral is intimately associated with a biological material, or matrix, that binds the crystals together from their early stages of assembly. The literature show that the biological component represents less than 5% of the entire biomineral volume (Marxen et al., 1998; Marin and Luquet, 2004; Dauphin, 2006); and, it is an integral part of the mineral and is responsible for crystal nucleation, growth and physical properties. (Lowenstam, 1981; Weiner, 1981). Therefore, knowing how this is achieved is extremely important to understand the whole mineralization process.

The matrix has been frequently investigated. Two fractions are present, one is the (water)-soluble fraction, and the other is the insoluble component.

It is essentially inter-crystalline, and acts as the framework upon which crystals are deposited. Therefore, the dissolution of the crystalline matter of the biomineral allows not only a clear three dimensional view of the insoluble matrix, but also a means of its biochemical characterization (Tong et al., 2002; Dauphin et al., 2003 a,b). The matrix basically contains proteins, carbohydrates, polysaccharides and

lipids (Levi-Kalisman et al., 2001). The soluble fraction is essentially associated with the surface of the insoluble and structured matrix, and also found within the crystals (Tong et al., 2002).

The mineral deposition dynamics and the biological and chemical reactions underlying it have not been completely explained. Recent studies by Cartwright and Checa (2007) emphasize the complexity of the phenomena involved, of biological and physical–chemical nature. The matrix is present between each crystalline layer and also within the crystals, comprised of crystalline subunits (Gregoire, 1961; Checa and Rodriguez-Navarro, 2001; Tong et al., 2002; Cartwright and Checa, 2007).

The third component of the organic matrix of calcareous biominerals is lipids. Although analyses dealing with this component, for example in biomineral as molluscan shells are scarce. Gouletquer and Wolowicz (1989) have estimated that proteins represent 90% of the organic matrix of the shell, carbohydrates vary from 0.15 to 0.29%, while lipids vary from 0.8 to 2.9%. Fatty acids, cholesterol, phytadienes and ketones have been described in modern and fossil shells (Cobabe and Pratt, 1995). Recently, Farre and Dauphin (2009) verified through spectrometry and thin layer chromatography the difference in lipids content between prismatic and nacreous layers of *P. nobilis* (Mytiloidea) and *P. margaritifera* (Pterioida, Pteriidae); both organisms contain lipids, but there are compositional differences.

FT-IR has also been applied for comparing the organic composition of different biominerals as molluscan shells (Dauphin, 1999; Dauphin et al., 2008). The biogenic crystal growth is controlled by an organic matrix responsible for defining: (a) crystal nucleation; (b) crystal size; (c) crystal orientation; (d) crystal morphological characteristics (Wilbur and Saleuddin, 1983). The use of infrared spectroscopy has identified the functional groups responsible for organic matrix.



The organic matrix, clearly visible in the  $^{13}\text{C}$  CPMAS NMR (Fig. 4.12) and SEM (Fig. 4.3 g) images for the Nar sample, has been extract and characterized by FT-IR. In the Figure 4.18 the FT-IR spectra for the Nar biomineral sample, the insoluble organic matrix (IOM) and lipidic fraction are reported.

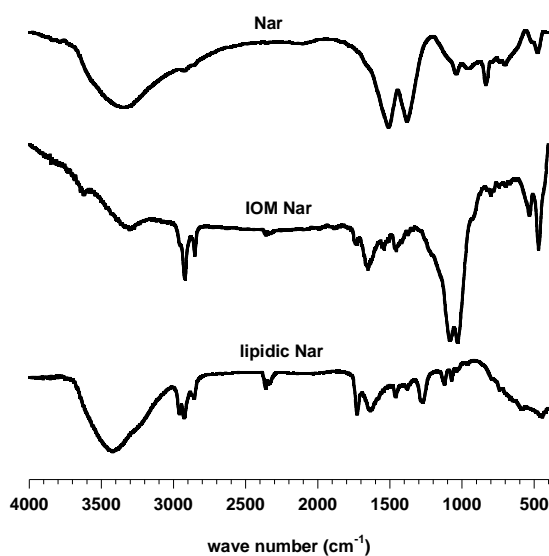


**Figure 4.18** FT-IR spectra of biomineral Nar sample, insoluble organic matrix (IOM) and lipidic extraction.

#### 4.6.1 Characterization of insoluble extract

For the better analysis of IOM the FT-IR spectrum has been divided in three range, the Figure 4.19 show the FT-IR between 4000-2700 cm<sup>-1</sup>, this part is characterized by bands corresponding to the N-H stretching at 3620 cm<sup>-1</sup>, amide A at 3300 cm<sup>-1</sup>, three signals at 2954, 2925 and 2854 cm<sup>-1</sup> corresponding to CH<sub>2</sub> and CH<sub>3</sub> vibrations.

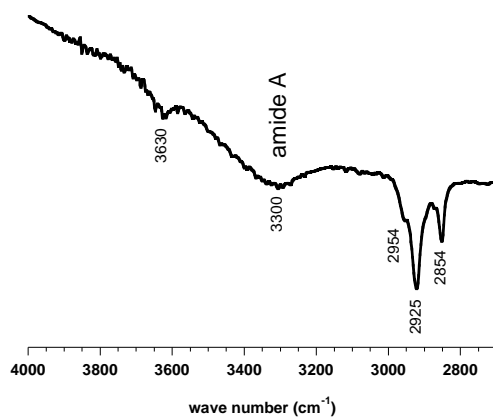


**Figure 4.19** Detailed FT-IR spectrum of IOM Nar sample in the range 4000-2700  $\text{cm}^{-1}$ .

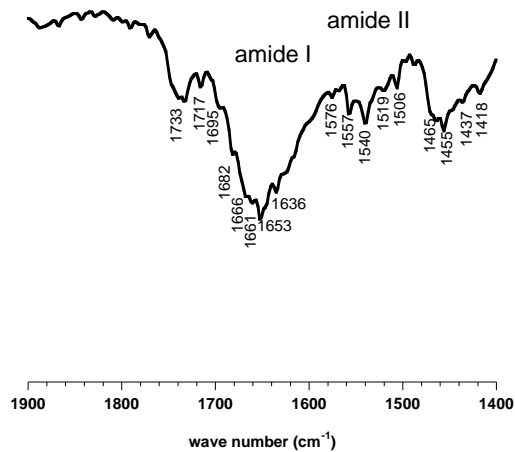


**Figure 4.20** Detailed FT-IR spectrum of IOM Nar sample in the range 1900-1400  $\text{cm}^{-1}$ .

In the range between 1900-1400  $\text{cm}^{-1}$  (Fig. 4.20) are very clearly the vibration of amide I and amide II: amide I at 1653  $\text{cm}^{-1}$  ( $\nu$  C=O), band of amide II at 1557  $\text{cm}^{-1}$  ( $\nu$  C-N and  $\delta$  N-H) and 1548  $\text{cm}^{-1}$  ( $\nu$  C=O). This part of the spectrum is very similar with other FT-IR spectrum of IOM for *Pinna Nobilis* and *Pinctada Margaritifera* calcitric prisms bivalves (Dauphin, 2003).

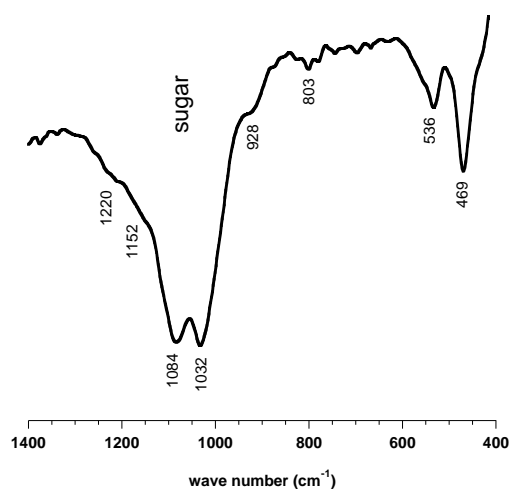


**Figure 4.21** Detailed FT-IR spectrum of IOM Nar sample in the range 1400- 400  $\text{cm}^{-1}$ .

FT-IR between 1400-400  $\text{cm}^{-1}$  is reported in the Figure 4.21. Band between 1000 and 1150  $\text{cm}^{-1}$  are usually considered to characterize the presence of polysaccharides. The FT-IR showed two important bands in this region at 1084 and 1032  $\text{cm}^{-1}$  which suggest the presence of polysaccharides in the insoluble matrix extracted from Nar sample.

## 4.6.2 Characterization of lipidic extract

FT-IR data on lipidic extracted from biomineral are very rare. Nevertheless, Samata and Ogura (1997) have shown that lipids were present in the nacreous layer of *Pinctada fucata*. The FT-IR of lipid extract from Nar sample is reported in the Figure 4.22. The spectrum shown characteristic frequencies for the lipids: a strong broad band centered at  $3422\text{ cm}^{-1}$  due to HOH stretching; IR absorption bands of

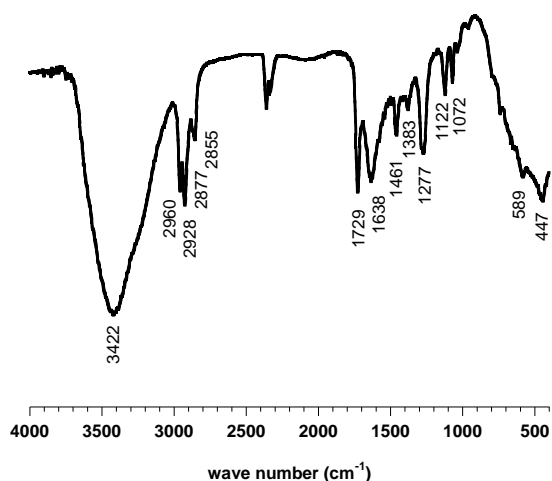


**Figure 4.22** FT-IR spectrum of lipidic extract from biomineral Nar.

aliphatic CH moieties at 2960, 2928, 2877 and  $2855\text{ cm}^{-1}$ , the bands around  $2960\text{ cm}^{-1}$  and  $2928\text{ cm}^{-1}$  are derived from asymmetric stretching of end-methyl aliphatic  $\text{CH}_3$  and methylene-chain  $\text{CH}_2$ , respectively (Bellamy, 1954), while the weaker bands from symmetric stretching of aliphatic  $\text{CH}_3$  and  $\text{CH}_2$  are also seen around

2877  $\text{cm}^{-1}$  and 2855  $\text{cm}^{-1}$ , respectively; intense signals at 1729  $\text{cm}^{-1}$  due to carboxylic acid ( $\nu\text{C}=\text{O}$ ); a weaker band for amide I at 1630  $\text{cm}^{-1}$ ;  $\text{CH}_2$  bending and  $\text{CH}_3$  symmetric bending at 1461  $\text{cm}^{-1}$  and 1383  $\text{cm}^{-1}$ , respectively; is also clearly the presence of phosphate diester, in fact the FT-IR showed the asymmetric stretching at 1277  $\text{cm}^{-1}$ , and the symmetric stretching at 1072  $\text{cm}^{-1}$  due to this group.

## 4.6 Conclusions

The microscopic properties of biomineral hydrozincite from Naracauli Creek (SW Sardinia) were investigated by using X-ray Diffraction (XRD), Fourier Transform Infrared (FT-IR), Nuclear Magnetic Resonance (NMR), Scanning Electron Microscopy (SEM), and High-Resolution Transmission Electron Microscopy (HRTEM). Because the biomineral hydrozincite turned out to significantly deviate from ideal structure of hydrozincite, synthetic and geologic samples were also investigated for comparison. SEM imaging shows that biomineral hydrozincite is made of small platelet-shaped crystallites having a 20-50 nm long side at the shortest and other sides measuring hundreds of nanometers long. These are interlaced to form sheaths several micrometers long. HRTEM analysis of the biomineral samples shows an imperfectly oriented aggregation of the nanocrystals that is discussed in terms of mesocrystals. TEM and XRD analysis indicate a progressive decrease in size of the particles in the biomineral compared to the synthetic and geologic hydrozincite samples, with coherent diffraction domains in the biomineral hydrozincite that are smaller by 30-50% that in the other samples investigated.  $^{13}\text{C}$  magic angle spinning (MAS) and cross-polarization magic angle spinning (CPMAS) NMR spectra show more than one peak for all the investigated samples, despite the fact that carbon atoms have a unique crystallographic

position in the hydrozincite structure. The additional peaks can reflect the presence of lattice defects, such as grain boundaries and stacking modes, can be observed both in the biomineral and in the synthetic samples. Further additional peaks in the NMR spectra of biomineral samples are attributed to organic molecules, relicts of the biomineralization process, in agreement with the filaments observed in SEM images of biomineral samples. The organic components of the biomineral sample has been extracted and characterized by FT-IR, it is composed by proteins, polysaccharides and lipids, and the result is very similar with other biomineral formation reported in literature

## 4.7 References

- Alam, T. M., Pless, J. D., Nenoff, T. M. Probing Water Dynamics in Octahedral Molecular Sieves: High Speed  $^1\text{H}$  MAS NMR Investigations. *Mag. Res. Mat. Sci.* (2007).
- Arrondo, J.L.R., and Goñi, F.M. Infrared studies of protein-induced perturbation of lipids in lipoproteins and membranes. *Chem. Phys. Lipids* 96, 53–68 (1998).
- Baccile, N., Laurent, G., Bonhomme, C., Innocenzi, P., Babonneau F. Solid-State NMR Characterization of the Surfactant-Silica Interface in Templated Silicas: Acidic versus Basic Conditions. *Chem. Mater.*, 19, 1343-1354 (2007).
- Banfield, J.F., Welch, S.A., Zhang, H.Z., Ebert, T.T., and Penn, R.L. Aggregation-based crystal growth and microstructure development in natural iron oxyhydroxide biomineralization products. *Science*, 289, 751-754 (2000).
- Beedham, G.E., 1958. Observations on the non-calcareous component of the shell of the Lamellibranchia. *Q. J. Microsc. Sci.* 99, 341–357 (1958).
- Bellamy, L.J. (Ed.). *The Infra-red Spectra of Complex Molecules*. John Wiley & Sons, New York, pp. 13–56 (1954).
- Berman, A., Hanson, J., Leiserowitz, L., Koetzle, T.F., Weiner, S., Addadi, L., 1993. Crystal–protein interactions: controlled anisotropic changes in crystal microtexture. *J. Phys. Chem.* 97, 5162–5170 (1993).
- Brunner, E., and Sternberg, U. Solid-state NMR investigations on the nature of hydrogen bonds. *Prog. Nucl. Magn. Reson. Spectrosc.* 32, 21–57 (1998).
- Cartwright, J.H.E., and Checa, A.G. The dynamics of nacre self-assembly. *J. R. Soc. Interface*, 4, 491–504 (2007).
- Checa, A.G., and Rodriguez-Navarro, A. Geometrical and crystallographic constraints determine the self-organization of shell microstructures in Unionidae (Bivalvia: Mollusca). *Proc. R. Soc. Lond. B* 268, 771–778 (2001).

- Cobabe, E.A., and Pratt, L.M. Molecular and isotopic compositions of lipids in bivalve shells: a new prospect for molecular paleontology. *Geochim. Cosmochim. Acta*, 59, 87–95c (1995).
- Collins, M.J., Stern, B., Abbott, G.D., Walton, D., Riley, M.S., vonWallmenich, T., Savage, N.M., Armstrong, H.A., Westbroek, P. “Intracrystalline” organic matter in biominerals. In: Grimalt, J.O., Dorronsoro, C. (Eds.), *Organic Geochemistry: Developments and Applications to Energy, Climate, Environment and Human History*. AIGOA, Donostia- San Sebastian, Spain, 702–705 (1995).
- Cuif, J.P., Dauphin, Y., Denis, A., Gaspard, D., Keller, J.P. Continuité et périodicité du réseau organique intraprismatique dans le test de *Pinna muricata* Linné (Lamellibranches). *C.R. Acad. Sci. Paris*, 290, sér. D 759–762 (1980).
- Cong, X. and Kirkpatrick, R.J.  $^{17}\text{O}$  NMR investigation of the structure of calcium silicate hydrate gel. *Journal of American Chemical Society*, 79, 1585-1592 (1996).
- Dauphin, Y. Structure and composition of the septal nacreous layer of *Nautilus macromphalus* L. (Mollusca, Cephalopoda). *Zoology* 109, 85–95 (2006).
- Dauphin, Y., Cuif, J.P., Doucet, J., Salomé, M., Susini, J., Williams, C.T. In situ chemical speciation of sulfur in calcitic biominerals and the simple prism concept. *J. Struct. Biol.*, 142, 272–280 (2003).
- Dauphin, Y., Ball, A.D., Cotte, M., Cuif, J.-P., Meibom, A., Salomé, M., Susini, J., Williams, C.T. Structure and composition of the nacre-prisms transition in the shell of *Pinctada margaritifera* (Mollusca, Bivalvia). *Ann. Bioanal. Chem.* 390, 1659–1669 (2008).
- Dauphin, Y. Soluble organic matrices of the calcite prismatic shell layers of two Pteriomorphid bivalves. *J. Biol. Chem.* 17, 15168-15177 (2003).
- Gre´goire, Ch. Structure of the conchiolin cases of the prism in the *Mytilus Edulis* Linne. *J. Biophys. Biochem. Cytol.* 9 (2), 395–400 (1961).



- Gouletquer, P., and Wolowicz, M. The shell of *Cardium edule*, *Cardium glaucum* and *Ruditapes philippinarium*: organic content, composition and energy value, as determined by different methods. *J. Mar. Biol. Assoc. U.K.* 69, 563–572 (1989).
- Grégoire, C., Duchateau, G., Florin, M., 1955. La trame protidique des nacres et des perles. *Ann. Inst. Océanogr.* 31, 1–36 (1955).
- Ghose, S. the crystal structure of hydrozincite,  $Zn_5(OH)_6(CO_3)_2$ . *Acta Crystallographica*, 17, 1051-1057 (1964).
- Gyunggoo C., Yaotang Wu., Jerome L. Detection of Hydroxyl Ions in Bone Mineral by Solid-State NMR Spectroscopy. *Science*, 300, 1123 (2003).
- Engelhardt, G. High Resolution Solid State NMR of Silicates and Zeolites, 485 p. Wiley, New York, (1987).
- Eckert, H., Yesinowski, J.P., Stolper, E.M., Stanton, T.R., Holloway, J. The state of water in rhyolitic glasses a deuterium NMR study. *J. Non-Cryst Solids*, 93,93–114(1987).
- Jones, G.C., and Jackson, B. Infrared Transmission Spectra of Carbonate Minerals. Chapman and Hall, London. 256 pp (1993).
- Kobayashi, I., and Samata, T. Bivalve shell structure and organic matrix. *Mat. Sci. Engineer, r C26*, 692–698 (2006).
- Kohn, S.C. Structural Studies of OH in Nominally Anhydrous Minerals Using NMR. *Min.Soc.America*, (2007).
- Lowenstam H. A. Minerals formed by organisms. *Science*, 211, 1126-1131 (1981).
- Hatchett, C. Experiments and observations on shell and bone. *The Royal Soc.* 89, 315–334 (1799).
- Hales, M.C. and Frost, R.L. Synthesis and vibrational spectroscopy characterization of synthetic smithsonite and hydrozincite. *Polyhedron*, 26, 4955-4962 (2007).

- Harris, R.K. NMR crystallography: The use of chemical shift. *Solid State. Science*, 6, 1025-1037 (2004).
- Hartman, J.S., Richardson, M.F., Sherriff, B.L., and Winsborrow, B.G. Magic angle spinning NMR studies of silicon carbide: polytypes, impurities, and highly inefficient spin-lattice relaxation. *J. Am. Chem. Soc.* 109, 6059-6067 (1987).
- Holland, G. P., Cherry, B. R., Alam, T. M. Distribution effects on  $^1\text{H}$  double-quantum MAS NMR spectra. *J. Mag. Res.*, 161-167 (2004).
- La Mar, G.N., Horrocks Jr., W.D., and Holm, R.H. NMR of Paramagnetic Molecules, 678 p. Academic Press, New York, (1973).
- Libowitzky, E. correlation of O-H stretching frequencies and O-H...O hydrogen bond lengths in minerals. *Monatshefte fur Chemie*, 130, 1047-1059 (1999).
- Mehring, M. Principles of High Resolution NMR in Solid, 2<sup>nd</sup> edition, 342 p. Springer-Verlag, New York, (1983).
- Meldrum, F. and Cölfen, H. Controlling mineral morphologies and structures in biological and synthetic systems. *Chem. Rev.* 108, 4332-4432 (2007).
- Music, S.; Popovic, S.; Maljkovic, M.; Dragc̃evic, D. Influence of synthesis procedure on the formation and properties of zinc oxide. *J. Alloys Compd.*, 347, 324-332 (2002).
- Mutvei, H. On the micro- and ultrastructure of the conchiolin in the nacreous layer of some recent and fossil molluscs. *Stockh. Contrib. Geol.* 20, 1-17 (1969).
- Marxen, J.C., and Becker, W. The organic shell matrix of the freshwater snail *Biomphalaria glabrata*. *Comp. Biochem. Physiol.* 118 B, 23-33 (1997).
- Marin, F., and Luquet, G. Molluscan shell proteins. *Comptes Rendus Palevol*, 3, 469-492 (2004).
- Mykhaylyk, O.O., Khimyak, Y.Z., Attfiel, J.P., Mykola, P., Gadzira, M.P. Phase segregation in silicon carbide-carbon solid solutions from XRD and NMR studies. *Chem. Mater.*, 14, 1348-1353 (2002).

- Nara, M., Okazaki, M., Kagi, H. Infrared study of human serum very-low-density and low-density lipoproteins. Implications of esterified lipid C=O stretching bands for characterizing lipoproteins. *Chem. Phys. Lipids*, 117, 1–6 (2002).
- Nenoff, T. M., Ockwig, N. W., Cygan, R. T., Alam, T. M., Leung, K., Pless, J. D., Xu, H., Hartl, M. A., Daemen, L.L. Role of Water in the Ion Selectivity of Niobate-Based Octahedral Molecular Sieves. *J. Phys. Chem. C*, 111, 13212-13221 (2007).
- Papenguth, H. et al. <sup>13</sup>C MAS NMR spectroscopy of inorganic and biogenic carbonate. *Am. Miner.*, 74, 1152-1158 (1989).
- Patterson, A. The Scherrer Formula for X-Ray Particle Size Determination. *Phys. Rev.*, 56 (10), 978–982 (1939).
- Pohle, W., Gauger, D.R., Fritzsche, H., Rattay, B., Selle, C., Binder, H., Böhlig, H. FTIR—spectroscopic characterization of phosphocholine-headgroup model compounds. *J. Mol. Struct.*, 563/564, 463–467 (2001).
- Rousseau, M., Bedouet, L., Latie, E., Gasser, P., Le Ny, K., Lopez, E. Restoration of stratum corneum with nacre lipids. *Comp. Biochem. Physiol. B*, 145, 1–9 (2006).
- Rothwell W. P., Waugh J. S., Yesinowski J. P. High-resolution variable-temperature phosphorus-31 NMR of solid calcium phosphates *J. Am. Chem. Soc.*, 102, 2637 (1980).
- Ryjáček, F., Engkvist, O., Vacek, J., Kratochvíl, M., and Hobza, P. Hoogsteen and stacked structures of the 9-methyladenine 1-methylthymine pair are populated equally at experimental conditions: Ab initio and molecular dynamics study. *J. Phys. Chem. A*, 105, 1197-1202 (2001).
- Samata, T., Ogura, M. First finding of lipid component in the nacreous layer of *Pinctada fucata*. *J. Fossil Res.* 30, 66 (1997).
- Simkiss, K. The organic matrix of the oyster shell. *Comp. Biochem. Physiol.*, 16, 427–435 (1965).

- Scherrer P., Nachrichten von der Gesellschaft der Wissenschaften zu Göttingen, 98-100 (1918).
- Schmidt, M., and Lutz, H.D. Hydrogen bonding in basic copper salts: a spectroscopic study of malachite,  $\text{Cu}_2(\text{OH})_2\text{CO}_3$ , and brochantite,  $\text{Cu}_4(\text{OH})_6\text{SO}_4$ . *Phys. Chem. of Min.*, 20 (1), 27-32 (1993).
- Takahashi, K., Yamamoto, H., Onoda, A., Doi, M., Inaba, T., Chiba, m., Kobayashi, A., Taguchi, T., Okamura, T.-a., and Ueyama, N. Highly oriented aragonite nanocrystal-biopolymer composites in an aragonite brick of the nacreous layer of *Pinctada fucata*. *Chem. Comm.*, 8, 996-997 (2004).
- Tateyama, H., Noma, H., Adachi, Y., and Komatsu, M. Prediction of stacking faults in  $\beta$ -silicon carbide: X-ray and NMR studies. *Chem. Mater.*, 9, 766-772 (1997).
- Tong, H., Hu, J., Ma, W., Zhong, G., Yao, S., Cao, N. In situ analysis of the organic framework in the prismatic layer of mollusk shell. *Biomaterials*, 23, 2593–2598 (2002).
- Ueyama, N., Hosoi, T., Yamada, Y., Doi, M., Okamura, T., Nakamura, A. Calcium complexes of carboxylate-containing polyamide with sterically disposed NH-O hydrogen bond: Detection of the polyamide in calcim carbonate by  $^{13}\text{C}$  cross polarization/magic angle spinning spectra. *Macromolecules*, 31, 7119-7126 (1998).
- Vogels, R.J.M.J., Kloprogge, J.T., Geus, J.W. Synthesis and characterization of boron and gallium substituted saponite clays below 100°C at one atmosphere. *Microporous and Mesoporous Material*, 77, 159-165 (2005).
- Yesinowski J. P., Eckert H. Hydrogen environments in calcium phosphates: proton MAS NMR at high spinning speeds. *J. Am. Chem. Soc.*, 109, 6274 (1987).
- Weiner S., Traub W. and Lowenstam H. A. Organic matrix in calcified exoskeletons. In *Biomineralization and Biological Metal Accumulation* (Edited by Westbroek P. and DeJong E. W.), pp. 205-224. D. Reidel, Holland (1983).

Wu Y., Ackerman J. L., Kim H. M., Rey C., Barroug A., and Glimcher M. J. Nuclear Magnetic Resonance Spin-Spin Relaxation of the Crystals of Bone, Dental Enamel, and Synthetic Hydroxyapatites. *J. Bone Miner. Res.*, 17, 472 (2002).

Zabinski, W. The problem of stacking-order in natural hydrozincite. *Can. Mineral.* 8, 649 (1964).



## Chapter V Characterization of the interaction hydrozincite/DEHP

---

### 5.1 Hydrozincite in vitro synthesis

Another important aspect of the research was to understand the phenomenon, at the molecular level, of the hydrozincite biomineralization.

But during the attempt to reproduce the hydrozincite biomineral in vitro, we have found the presence of new molecule bounding with the mineral. The Figure 5.1 showed the FT-IR spectra of synthetics hydrozincite Hy3 and Hy4.

Both FT-IR spectra in the range of 400 – 1800  $\text{cm}^{-1}$ , are the carbonate stretching and bending modes of hydrozincite (see chapter IV), in agreement with those reported in literature (Music et al., 2002): the four peaks in the region of 1520–1390  $\text{cm}^{-1}$  ascribed to the asymmetric C-O stretching  $\nu_3$  mode (the correlation field splitting is well observed in the spectrum); the strong and sharp peak at 836  $\text{cm}^{-1}$  assigned to the  $\nu_2$  out-of-plane O-C-O bending mode and the one at 709  $\text{cm}^{-1}$  is assigned to  $\nu_4$  asymmetric O-C-O bending modes and the peak at 1047  $\text{cm}^{-1}$  assigned to the  $\nu_1$  symmetric C-O stretching mode (Music et al., 2002). The spectrum exhibits broad signals which were attributed to the contributions of different lattice defects and grain boundaries (Hales and Frost, 2007). But in the 15% of synthesized hydrozincite samples, the FT-IR spectrum, besides the signals ascribed to hydrozincite, shows several new peaks (Hy4): a series of signals in the region of the C-H stretching at 2962, 2925, 2875, 2858  $\text{cm}^{-1}$ ; an intense signal at 1730  $\text{cm}^{-1}$ , which is typical of ester C=O stretching; and two small bands at 1290  $\text{cm}^{-1}$  and 1189  $\text{cm}^{-1}$ . The new signals were partially removed after washing the sample with acetone at room temperature (Fig. 5.1, sample Hy4/1).

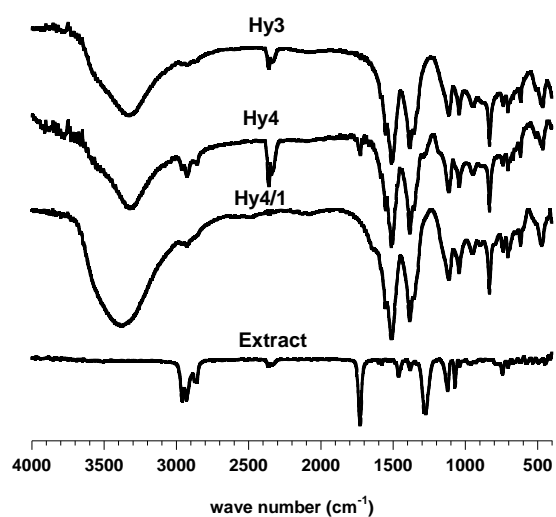


**Figure 5.1** FT-IR spectra of synthetic hydrozincite (Hy3), synthetic hydrozincite with unknown molecule (Hy4), Hy4 washed with acetone (Hy4/1) and the extract molecule.

The acetone extract was evaporated and the residue, which appeared as a viscous liquid, was characterized through FT-IR and NMR spectroscopy. The FT-IR spectrum of this sample (Fig. 5.1 extract) exhibits new signals which were not evident in the Hy4 spectrum, as they were hidden by the hydrozincite signals. These signals are present in the region of C-H bending at  $1467\text{ cm}^{-1}$ , and in the region of C-O stretching at  $1293$ ,  $1273$ ,  $1141$ ,  $1125$ ,  $1075\text{ cm}^{-1}$  respectively, and two signals at  $744$  and  $705\text{ cm}^{-1}$ .



## 5.2 Identification of extract molecule

This extract molecule has been identified by means 1D  $^1\text{H}$  and  $^{13}\text{C}$ , and 2D COSY, HSQC and HMBC NMR experiments. In Figure 5.2 and 5.3 the  $^1\text{H}$  NMR and  $^{13}\text{C}$  NMR experiment for the extract molecules in Acetone- $d_6$  are reported.

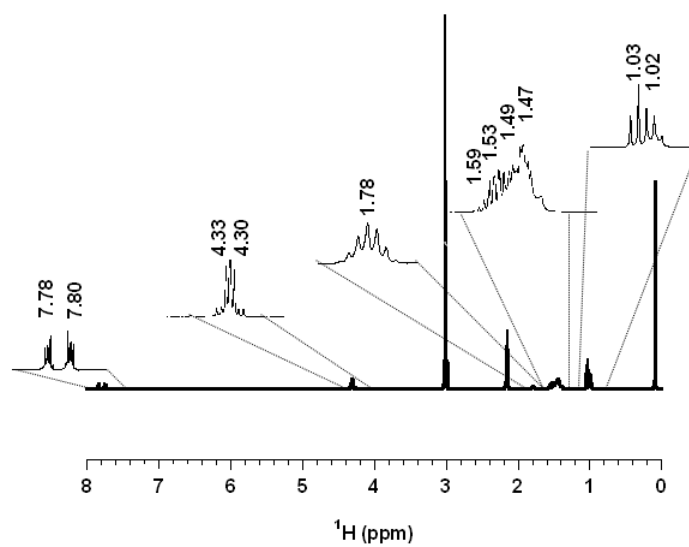


**Figure 5.2**  $^1\text{H}$  NMR spectrum for extract molecules by Hy4.

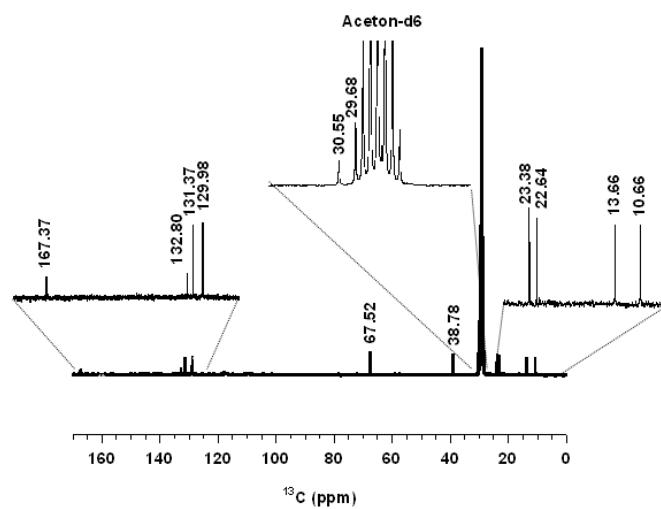


**Figure 5.3**  $^{13}\text{C}$  NMR spectrum for extract molecules by Hy4 sample.

In the  $^1\text{H}$  NMR (Fig. 5.2) spectrum the signals at 7.85 ppm and 7.78 ppm exhibiting the AA'BB' system typical of a di-substituted ring whereas the signals at 4.33 ppm is the AB part of the ABX pattern formed by three protons in the OCH<sub>2</sub>CH group. The  $^{13}\text{C}$  NMR (Fig. 5.3) spectrum of unknown compound showed 12 carbon signals.

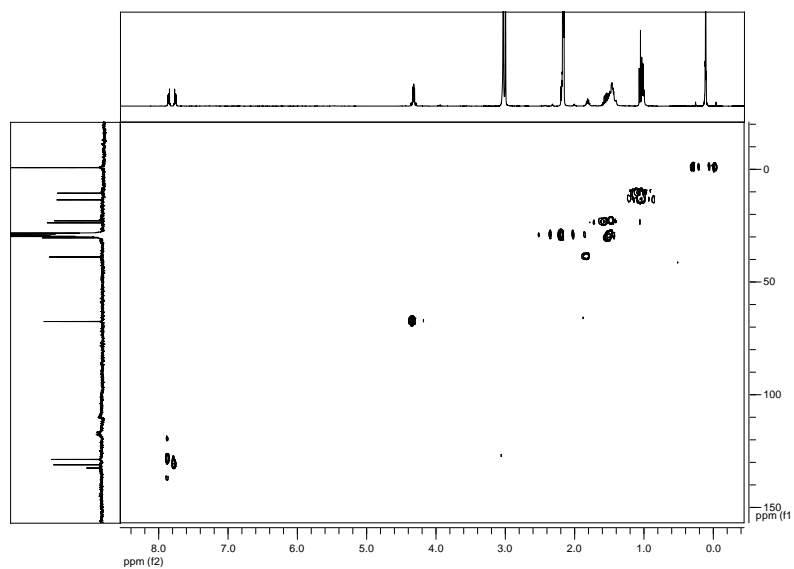


**Figure 5.4** COSY experiment acquired with 64 transients with a total 2 K data points along the t2 axis and 512 data points along the t1 axis.

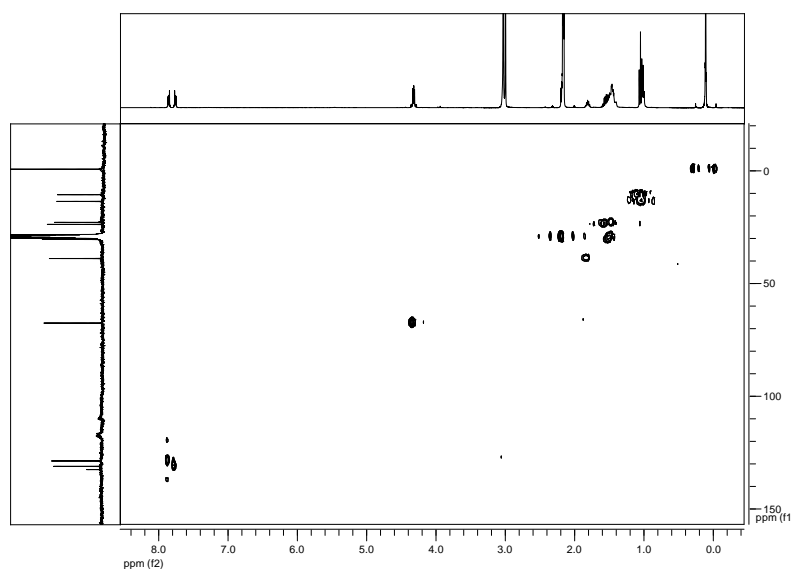


**Figure 5.5**  $^1\text{H}/^{13}\text{C}$  HSQC spectrum recorded with 64 transients with 2k points in the t2 dimension and 512 in the t1 dimension.

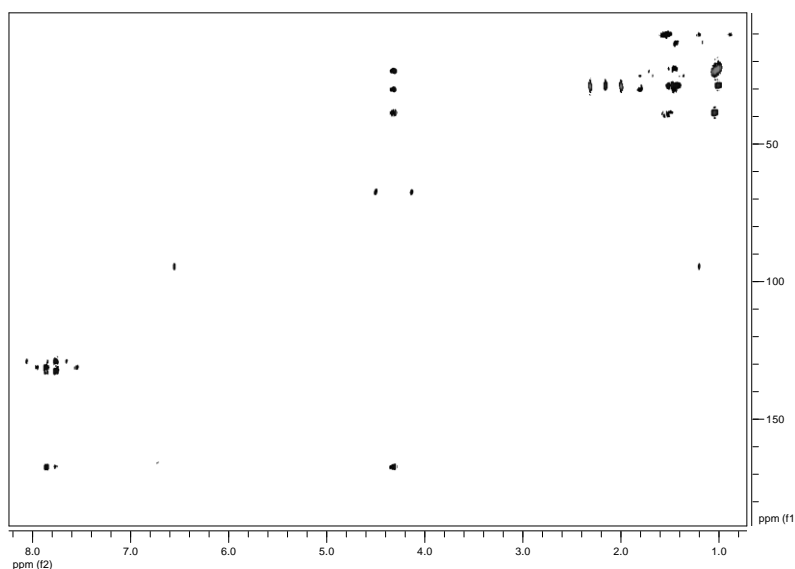


**Figure 5.6**  $^1\text{H}/^{13}\text{C}$  HMBC spectrum recorded with 128 transients with 2k points in the t2 dimension and 512 points in the t1 dimension

The COSY (Correlation Spectroscopy) experiment showed the cross peaks couplings (2 and 3 bond) between two protons, the spectrum in the figure 5.4 H-5 showed cross peaks with H-6 methine protons, H-9 correlated with H14 and H10. A HSQC (Heteronuclear Single Quantum Coherence) experiment was utilized to assign the protons to their attached carbons. In the spectrum reported in the figure 5.5, the carbons 4/5 and 3/6 showed cross peaks with two multiplets at 7.85 and 7.78 ppm; the C-9 showed the cross peak at 1.78 ppm, the C-10 at 1.59 ppm, the C11 and C12 respectively at 1.49 and 1.47 ppm, the C-14 at 1.53 ppm; C-11 and C-15 showed the cross peaks respectively at 1.02 and 1.05 ppm. HMBC (Heteronuclear Multiple Bond Coherence) was utilized for the determination of connectivity between two different nuclear species; in the Figure 5.6 the interactions where found between H-4,5 and C-1,2 and between H-13 and C-12,

C-11 and between H-15 and between C-14 . All these correlation suggested that the unknown molecule correspond to Bis(2-ethylexil)phthalate, an schematic representation of the molecules is reported in Figure 5.7

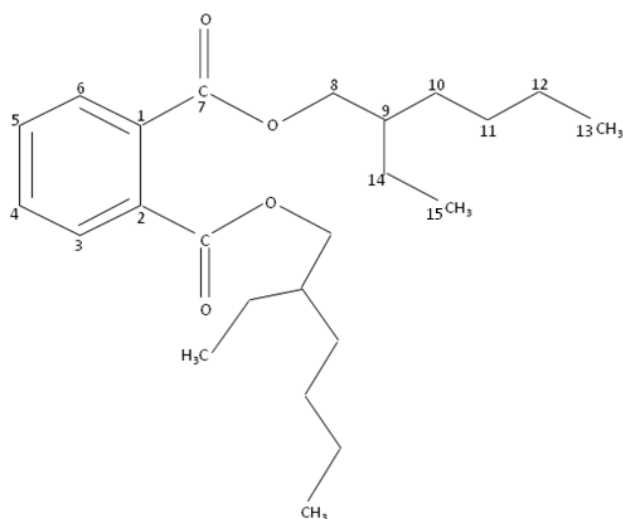


**Figure 5.7** The schematic representation of Bis(2-ethylexil)phthalate.

The complete assignment of the <sup>13</sup>C NMR and <sup>1</sup>H signals of neat DEHP, which result in good agreement with previous assignments (Cohen et al., 2001) is shown in Table 5.1.

DEHP	<sup>13</sup> C δ (ppm)	<sup>1</sup> H δ (ppm)
1/2	132.8	
4/5	128.98	7.85m
3/6	131.37	7.78m
7	167.37	
8	67.52	4.33dd 4.30dd
9	38.78	1.78sept
10	29.68	1.59quad
11	23.38	1.49quint
12	22.64	1.47sest
13	13.66	1.02t
14	30.55	1.53sest
15	10.66	1.03t

**Table 5.1** Complete assignment of <sup>1</sup>H and <sup>13</sup>C chemical shift for DEHP.

### 5.3 Origin of DEHP pollution

DEHP is commonly used as a plasticizer and is contained in the plastic materials used in the synthesis, for this reason we have analyzed the plastic devices (flexible tube and plastic container) used for the synthesis. In the Figure 5.8 the FT-IR analysis of plastic devices in comparison with extract molecule and pure DEHP are reported.

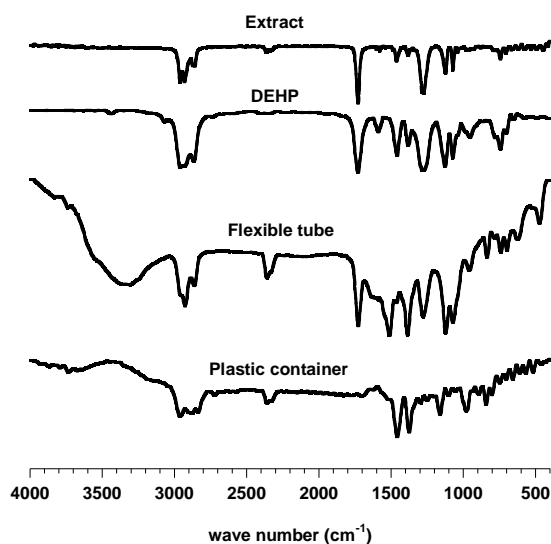


**Figure 5.8** FT-IR spectra of extract molecule by Hy4, pure DEHP and plastic device as flexible tube and plastic containers.

The signal characteristic for DEHP at  $1730\text{ cm}^{-1}$  which is attributing to the carboxylic group is present in the FT-IR spectrum of flexible tube.

These results would suggest that DEHP migrates from the PVC tube into the solution and is then taken up by hydrozincite during precipitation.

#### **5.4 FT-IR study of hydrozincite synthesized in presence of PVC**

In order to test the reproducibility of DEHP uptake, hydrozincite was synthesized in the presence of sliced flexible tubing sections (Hy5). As can be observed in the FT-IR spectrum of the sample Hy5 signals attributed to DEHP are clearly visible (Fig. 5.9); the spectrum of the Hy3 sample is shown for comparison. The

experiment was repeated several times always giving the same result when the pH of the solution was set at 6.8, which was found to be stable during the experiments.

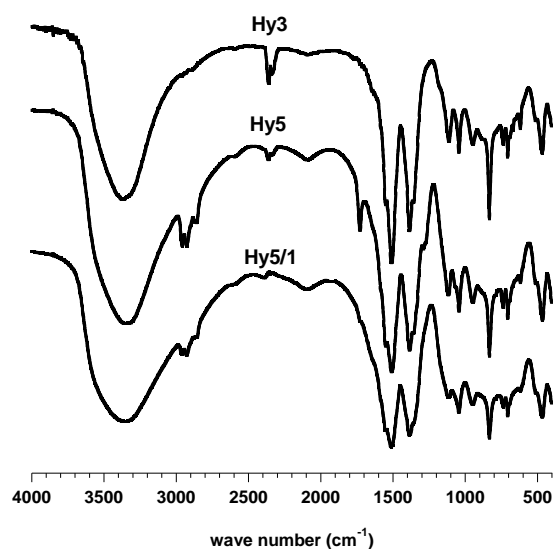


**Figure 5.9** FT-IR of synthetic hydrozincite Hy3, hydrozincite synthesized in presence of PVC slices (Hy5) and Hy5 after washing with acetone Hy5/1.

In order to evaluate whether the DEHP was only adsorbed by hydrozincite, the sample Hy5 was washed with acetone at room temperature in a glass tube. The FT-IR spectrum of the washed hydrozincite (Hy5/1) showed that the signal intensities pertaining to DEHP were significantly reduced. However, as can be observed from the signals attributed to C-H stretching vibration, some of the DEHP remained. The absence of the signal attributed to the C=O stretching vibration is evident.



For explain this different evolution of the DEHP signals in the FT-IR spectra after washing, we have prepared several samples of hydrozincite (Hy3) mixed with pure DEHP.

## 5.5 FT-IR study of hydrozincite/DEHP mixture

Several samples are prepared by mixing hydrozincite Hy3 with different quantities of pure commercial DEHP. The FT-IR spectra for the hydrozincite samples mixed with 25 $\mu$ l, 50  $\mu$ l, 100  $\mu$ l, 200  $\mu$ l, 400  $\mu$ l of pure DEHP are show in Figure 5.10.

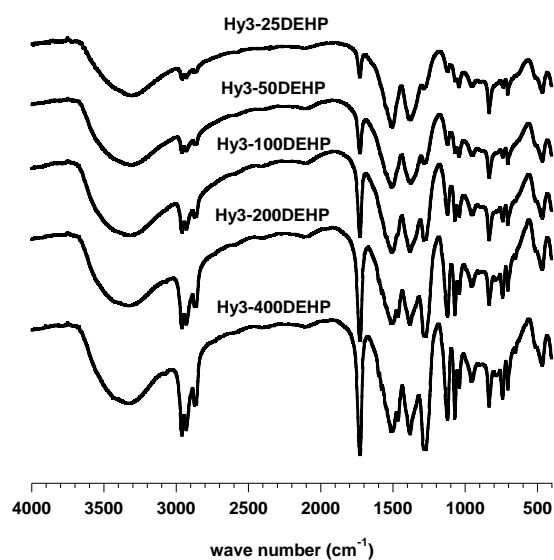


**Figure 5.10** FT-IR spectra 300 mg of hydrozincite Hy3 mixed with 25 $\mu$ l of pure DEHP (Hy3-25DEHP), with 50 $\mu$ l of pure DEHP (Hy3-50DEHP), with 100 $\mu$ l of pure DEHP (Hy3-100DEHP), with 200 $\mu$ l of pure DEHP (Hy3-200DEHP) and with 400 $\mu$ l of pure DEHP (Hy3-400DEHP).

The intensity of the signals in the region of C-H stretching ( $2800-3000\text{ cm}^{-1}$ ) and the signal of the C=O stretching at  $1730\text{ cm}^{-1}$  increase with addition of DEHP. The FT-IR spectra does not show any shift of the above mentioned signals, neither the signals attribute to hydrozincite show broadening or shift.

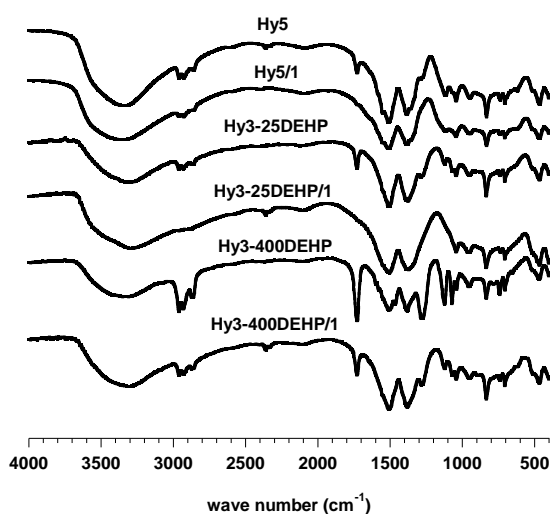


**Figure 5.11** FT-IR spectra of Hy5, Hy5 after washing (Hy5/1), Hy3-25DEHP, Hy3-25DEHP after washing (Hy3-25DEHP/1), Hy3-400DEHP and Hy3-400DEHP after washing (Hy3-400DEHP/1).

The Figure 5.11 display the FT-IR spectra of Hy5, Hy5/1, Hy3-25DEHP, Hy3-25DEHP/1, Hy3-400DEHP, Hy3-400DEHP/1. The samples Hy5/1, Hy3-25DEHP/1, Hy3-400DEHP/1 were the samples washed with acetone. After washing (Hy3-25DEHP/1 and Hy3-400DEHP/1) the FT-IR spectra showed that the intensity of the C-H stretching signals and C=O signals decrease proportionally, but for the sample Hy5 this proportionally is not respect, in fact after washing (Hy5/1) the FT-IR present the signals for the C-H but is not present the C=O stretching.

This result indicates that the C=O stretching signal of the DEHP is broadened beyond detection in the spectrum of Hy5/1, and this suggest that DEHP is strongly bound to the hydrozincite, possibly through the C=O groups, when flexible tubing is present during the hydrozincite synthesis (sample Hy5), while it shows a weaker interaction with the surface of the hydrozincite when added to hydrozincite nanocrystals (sample Hy3-400DEHP).

For comparison the synthetic calcite has been prepared in the presence of flexible tubing slices (Cal2). The FT-IR spectra are reported in Figure 5.12. The FT-IR spectra are consistent with the previously reported spectra of pure calcite (White, 1974; Balmain et al., 1999; Cebeci and Soñmez, 2004). Both spectra showed the diagnostic and characteristic signals for the calcite at 1428, 878, and 714  $\text{cm}^{-1}$  that correspond to the  $\nu_2$ ,  $\nu_3$  and  $\nu_4$  mode of vibration stretching. In the spectra are present also the bands for the overtone of calcium carbonate at 2983, 2782, 2589, 2511  $\text{cm}^{-1}$  and a broad band in the region of 3700-3100  $\text{cm}^{-1}$  attributable to the stretching modes of structural water.

The spectrum for the calcite synthesized in the presence of flexible tubing slices resulted indistinguishable from the calcite control spectra (Cal1). This result shows no evidence of DEHP incorporation into calcite during growth, under the experimental conditions used.

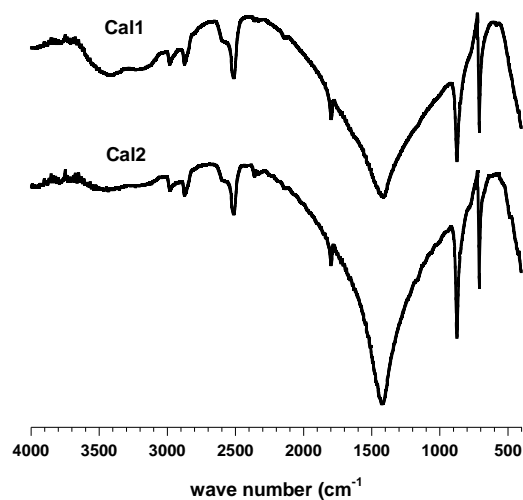
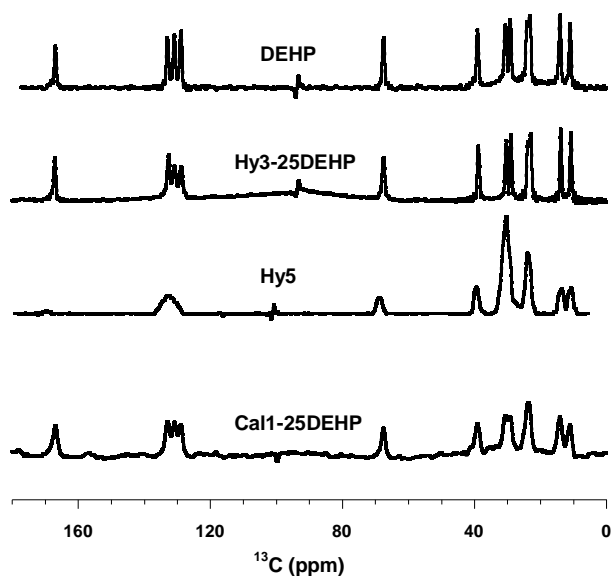


**Figure 5.12** FT-IR of synthetic calcite Cal1 and synthetic calcite synthesized in presence of PVC (Cal2).

## 5.6 $^{13}\text{C}$ MAS NMR investigation of hydrozincite/DEHP

NMR spectroscopy is well suited for the study of organic compound – solution or organic compound adsorbed interaction because it is an element specific method that is extremely sensitive to the electron density (shielding) near the nucleus of interest. NMR techniques can be used to obtain a variety of information about an adsorbed molecule, including mechanisms of adsorption and surface sites involved, the dynamics (molecular diffusion, chemical exchange) of an adsorbed molecule on a mineral surface (Fyfe, 1983). The  $^{13}\text{C}$  NMR spectra of pure DEHP (neat DEHP), hydrozincite in which 25  $\mu\text{l}$  of neat DEHP was added to 300 mg of

hydrozincite (Hy3-25DEHP) and hydrozincite synthesized in the presence of sliced flexible tubing sections (Hy5) are shown in Figure 5.13.

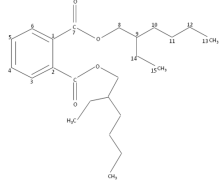


**Figure 5.13**  $^{13}\text{C}$  MAS spectra of the following samples: DEHP as a neat liquid (DEHP), hydrozincite mixed with DEHP (Hy3-25DEHP), DEHP adsorbed on hydrozincite by sliced pipes (Hy5), calcite mixed with DEHP (Cal1-100DEHP).

In the Hy3-25DEHP and Hy5 MAS spectra signal from the carbonate group of hydrozincite, which occurs between 160 – 170 ppm, is not visible. This absence of carbonate peaks is due to the short repetition time (1 s) used in the experiments relative to the long spin lattice relaxation time that characterizes the hydrozincite carbonate carbon (> 50 s). However, all the carbon signals pertaining to DEHP, which exhibit spin lattice relaxation times shorter than 1 s, are clearly visible.

The most important differences concerning the  $^{13}\text{C}$  NMR spectra of DEHP as a neat liquid and DEHP in the Hy5 and Hy3-25DEHP samples are highlighted in the following:

- $^{13}\text{C}$  spectrum of neat liquid DEHP taken without sample spinning (spinning at 1 kHz did not change the quality of the spectrum) is shown in Figure 5.13 and the chemical shift values are listed in Table 5.1. The Full Width at Half Maximum (FWHM) of the carbon signals of this sample range between 0.82 ppm (C3/6) to 0.72 ppm (C7).
- $^{13}\text{C}$  MAS peaks of the aliphatic chains of DEHP mixed with hydrozincite (Hy3-25DEHP) are very similar to those observed for neat liquid DEHP. Slight differences were observed in the regions for C8, carboxyl and ring carbons: the peaks for C8, carboxyl and ring carbons in the Hy3-25DEHP MAS spectra are slightly broader (FWHM >1.0 ppm) and the carboxyl signal is shifted 0.4 ppm downfield (Table 5.1).
- $^{13}\text{C}$  MAS spectrum of the Hy5 sample exhibits overlapping resonances and a downfield shift of the aliphatic carbons (Fig. 5.13 and Table 5.1). The ring carbons show only a single, unresolved broad peak (FWHM = 5.3 ppm) shifted downfield (~3 ppm) and the carboxyl peak is also broadened (FWHM > 3 ppm) and shifted downfield (3.5 ppm).

	Carbon type	<sup>13</sup> C (ppm)		
		DEHP	Hy3-25DEHP	Hy5 <sup>a</sup>
1/2	Ring carbon	132.8	132.6	132.6
3/6	Ring carbon	130.7	130.9	
4/5	Ring carbon	128.8	128.8	
7	Carbonyl group	166.7	167.2	169.5
8	Methylene group	67.4	67.4	67.7
9	Methyne group	38.8	38.8	39.4
10	Methylene group	28.9	28.9	30.4
11	Methylene group	23.9	23.9	23.7
12	Methyl group	23.0	23.0	
13	Methyl group	10.8	10.8	11.0
14	Methylene group	30.4	30.4	30.5
15	Methyl group	13.9	13.9	13.9

**Table 5.2** <sup>13</sup>C chemical shift (ppm) for DEHP, Hy3-25DEHP and Hy5 taken from the MAS NMR spectra. a) The <sup>13</sup>C chemical shifts are reported as the medium position of the overlapped signals.

It is important to observe that the C7 carboxyl carbon in Hy5 sample is ~3 ppm shifted respect the pure DEHP and Hy3-DEHP. At the same time some others carbons (3/6 and 4/5 ring carbons between 2 and 3.8 ppm; C9 ~0.6 ppm and C10 ~1.4 ppm) close to the C7 show significant shifts. This would suggest that the C=O group of DEHP is in close contact with the surface of the mineral.

The  $^{13}\text{C}$  MAS spectrum of a calcite sample in which 100  $\mu\text{l}$  of neat DEHP was added to 300 mg of calcite (Cal1-100DEHP) is also shown in Figure 5.13. The carbon signals of this sample did not show chemical shift variations compared to those of neat DEHP, but the signals appear broader. No  $^{13}\text{C}$  MAS signal was observed from a calcite sample precipitated in the presence of sliced tubing sections (data not show). This observation would suggest that the DEHP released by the PVC slices is not strongly adsorbed at the surface of the calcite and consequently it is not incorporated during crystal growth.

## 5.7 $^{13}\text{C}$ CPMAS NMR investigation on hydrozincite /DEHP

Additional information can be obtained from the analysis of the  $^{13}\text{C}$  CPMAS spectra. Cross-polarization is a method of signal enhancement, whereby energy is transferred from abundant spins ( $^1\text{H}$ ) to the rare spins ( $^{13}\text{C}$ ). For the  $^1\text{H}$ - $^{13}\text{C}$  CP experiment, the efficiency of polarization transfer depends on the strength of the static dipolar interaction between  $^1\text{H}$  and  $^{13}\text{C}$  spins, which is determined by the number of protons directly bound to the carbons or close to them and the  $^1\text{H}$ - $^{13}\text{C}$  internuclear distances ( $<10 \text{ \AA}$ ). Effective intermolecular CP transfer also requires molecular rigidity, being hindered by molecular motions in the kilohertz range. (Fyfe, 1980; Demco et al., 1975; Hoffmann and Mayer, 1999).



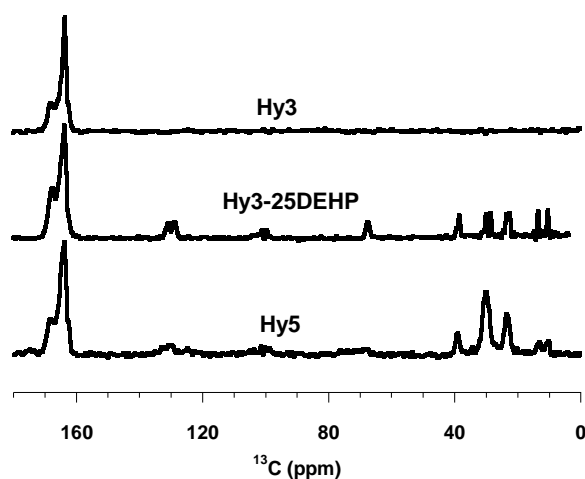


**Figure 5.14**  $^{13}\text{C}$  CPMAS NMR spectra of the following samples: pure hydrozincite (Hy3) hydrozincite mixed with DEHP (Hy3-25DEHP), DEHP adsorbed on hydrozincite by sliced pipes (Hy5).

The Figure 5.14 shows the  $^{13}\text{C}$  CPMAS NMR spectrum of the Hy3, Hy3-25DEHP and Hy5 samples collected with 8 ms contact time. No  $^{13}\text{C}$  CPMAS NMR signal of DEHP as a neat liquid is observed at any contact time, owing to molecular tumbling. The CPMAS spectrum of the Hy3 sample shows overlapping signals in the 162 – 169 ppm range, whose main peak appears at ~163.8 ppm. These signals are attributed to the carbonate group of hydrozincite, despite the fact that the carbonate in this mineral has only one crystallographic position in the ideal structure (De Giudici et al., 2009; Ghose, 1964) as described in the chapter IV. These additional peaks have been ascribed to the presence of lattice defects, namely grain boundaries and stacking faults that lower the crystal order in these

hydrozincite nanocrystals (Giudici et al., 2009). This feature is not changed in the CPMAS spectra of the Hy3-25DEHP and Hy5 samples as shown in Figure 5.14.

Carbon signals attributed to DEHP are observed in CPMAS spectra of the Hy3-25DEHP and Hy5 samples, which show that this molecule behaves like a solid. As shown in Figure 5.14, the aliphatic region (5-50 ppm) of the Hy3-25DEHP sample presents the same features as observed in the Hy3-25DEHP MAS spectrum, whereas the C8, the C4,5 and C3,6 carbons are broadened (FWHM >1.4 ppm). The signal attributed to the ring C1,2 carbons is not observed, probably due to extreme broadening. The signal of the carboxyl group cannot be observed because it is buried under the hydrozincite carbonate peaks.

As observed for the Hy3-25DEHP sample, the  $^{13}\text{C}$  CPMAS signals of the aliphatic region (5-50 ppm) of the Hy5 sample are also similar to those in the corresponding MAS spectrum. Differences are observed for the other carbon signals: the C8 peak disappears and those for the ring carbons are broad, as observed in the MAS spectrum. The carboxyl signal cannot be detected because it is buried below the hydrozincite carbonate peaks as stated for the Hy3-25DEHP sample. The behavior of the C=O, the C8 and the ring carbon resonances in the Hy5 sample is indicative of binding of the DEHP with hydrozincite, in agreement with the FT-IR results, and further suggests that these carbons are closest to the coordinating atoms. These data suggest that DEHP migrates from the PVC tubing, where it is bound by complex formation of the type  $>\text{C}=\text{O}:::\text{H}-\text{CH}_2-\text{Cl}$  (Baijayantimala and Swaminathan, 1996), to hydrozincite where it is incorporated between the crystallites during hydrozincite crystallization. At the same time the complex overlapping signals of aliphatic chains suggest the presence of significant structural disorder. Different modes of binding may occur at the hydrozincite surface. This consideration is in agreement with the observation of Phillips et al., (Phillips et al., 2005) of broad peaks in  $^{13}\text{C}$  CPMAS NMR spectra of citrate

coprecipitated with calcite which indicates multiple conformations of citrate with the calcite.

Signals from DEHP are absent in the  $^{13}\text{C}$  CPMAS spectrum Cal1-25DEHP and in the spectrum of the calcite sample precipitated in the presence of sliced PVC tubing sections (data not shown). The absence of CPMAS signal from the Cal1-25DEHP sample suggests that the DEHP is too mobile to cross-polarize and has a low affinity for binding at surface Ca sites compared to DEHP interacting with surface Zn sites in Hy3-25DEHP.

## **5.8 $^{13}\text{C}$ CPMAS NMR experiments with different contact times**

The CP technique is based on heteronuclear dipolar interaction, it is sensitive to internuclear dipolar interaction, to internuclear distance and to the mobility of molecules or functional groups involved (Kolodziejewski and Klinowski, 2002). This means that CP can be used to establish the connectivity between coupled nuclei and to monitor molecular dynamics in solids, a very useful feature in the structural determination. To gain such information it is indispensable to measure the spin lattice relaxation time in the rotating frame,  $T_{1\rho}$ , and the cross-polarization time ( $T_{\text{CH}}$ ). Variable contact time CP experiments allow simultaneous monitoring of  $T_{\text{CH}}$  and  $T_{1\rho}$ . However these experiments require spectra with a good signal/noise ratio, which is not our case. In fact, as it is observed in the Figure 5.14 using the  $^{13}\text{C}$  natural abundance the ratio signal/noise is poor. Moreover important information, although qualitative, can be obtained by collecting the spectra with few contact times.

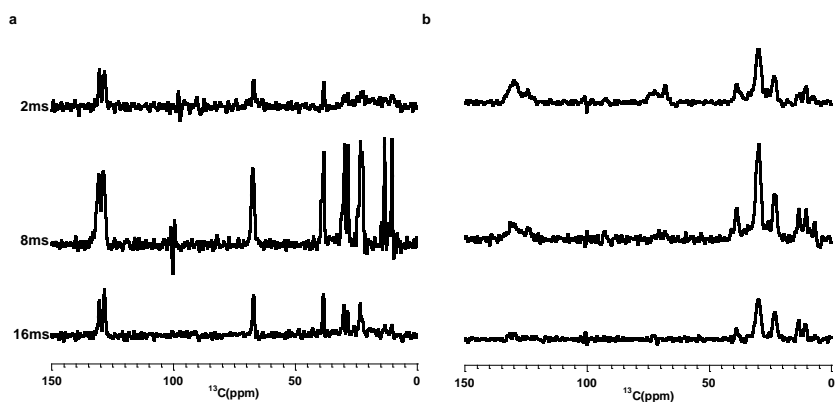


**Figure 5.15**  $^{13}\text{C}$  CPMAS experiments collected with 2, 8 and 16 ms of contact time for the samples Hy3-25DEHP (a) and Hy5 (b).

The experiments for the sample Hy3-25DEHP and Hy5 have been collected using 2, 8 and 16 ms of contact times. The Figure 5.15 a and b display the spectra for the samples Hy3-25DEHP and Hy5, respectively. In these experiments we analyzed the signals for the DEHP in the range between 0-150 ppm. Over this range the signals of the hydrozincite carbons do not allow the observation of C=O carbon of DEHP.

Several considerations can be drawn on the evolution of the carbons signals in these experiments:

Hy3-25DEHP – In the experiment performed with 2 ms of contact time only the ring carbons (C3/6 and C4/5) and the carbons C8 and C9 signals are observed. The intensities of the aliphatic chains signals are very low. All signals increase at 8 ms of contact time and decrease at 16 ms of contact time. This evolution is more evident for the carbons C13 and C15.

Hy5 – the CPMAS spectra collected with 2, 8, 16 ms of the Hy5 sample show broad signal as reported before. The intensity of the ring carbons and C8 and C9 decrease at 8 ms and disappear at 16 ms, while the aliphatic carbons show similar evolution as observed in the Hy3-25DEHP.

The behavior of the C8 and the ring carbon resonances in the Hy5 sample, when compared to the behavior of the same signals in the Hy3-25DEHP, is indicative of reduced mobility and/or of a stronger  $^1\text{H}$ - $^{13}\text{C}$  hetero nuclear dipolar coupled network, thus suggesting that those atoms are the most involved in the interaction with the mineral. The aliphatic chains display slower CP kinetics in both samples denoting a lower rigidity of this portion of the molecules of DEHP. The non-rigid environment and inefficient cross-polarization have been observed previously for organic molecules intercalated in smectite (Corrado et al., 1990; O'Brein et al., 1991) and for the adsorbed pyridine on clay minerals (Ukrainczyk and Smith, 1996). These results, which are in good agreement with the FT-IR,  $^{13}\text{C}$  MAS and CPMAS results, confirm that the portion of the molecule including the carboxyl group of DEHP, in the sample Hy5, is strictly bound to the surface of hydrozincite.

## 5.9 $^1\text{H}$ MAS informations

Further experiments were carried out on Hy3-25DEHP and Hy5 samples in order to investigate the surface of the hydrozincite mineral, through the  $^1\text{H}$  resonance of water and DEHP molecules. The mobility of a molecule at the surface of solid matrix can be assessed; as reported in the literature, also with  $^1\text{H}$  MAS experiments that are very promising in differentiating molecular species according to their degree of mobility in solids (Chamignon et al., 2004).

In the Figure 5.18 the  $^1\text{H}$  MAS spectra of Hy3-25DEHP and Hy5 are reported.

The spectrum of Hy3-25DEHP shows broad peaks respect to the  $^1\text{H}$  spectra acquired in liquid state (see paragraph 5.2). The peaks at 7.8 and 7.6 ppm are attributed to the proton resonance of the ring protons 4/5 and 3/6, respectively; two broad resonances at 4.5 and 4.3 ppm attributable to the proton in the position 8 in the DEHP molecule the very broad resonance in the range between 2.2 and 0.5 ppm with two maximum at 1.4 and 1.0 ppm are due to the aliphatic chain; the signal centered at 5.1 ppm is due to the water content present at the surface of the hydrozincite mineral.

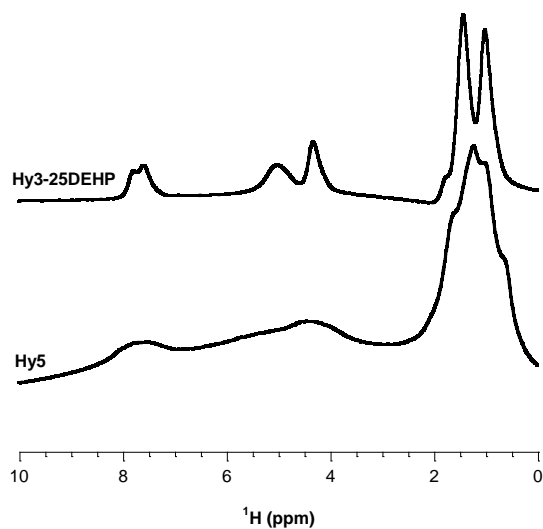


**Figure 5.16**  $^1\text{H}$  MAS experiments from Hy3-25DEHP mixed sample and from precipitate sample in the presence of PVC Hy5.

The spectrum of the Hy5 sample shows  $^1\text{H}$  signals much broader than those observed in the Hy3-25DEHP spectrum, in agreement with the  $^{13}\text{C}$  MAS and CPMAS spectra. In particular, the resonances of the ring protons and the protons in the position 8 in the DEHP molecule are particularly broad. It is remarkable the

broadening of the proton resonance (~5 ppm) attributed to the water molecules at the hydrozincite surface.

MAS NMR signals basically reflect the degree of mobility of the species loaded onto the surface of a solid matrix: very mobile molecules give narrow signals, close to those of liquid-state NMR spectra. In contrast, when the strength of the interaction increases, the signals are broader. In this way, it is possible to differentiate adsorbed versus incorporated DEHP. Similar examples are reported in literature for the study of 4-chloro-2-methylphenoxyacetic acid in clays (Combourieu et al., 2001).

Thus, it appears that the  $^1\text{H}$  MAS NMR is suitable to discriminate different species (mobile and immobile) of a DEHP loaded onto the surface of hydrozincite. From these considerations it is evident that DEHP molecules in the Hy3-25DEHP are weakly-bound to the surface of the hydrozincite. On the contrary, the results clearly show that, in the Hy5 sample, the DEHP molecules are strongly bound or incorporated between the hydrozincite nanoparticles.

## **5.10 X-Ray Diffraction complementary informations**

The structural differences between synthetic hydrozincite Hy3 and synthetic hydrozincite synthesized in the presence of PVC slices Hy5 have been investigated by XRD diffraction. The XRD patterns of the two samples are reported in Figure 5.17. Both XRD patterns exhibit Bragg reflections that can be indexed as hydrozincite single phase with a monocline structure, according to experimental (PDF Card 19-1458) and calculated (PDF 72-1100) references patterns.

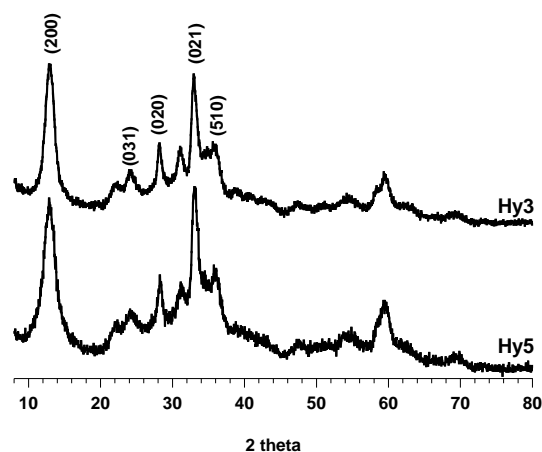


**Figure 5.17** XRD patterns of Hy3 and Hy5.

The XRD patterns do not reveal important modification of mineral structures for Hy5 compared with the Hy3, and this result is in agreement with the NMR and FTIR evidences. Slight differences might be observed in the peak positions. In the pattern of Hy5 sample, compared with Hy3, a small shift to a lower value is observable for the peak (200) [ $2\theta=12.97^\circ$  for Hy3 and  $12.87^\circ$  for Hy5]. This results in a low increase of the d-spacing for this reflection. However, the (020) and (021) reflections show a small shift to higher values that are correlated with a decrease of the d-spacing for these reflections. This might be an evidence for the intercalation of DEHP in hydrozincite structure, although these changes are not very evident, this can be due at the low concentration of DEHP in Hy5 sample. In fact, in the literature, significant variations in XRD patterns for intercalated molecules are reported for high concentration of intercalated molecules (Chamignon et al., 2004).



All diffraction peaks are slightly broad in the HY5 sample; the broadening can be ascribed to the presence of DEHP with consequent increase of disorder in the structure, and this is in agreement with the previous  $^{13}\text{C}$  MAS measurements.

## 5.11 Conclusions

The interaction of Bis(2-ethylhexyl)phthalate (DEHP) with hydrozincite [ $\text{Zn}_5(\text{CO}_3)_2(\text{OH})_6$ ], under controlled laboratory experiments, was investigated by using Fourier Transform Infrared (FT-IR), Nuclear Magnetic Resonance Spectroscopy (NMR) and X-ray Diffraction (XRD).

Our results from FT-IR and solid state  $^{13}\text{C}$  NMR indicate that DEHP released from flexible PVC tubing is bound to the hydrozincite structure during crystallization. Under our experimental conditions the hydrozincite contains about ~10% (w/w) DEHP taken up from the tubing.  $^{13}\text{C}$  MAS and CPMAS NMR spectra reveal that the chemical shift, the intensity and the line width of DEHP carboxylic group and the ring carbons are greatly affected. These data suggest that the carboxyl head group is directly involved in the binding to hydrozincite. At the same time, the observed broad and overlapping aliphatic carbon signals of DEHP, is indicative of structural disorder. Overall these results would suggest that DEHP is sequestered from the tubes and incorporated at the hydrozincite nanoparticles surface during the crystallization. In contrast,  $^{13}\text{C}$  MAS and CPMAS NMR data show that DEHP is not incorporated in calcite precipitated in the presence of flexible tubing. XRD results are also consistent with an increase of structural disorder in hydrozincite structure caused by the presence of DEHP, in agreement with the  $^{13}\text{C}$  MAS measurements.

This result suggests a specific interaction between DEHP and surface Zn-centers is responsible for the strong uptake of DEHP by hydrozincite.

## 5.12 References

- Baijayantimala, G., and Swaminathan, S. Study of Polymer–Plasticizer Interaction by  $^{13}\text{C}$  CP/MAS NMR Spectroscopy: Poly(vinyl chloride)–Bis(2-ethylhexyl) Phthalate System. *Macromolecules*, 29, 185-190 (1996).
- Balmain, J., Hannover, B., Lopez, E. Fourier transform infrared spectroscopy (FTIR) and X-ray diffraction analyses of mineral and organic matrix during heating of mother of pearl (nacre) from the shell of the mollusc *Pinctada maxima*. *J. Biom. Mat. Res. B*, 48, 749–54 (1999).
- Cebeci, Y., and Sonmez, I. A study on the relationship between critical surface tension of wetting and oil agglomeration recovery of calcite. *J. Coll. Int. Sci.*, 273, 300-305 (2004).
- Chamignon, C., Haroune, N., Forano, C., Delort, A.-M., Besse-Hoggan, P., Combourieu, B. Mobility of organic pollutants in soil components. What role can magic angle spinning NMR play? *Eur. J. Soil Sci.*, 59, 572–583 (2008).
- Cohen, H., Charrier, C., Sarfaty, J. Extraction and Identification of a Plasticizer, Di-(2-ethylhexyl)phthalate, from a Plastic Bag Containing Contaminated Corn. *Arch. Environ. Contain. Toxicol.*, 20, 437-440 (1991).
- Combourie, B., Inacio, J., Delort, A.M., Forano, C. Differentiation of mobile and immobile pesticides on anionic clays by  $^1\text{H}$  HR MAS NMR spectroscopy. *Chem. Comm.*, 21, 2214–2215 (2001).
- Corrado, K.A., Hayatsu, R., Botto, R.E., Winans, R.E. Reactivity of anisoles on clay and pillared clay surfaces. *Clay and clay miner.*, 38, 250 (1990).
- De Giudici, G., Podda, F., Sanna, R., Musu, E., Tombolini, R., Cannas, C., Musinu, A., Casu, M. Structural properties of biologically controlled hydrozincite: a HRTEM and NMR spectroscopic study. *Amer. Mineral.*, 94, 1698-1706 (2009).

- Demco, D. E., Tegenfeldt, J., Waugh, J. S. Dynamics of cross relaxation in nuclear magnetic double resonance. *Phys. Rev.*, 11, 4133 (1975).
- Fyfe, C.A., Solid State NMR for Chemists. C.F.C. Press: Guelph, Ontario, Chapter 1 (1983).
- Fyfe, C.A., Solid State NMR for Chemists. Guelph University Press. Guelph, Canada (1980).
- Ghose, S. The crystal structure of hydrozincite,  $Zn_5(OH)_6(CO_3)_2$ . *Acta Crystallog.*, 17, 1051-1057 (1964).
- Hales M., and Frost R. Synthesis and vibrational spectroscopic characterisation of synthetic hydrozincite and smithsonite. *Polyhedron*, 4955-4962 (2007).
- Hoffmann, D., and Mayer, C. Cross polarization induced by temporary adsorption: NMR investigations on nanocapsule dispersions. *J. Chem. Phys.*, 112, 4242-4250 (1999).
- Kolodziejewski, W., Klinowski, J. Kinetics of Cross Polarization in Solid State NMR: a guide for chemist. *Chem. Rev.*, 2002, 102, 613-628.
- Music, S., Popovic, S., Maljkovic, M., Dragcevic, D. Influence of synthesis procedure on the formation and properties of zinc oxide. *J. Alloys Compd.*, 347, 324-332 (2002).
- O'Brein, P., Williamson, C.J., Groombridge, C. J. Multinuclear solid-state MAS and CP-MAS NMR study of the binding of triethyl phosphate to a montmorillonite *Chem. Mater.* 3, 276 (1991).
- Ukrainczyk, L. and Smith, K. A. Solid State  $^{15}N$  NMR study of pyridine adsorption on clay minerals. *Environ.Sci.Technol.* ,30, 3167-3176 (1996).
- White, W.B. The carbonate minerals. In V.C. Farmer, Ed., The infrared spectra of minerals, p.227-279. Mineralogical Society Monograph, London (1974).



## General considerations

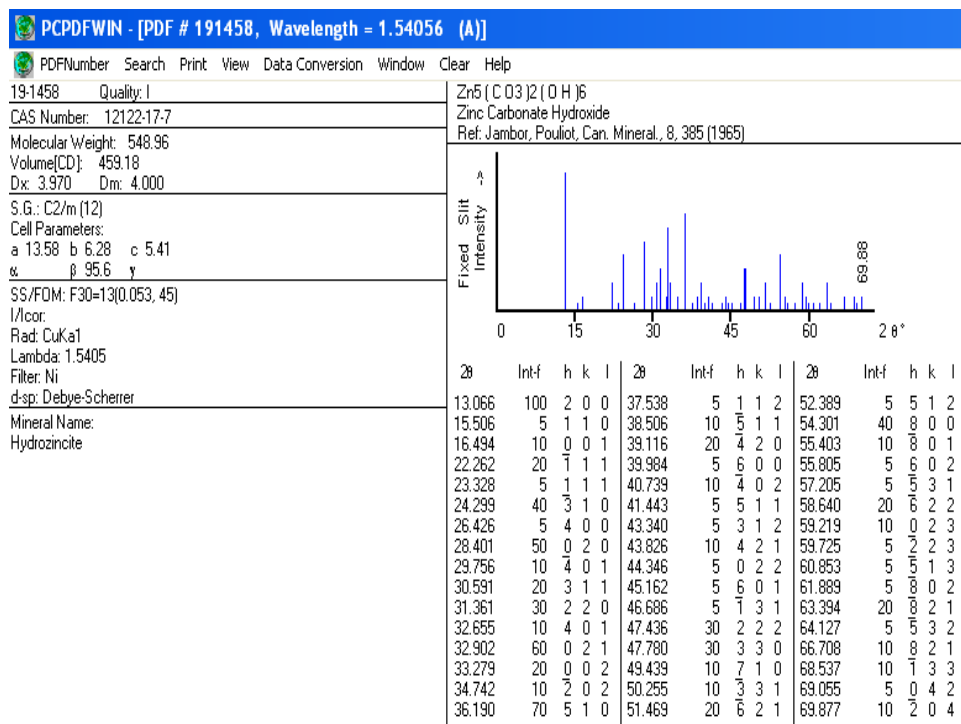
Materials have played an important role in our civilization, embedding our political history and culture. Historians have used the state of materials technology as nomenclature for various periods of mankind's history (e.g., stone, bronze and iron) but the field of Material Science and Engineering began to be considered its own discipline around the mid 1960's. The advancement in human history can be traced by the progress in materials processing techniques, from the development of the Damascus steel used to produce unrivaled weaponry, to the refinement of silicon for computer chips in modern computer systems. Yet, towards the end of the 20<sup>th</sup> century, it was discovered that while mankind had indeed advanced in the development of technology, there were still lessons that could be learned from Nature. Scientists and engineers have long envied Nature's ability to design crystalline structures whose properties are often superior to those of similar synthetic materials. The work contained within this dissertation can be considered a piece of knowledge which can contribute to understanding the complex world of biomineralization and the reactivity of minerals. Finally, the mechanism governing the hydrozincite biomineral formation at the molecular level is not yet understood. The role of organic matter in the biomineralization requires further investigation. Despite this, the information acquired in this PhD period about the morphology, structure and organic matter present in the hydrozincite biogenic formation will be used for modeling the mechanism of formation of biominerals and for the prediction of their reactivity and stability under specific environmental conditions.

Further studies are required to examine the stability, strength and geometry of the interaction between DEHP molecule and hydrozincite surfaces and to assess whether nanocrystalline hydrozincite can be regarded as an effective sorbent that

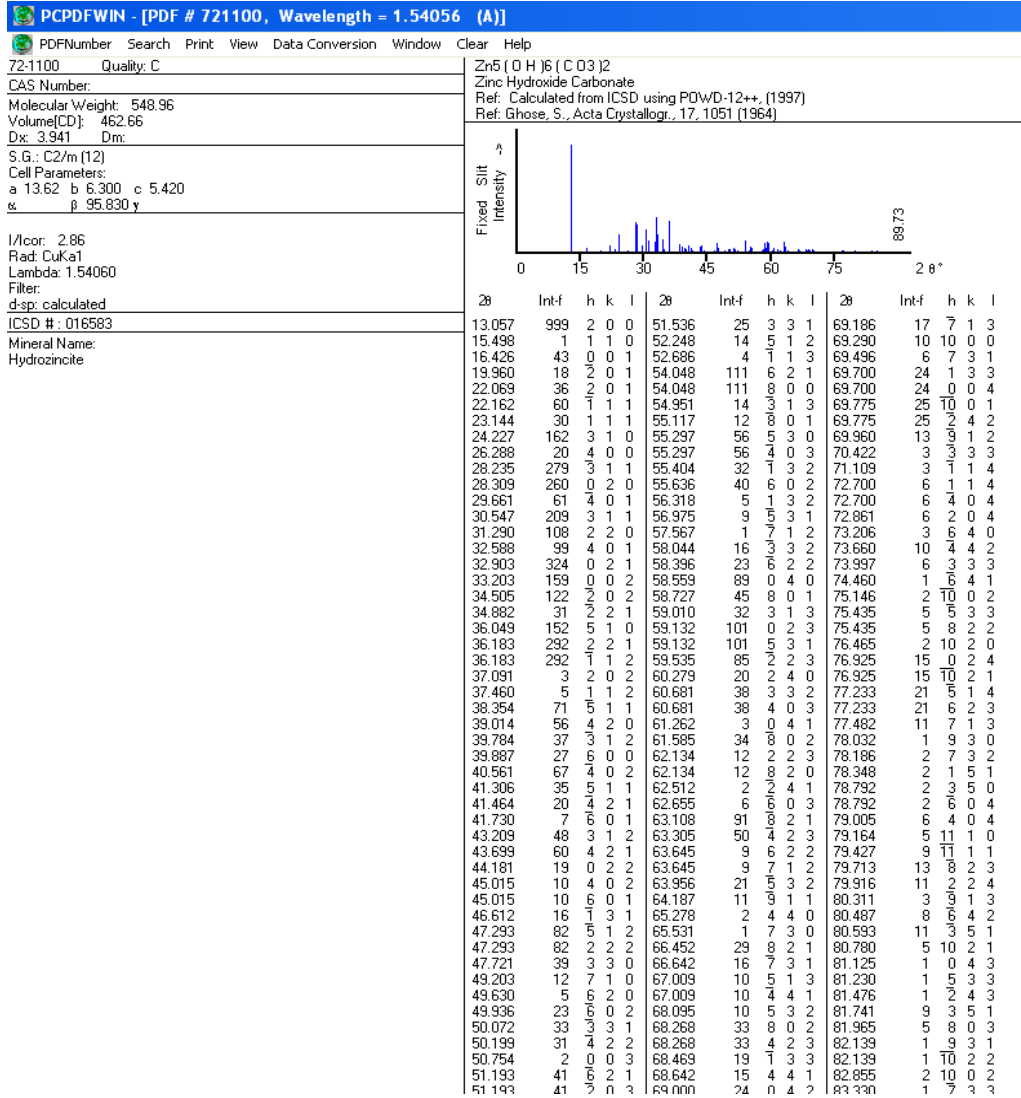
incorporates DEHP for the use in remediation strategies under different environmental conditions.

## Appendix

- PDF Card 19-1458 Wavelength = 1.54056Å

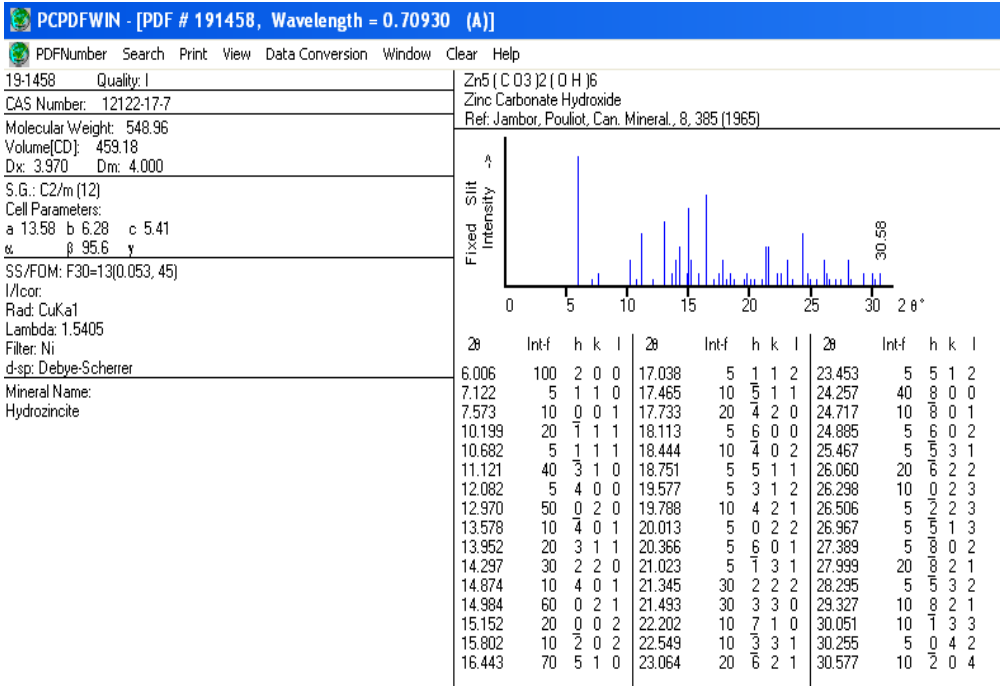


• PDF Card 72-1100 Wavelength = 1.54056Å

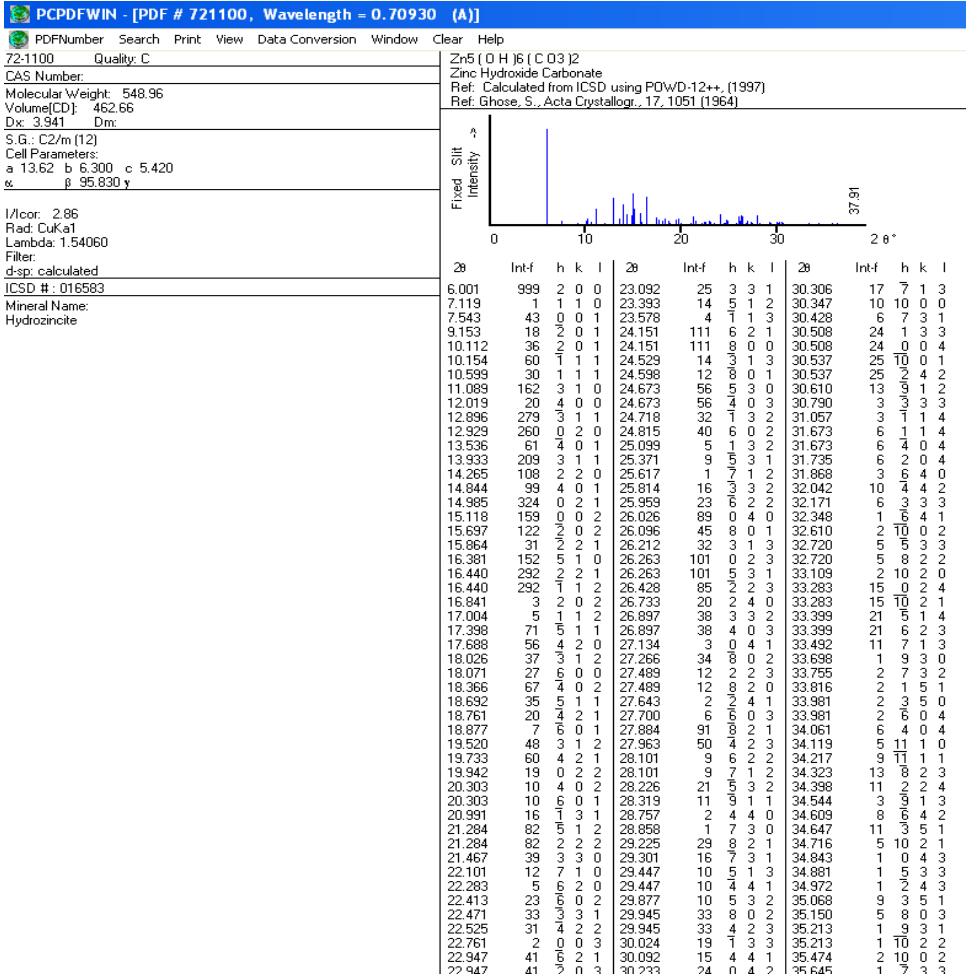




• PDF Card 19-1458 Wavelength = 0.70930 Å



• PDF Card 72-1100 Wavelength = 1.54056 Å



## Scientific Publications

1) Giovanni De Giudici, Francesca Podda, Roberta Sanna, Elodia Musu, Riccardo Tombolini, Carla Cannas, Anna Musinu and Mariano Casu; *Structural properties of biologically controlled hydrozincite: a HRTEM and NMR spectroscopic study. Am.Miner.* , 94 (11), pp 1698-1707 (2009).

2) Carla Cannas, Anna Musinu, Andrea Ardu, Federica Orru', Davide Peddis, Mariano Casu, Roberta Sanna, Fabrizio Angius, Giacomo Diaz and Giorgio Piccaluga. *CoFe<sub>2</sub>O<sub>4</sub> and CoFe<sub>2</sub>O<sub>4</sub>/SiO<sub>2</sub> Core/Shell Nanoparticles: Magnetic and Spectroscopic Study. Chem. Mater.*, 22 (11), pp 3353–3361 (2010).

3) Giuseppina Marras, Anna Musinu, Roberta Sanna. *L'uso di "malta" in età nuragica*. In press In Atti XLIV Riunione Scientifica in Sardegna-II (2011).

4) Carla Mura, Donatella Valenti, Costantino Floris, Roberta Sanna, Maria Antonietta De Luca, Anna Maria Fadda, and Giuseppe Loy. *Metronidazole prodrugs: synthesis, physicochemical properties, stability, and ex vivo release studies*. Submitted to *European Journal of Pharmaceutical Chemistry*.

5) Roberta Sanna, Mariano Casu, Costantino Floris, Francesca Podda, and Giovanni De Giudici. *A FTIR and solid state <sup>13</sup>C NMR study of the adsorption of Bis(2-ethylhexil)Phthalate on hydrozincite*. In preparation.

6) Martina Pilloni, Guido Ennas, Mariano Casu, Anna Maria Fadda, Francesca Frongia, Francesca Marongiu, Roberta Sanna, Alessandra Scano, Donatella

Valenti, Chiara Sinico. *Caffeine Silica Nanocomposites: effect of inclusion in silica matrix*. In preparation.